Sheet Metal Forming and Failure during Biaxial Stretching at High Strain Rates

Richard Davies

UNIVERSITE DE STRASBOURG

École Doctorale Mathématiques, Sciences de l'Information et de l'Ingénieur

Institut de Mécanique des Fluides et des Solides

THÈSE

Présentée pour obtenir le grade de:

Docteur de l'Université de Strasbourg

Discipline : Mécanique des matériaux

Spécialité : Mise en Forme des Métaux

par

Richard W. DAVIES

Mise en forme et endommagement des tôles métalliques sous chargement biaxial à taux de déformation élevé. "Sheet Metal Forming and Failure during Biaxial Stretching at High Strain Rates"

Soutenue le 21 Mai 2012

Membres du jury

Directeur de thèse :	**Prof. Saïd AHZI, Université de Strasbourg**
Co-Directeur de thèse :	**Dr. Mohammad KHALEEL, Pacific Northwest National Laboratory, USA**
Rapporteur externe :	**Prof. Frédéric BARLAT, Pohang University of Science and Technology, Corée du Sud**
Rapporteur externe :	**Prof. José Gracio, University of Aveiro, Portugal**
Examinateur :	**Prof. Yves REMOND, Université de Strasbourg**
Examinateur :	**Prof. Siham M'GUIL, Université de Strasbourg**
Invité :	**Prof. Pedro de Magalhaes Correia, Université de Strasbourg**

Nom du Laboratoire: IMFS **N° de l'Unité FRE 3240**

Sheet Metal Forming and Failure During Biaxial Stretching at High Strain Rates

Doctoral Thesis

University of Strasbourg

Rich Davies

Table of Contents

1 Abstracts

1.1 English Abstract

This thesis focuses on scientific investigation to develop and enable a class of high strain rate sheet metal forming of aluminum alloys and advanced high strength steel (AHSS). These technologies employ a short duration pressure-pulse to drive sheet metal into single-sided dies, and can generally be described as pulse pressure forming (PPF) processes. The work under this thesis has overcome three technical barriers to using PPF processing for more cost effective lightweight vehicles. The first technical barrier was the lack of understanding of the interrelationship between formability and measured strain rates that develop during PPF processing. The work under this thesis investigated the formability and fracture of sheet metals during PPF, and characterized the strain rate and the strain rate heterogeneity. The second technical barrier was the lack of a validated constitutive model for lightweight materials during PPF processing. The work under this thesis investigated the microstructure and mechanical property evolution in metals during PPF. The third technical barrier was the lack of validated and predictive formability models for PPF processes. The work under this thesis used the Marciniak and Kuczynski method of formability prediction to predict the formability of both aluminum alloy AA5182 and AHSS alloy DP600 across a wide range of strain rates and strain rate directions. The combination of these research results permits a more predictive capacity to design and develop PPF manufacturing processes for a desired automotive component made from aluminum alloys and AHSS.

1.2 French Abstract

Cette thèse met l'accent sur la recherche scientifique pour développer une classe de procédés à hautes vitesses de déformation des tôles métalliques en alliages d'aluminium et en acier à haute résistance (AHR). Ces technologies emploient une impulsion de pression de courte durée qui propulse la tôle dans une matrice. Ces procédés sont généralement décrits comme procédés de formage par impulsion de pression (PPF). Le travail proposé dans ce mémoire de thèse a permis de surmonter trois obstacles pour l'utilisation des procédés PPF et la fabrication à moindre coût de structures légères. Le premier obstacle a été le manque de corrélation entre formabilité et vitesses de déformation qui se développent lors d'un procédé PPF. Nous avons proposé d'analyser la formabilité et la rupture des tôles, et de caractériser les vitesses de déformation et leur l'hétérogénéité pendant le procédé PPF. Le deuxième obstacle a été le manque de lois constitutives validées pour les métaux déformés par le procédé PPF. Nous avons étudié la microstructure et l'évolution des propriétés mécaniques durant le procédé PPF. Le troisième obstacle est le manque de modèles de formabilité prédictifs validés pour le procédé PPF. Nous avons utilisé la méthode Marciniak-Kuczynski pour la prédiction de la formabilité de l'alliage AA5182 et de l'acier DP600 sous un large éventail de vitesses de déformation et sous différentes directions de ces vitesses. La combinaison de ces résultats de recherche permet une plus grande capacité prédictive pour concevoir et développer des procédés PPF pour composants d'automobile désirés à partir d'aluminium et d'acier AHR.

1.3 Extended English Abstract

This thesis focuses on scientific investigation to develop and enable a class of high strain rate sheet metal forming processes to more cost-effectively manufacture automotive structures made from aluminum alloys and advanced high strength steel (AHSS). These technologies employ a short duration pressure-pulse to drive sheet metal into single-sided dies, and can generally be described as pulse pressure forming (PPF) processes. The most common PPF processes being developed include electromagnetic forming [1, 2], electrohydraulic forming [3], and laser shock forming [4]. These PPF technologies develop in-process strain rates that are usually two to five orders of magnitude higher than conventional metal forming.

Wider vehicle application of aluminum alloys offers the potential weight reduction of 35-50%, and AHSS offers the potential weight reduction of 20-35%, if they are substituted for higher density or lower strength steel that are conventionally deployed in vehicles. However, the limited formability and the cost of processing these materials limit their application in vehicles. To produce more affordable lightweight metal structures, it will be necessary to develop and improve the manufacturability of these materials; and to develop tools that support the manufacturing process and reduce the cost of lightweight components. These metal forming processes have some remaining technical barriers to implementation. The figure below illustrates three critical attributes and the interdependency of these attributes that ultimately influence the formability of materials during sheet metal forming:

- *Process Design* imposes the pressure pulse, material constraints, and the forming dies that will ultimately create the desired shape of the sheet metal component
- *Deformation Behavior* of the material is defined by the material velocities, strains, strain rates, and die impact velocities that results from the process design
- *Constitutive Relations* of the materials will define the resulting flow stress as a function of strain hardening, strain rate sensitivity, anisotropy, and adiabatic heating of the subject material

These three factors interplay and influence each other during sheet metal forming processes, and collectively they primarily define the resulting material formability. All three of these critical attributes can vary highly under pulse pressure forming. The formability, failure modes, and constitutive relations of most metallic materials can be dramatically different as a result of the higher PPF process strain rates. This is particularly true for many emerging automotive materials such as aluminum and AHSS.

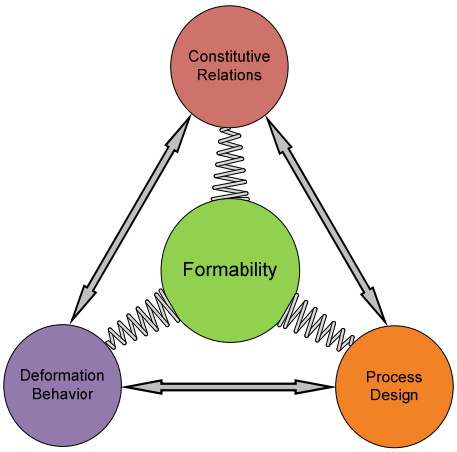

Formability of sheet metal is primarily dictated by three critical attributes and the interplay of these attributes

The work under this thesis has overcome three technical barriers to using PPF processing for more cost effective lightweight vehicles. The first technical barrier was the lack of understanding of the interrelationship between formability and measured strain rates that develop during PPF processing. There have been past works measuring sheet metal speed and general shape using videos [5], or measuring surface velocity of the materials [6]. But, this past work does not yield direct measurement of biaxial strains and strain rates during forming. The work under this thesis investigated the formability and fracture of metals during PPF, and characterized the strain rate, strain rate heterogeneity, formability, and fracture of sheet metal during PPF. This work also quantified the extended ductility of lightweight metals during PPF under proportional and variable strain rate loading using a unique experimental apparatus at Pacific Northwest National Laboratory (PNNL). The apparatus used high speed camera arrays (up to 80,000 frames per second) and digital image correlation to locally interrogate strains and strain rates during PPF to characterize full-field biaxial strain and strain rate measurement [7, 8]. The results of this work showed that electromagnetic forming and electrohydraulic forming processes can develop sheet metal velocities up to 150 meters/sec, and create true effective plastic strain rates in excess of $2x10^3$/sec.

The second technical barrier was the lack of a validated constitutive model for lightweight materials during PPF processing. The work under this thesis investigated the microstructure and mechanical property evolution in metals during PPF. Most metallic materials exhibit significant changes in flow stress based on strain rates [9] and mechanical property and microstructure variation [10]. This work determined the constitutive relations of aluminum alloy AA5182 and AHSS alloy DP600 at PPF strain rates, and investigated the variation in microstructure and texture evolution that evolves during PPF [11]. The results of this work showed that the strain rate sensitivities of these materials can vary between m= -.022 to 0.08 for AA5182, and is relatively constant at m=0.02 for DP600. Furthermore, the strain rate sensitivity of AA5182-O appears to be significantly dependent on the grain size and prior thermo-mechanical processing on the materials; where finer equiaxed grains result in higher

strain rate sensitivities in the material. These varying strain rate sensitivities result in constitutive relations that vary highly and become very advantageous for aluminum at strain rates above 10^3/sec during PPF.

The third technical barrier was the lack of validated and predictive formability models for PPF processes. The lack of full-field strain, strain rate, and deformation history during PPF makes validation of finite element models very difficult. Past work has focused on simple and reliable numerical models for PPF forming [12, 13, 14], but little validation opportunity is available with full-field deformation history. The work under this thesis used the Marciniak and Kuczynski (M-K) method of formability prediction to predict the formability of both aluminum alloy AA5182 and AHSS alloy DP600 across a wide range of strain rates and strain rate directions [15]. The results of this work validate the applicability and fitness of the M-K method to predict formability of sheet metals during pulse pressure forming. Furthermore, these models are used to parametrically evaluate the formability of the multiple sheet metals across a wide range of strains, strain rates, and loading paths.

The combination of these research results permits a more predictive capacity to design and develop PPF manufacturing processes for a desired automotive component made from aluminum alloys and AHSS. The first step in developing a new application should be selecting material and characterizing and modeling its constitutive relations from quasi-static to strain rates of 10^4/sec. The second step should be predicting the forming limits of the material across the PPF range of strains and strain rates using the predictive formability models. The third step should be designing the process to achieve the strain rates necessary for the selected material to form the given automotive component. In this way, the process can be designed to deliver the desired deformation behavior, which will capitalize on the materials constitutive behavior, and maximize the material formability.

1.4 Extended French Abstract

Cette thèse met l'accent sur la recherche scientifique pour développer et permettre à une classe de procédés à hautes vitesse de déformation des métaux de devenir plus rentable pour la fabrication des structures, pour l'industrie l'automobile, en alliages d'aluminium et en acier à haute résistance. Ces technologies emploient une impulsion de pression de courte durée qui pousse la tôle métallique dans une matrice. Ces procédés sont généralement décrit comme procédés de formage par impulsion de pression (« pulse pressure forming, PPF »). Parmi les procédés PPF, les plus courants sont le formage électromagnétique [1, 2], formage électrohydraulique [3], et le formage par impulsion laser (laser shock forming) [4]. Dans ce travail de thèse, on s'intéresse aux deux premiers procédés. Les vitesses de déformation qui se développent durant ces procédés sont habituellement de deux à cinq ordres de grandeur plus élevées que celles des procédés classiques.

Une application plus large des alliages d'aluminium dans l'industrie automobile offre une réduction du poids de 35-50%, et les aciers à haute résistance offrent une réduction de 20-35%, s'ils sont substitués aux aciers à densité plus élevée ou à plus faible résistance qui sont classiquement employés. Toutefois, la formabilité limitée et le coût de fabrication de ces matériaux limitent leur application dans l'industrie automobile. Pour une production plus abordables des structures métalliques légères, il nécessaire de développer et d'améliorer les méthodes de fabrication de ces matériaux. Ces procédés de formage des métaux ont certains obstacles techniques qui restent à résoudre. La figure ci-dessous illustre les trois attributs essentiels et l'interdépendance de ces attributs qui influencent la formabilité:

- Le design du procédé impose l'impulsion de pression, les conditions sur le matériau, et la matrice qui permet d'obtenir la forme désirée.
- Le comportement du matériau qui dépend des vitesses imposées, du taux de déformation, et des vitesses d'impact contre la matrice.
- Les lois constitutives du matériau qui permettent de définir la contrainte d'écoulement en fonction de l'écrouissage, de la sensibilité à la vitesse de déformation, de l'anisotropie, et de l'effet d'échauffement adiabatique.

Ces trois facteurs interagissent entre eux au cours du procédé de formage des tôles. Ils définissent d'une façon collective la formabilité résultante du matériau. Ces trois facteurs critiques peuvent varier fortement sous formage par impulsion de pression (PPF). La formabilité, mécanismes d'endommagement, et relations constitutives des matériaux métalliques peuvent être considérablement différentes en raison du taux de déformation élevé durant les procédés PPF. Cela est particulièrement vrai pour de nombreux alliages émergents pour les applications en automobile tels que des alliages d'aluminium et aciers à haute résistance.

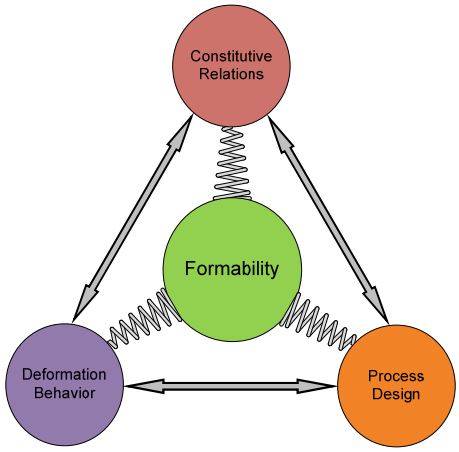

Formabilité des tôles principalement contrôlée
par trois paramètres essentiels et leurs interactions

Le travail proposé dans ce mémoire de thèse a permis de surmonter trois obstacles pour l'utilisation des procédés PPF et la fabrication à moindre coût de structures légères. Le premier obstacle technique a été le manque de compréhension de l'interrelation entre la formabilité et les vitesses de déformation qui se développent lors d'un procédé PPF. Les méthodes existantes pour mesurer les vitesses de déformation et la forme générale de tôle sont soit à l'aide de vidéos [5] ou par la mesure de vitesse à la surface du matériau [6]. Cependant, ces méthodes ne donnent pas de mesure directe des contraintes biaxiales et des vitesses de déformation lors du formage. Dans le

travail développé dans le cadre de cette thèse, nous avons proposé d'analyser la formabilité et la rupture des métaux pendant le procédé PPF, et de caractériser les vitesses de déformation, l'hétérogénéité des vitesses de déformation, la formabilité, et la rupture de la tôle pendant le procédé PPF. Dans ce travail, nous avons également quantifié la ductilité des métaux légers lors du procédé PPF sous des chargements à vitesse de déformation variable et proportionnel. Pour cela, nous avons utilisé des équipements expérimentaux uniques à « Pacific Northwest National Laboratory (PNNL) ». Cet équipement utilise une série de cameras à hautes vitesse (environ 80.000 images par seconde) et la corrélation d'images numériques pour déterminer les vitesses de déformation et les déformations locales pendant le procédé PPF. Ceci nous a permis de caractériser le champ de déformation biaxiale et les vitesses de déformation [7, 8]. Les résultats de ce travail ont montrés que le formage électromagnétique et le formage électrohydraulique peuvent développer des vitesses allant jusqu'à 150 m/s et de créer un véritable effet des taux de déformation plastique qui s'élèvent à de plus de $2x10^3$ s^{-1}.

Le deuxième obstacle technique a été le manque de lois constitutives validées pour les métaux déformés par le procédé PPF. Dans ce travail de thèse, nous avons étudié la microstructure et l'évolution des propriétés mécaniques des métaux durant le procédé PPF. La plupart des matériaux métalliques présentent des changements significatifs de la contrainte d'écoulement en fonction du taux de déformation [9] ainsi que des variations des propriétés mécanique et de la microstructure [10]. Dans ce travail, nous avons déterminé des lois constitutives pour l'alliage d'aluminium AA5182 ainsi que pour l'acier à haute résistance DP600 sous des taux de déformation de l'ordre de ceux observés sous PPF. Nous avons aussi caractérisé la variation de la microstructure et l'évolution des textures de déformation par PPF [11]. Les résultats de ce travail ont montré que la sensibilité au taux de déformation de ces matériaux peut varier entre m = - 0,022 à 0,08 pour AA5182, et m = 0,02 (relativement constant) pour DP600. Ces sensibilités au taux de déformation conduisent à des relations constitutives qui varient fortement et qui deviennent très avantageuses pour l'aluminium à des vitesses de déformation supérieures à 10^3 s^{-1}.

Le troisième obstacle est le manque de modèles de formabilité prédictifs validés pour le procédé PPF. Le manque d'une connaissance complète du champ de déformation, du taux de déformation, et de l'histoire de la déformation pendant le procédé PPF rend la validation des modèles éléments finis très difficile. Les travaux antérieurs ont porté sur le développent de simples, mais fiables, modèles numériques pour les procédés PPF [12, 13, 14], mais avec peu de validation due a la non disponibilité des champs de déformation et leurs évolutions. Dans le cadre de cette thèse, nous avons utilisé la méthode Marciniak et Kuczynski (MK) pour la prédiction de la formabilité de l'alliage d'aluminium AA5182 et de l'acier duplex DP600 sous un large éventail de vitesses de déformation et sous différentes directions de ces taux de déformation [15]. Les résultats de ce travail ont d'abord validé l'applicabilité de la méthode MK pour la prédiction de la formabilité durant les procédés PPF. En outre, nous avons utilisé cette approche avec une analyse paramétrique pour évaluer la formabilité des tôles métalliques sous un large éventail de déformations, de taux de déformation et de chemins de chargement.

La combinaison de ces résultats de recherche permet une plus grande capacité prédictive pour concevoir et développer des procédés de fabrication PPF pour des composants automobile désirés à partir d'alliages

d'aluminium et d'aciers à haute résistance. La première étape dans l'élaboration d'une nouvelle application devra être la sélection du matériau ainsi que la caractérisation et la modélisation de son comportement par des lois constitutives valides pour des vitesses de chargement allant du chargement quasi-statique à une vitesse de 10^4/sec. La deuxième étape doit être de prédire les limites de formage pour les différentes vitesses de déformations du procédé PPF ainsi que pour différents niveaux de déformation. La troisième étape doit être la conception du procédé pour atteindre les vitesses de déformation nécessaires pour former le composant automobile donné à partir du matériau sélectionné. De cette façon, le procédé de formage peut être conçu pour fournir le comportement en déformation désiré, ce qui permettra de capitaliser sur ce comportement pour maximiser la formabilité.

2 Introduction

The motivation of this work is reducing transportation vehicle weight as a key enabler to reducing the fuel consumption of automobiles and light trucks. This can best be achieved by using more lightweight materials in vehicles. However, forming of lightweight materials such as aluminum alloys, magnesium alloys, and higher strength steels can be more challenging due to lower inherent ductility in these materials during sheet metal forming as compared to commonly used steel materials. The purpose of this work is to develop pulse pressure forming (PPF) sheet metal forming technologies to more cost-effectively manufacture body-in-white and closure panels made from aluminum alloys and high strength and advanced high strength steel (HSS and AHSS). The most common PPF processes being developed include electromagnetic forming [1, 2], electrohydraulic forming [3], and laser shock forming [4]. These PPF technologies develop in-process strain rates that are usually two to five orders of magnitude higher than conventional metal forming. These high strain-rate processing techniques have the capacity to extend the ductility of metallic materials, which results in component integration and lower part counts through increased formability, use of lower-cost single-sided tooling during manufacturing, and the ability to reduce springback during manufacturing of higher strength and lower elastic modulus metals. PPF will enable more cost effective manufacturing of lightweight vehicles if deployed successfully.

Figure 1 illustrates three critical attributes and the interdependency of these attributes that ultimately influence the formability of materials during sheet metal forming:

- *Process Design* imposes the pressure pulse, material constraints, and the forming dies that will ultimately create the desired shape of the sheet metal component
- *Deformation Behavior* of the material is defined by the material velocities, strains, strain rates, and die impact velocities that results from the process design
- *Constitutive Relations* of the materials will define the resulting flow stress as a function of strain hardening, strain rate sensitivity, anisotropy, and adiabatic heating of the subject material

These three factors interplay and influence each other during sheet metal forming processes, and collectively they primarily define the resulting material formability. All three of these critical attributes can vary highly under PPF. The formability, failure modes, and constitutive relations of most metallic materials can be dramatically different as a result of the higher PPF process strain rates. This is particularly true for many emerging automotive materials such as aluminum and AHSS.

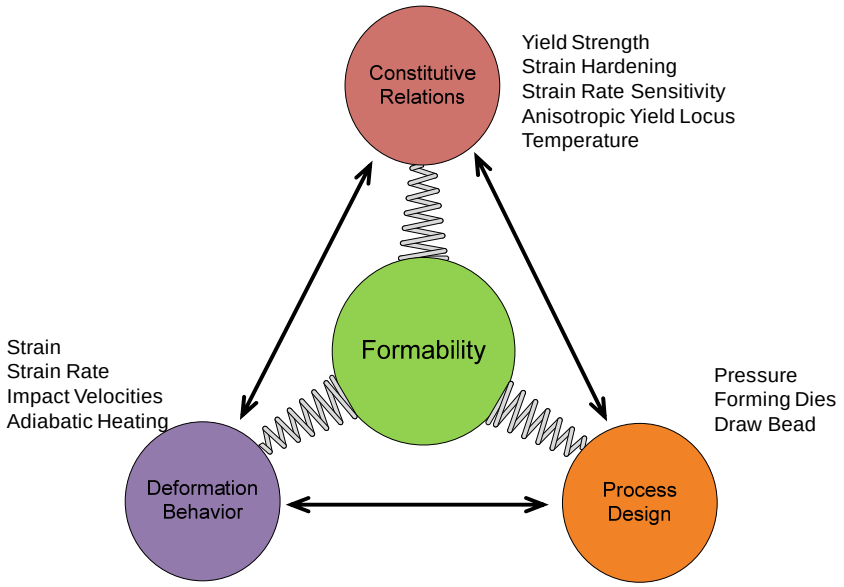

Figure 1 - Formability of sheet metal is primarily dictated by three critical attributes and their interplay

There are multiple emerging manufacturing techniques that involve high-rate metal forming of body-in-white and closure panels (as well as other metallic components). Figure 2 illustrates the relative comparison of strain rates during processing and other applications/events. PPF is a high rate metal forming process whose nominal strain rate is believed to be in the range of 10^2-10^4/s. In general, this is viewed to be three orders of magnitude higher in strain rate than conventional metal forming, and as much as two orders of magnitude higher in strain rate than typical automotive crash events. The formability, failure modes, and constitutive relations of most metallic materials can be dramatically different as a result of the higher PPF process strain rates. This is particularly true for many emerging automotive lightweighting materials such as aluminum, magnesium, and high strength and advanced high strength steel (HSS and AHSS). The understanding of these processes and material behavior during processing must become more comprehensive prior to routine deployment of these technologies for high-volume closure panel and body-in-white applications.

High rate forming methods have been shown to extend the forming limits of a number of sheet materials when compared to conventional die stamping. While EMF works most effectively with sheet materials having high electrical conductivity (aluminum, copper), other technologies (e.g. EHF and LSF) use a high energy discharge to generate pressure pulses (in water or air) that drive sheet metal into single-sided dies. Therefore the processes can be effectively used to form less conductive sheet materials such as magnesium, steel, titanium, and stainless steels. Several approaches can be used to generate a forming pressure pulse, including electrical discharge and laser energy. The high energy, short duration pressure pulses are the mechanism to form sheet material (or tubes) into a die and final shape. PPF is often done in multiple steps, or “bumps”. Although the benefit of PPF on

the ductility and forming limits of sheet materials is generally accepted, very limited quantitative information on the forming envelope of automotive sheet materials has been generated.

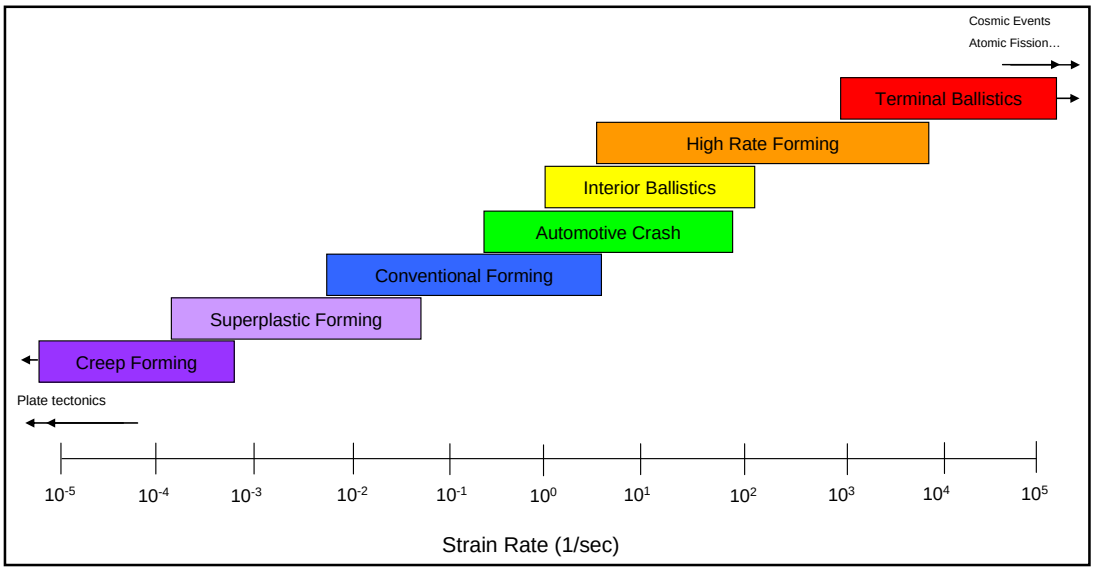

Figure 2 - General illustration of the strain rates of common metal forming and other events.

This thesis is structured into primary chapters in the remainder of this document. Chapter 3 contains the results of a literature review, which discusses past research and development to investigate and describe elements of PPF. The literature review works sequentially through investigation of the process and attributes of the process, constitutive relations, and predictive modeling of the formability limits of material subject to PPF. Chapter 4 contains original research directly investigating the process and the materials subject to PPF processes. This work involves developing a unique experimental apparatus and testing automotive sheet material formability in this apparatus. Chapter 5 presents an original experimental investigation of the constitutive relations of the subject materials, and develops a new constitutive model to describe these materials over six orders of magnitude of strain rate. Chapter 6 develops methods to conduct predictive modeling of the forming limits of automotive sheet materials subject to PPF, and parametrically analyzes the formability of the materials given different forming conditions and constitutive relations. Chapters 7 and 8 contain overarching discussion and conclusions from this work.

3 Literature Review of Pulse Pressure Forming

There has been significant past research and development to investigate and describe elements of PPF. This chapter divides the past work into five major elements. The first three elements of the literature involves characterizing and defining the methods and processes that result in PPF (Chapter 3.1), characterizing PPF formability enhancements reported in the literature (Chapter 3.2), and understanding methods to measure metal deformation during PPF processes (Chapter 3.3). The fourth major element of the literature review investigates prior work performed to experimentally investigate the constitutive relations of the materials subject to PPF, and describing these relations across a wide range of strain rates (Chapter 3.4). The fifth major element of the literature involves attempts to develop and validate generalized formability models for sheet metals that are subject to PPF (Chapter 3.5). Each of these elements of literature will be described separately in the sections below.

3.1 State of the Art of PPF Processes

Daehn [16] conducted a recent review of various high-rate forming techniques. High strain-rates have been shown to enhance the formability (relative to formability at quasi-static strain-rates) of sheet metal in many instances. High strain-rates for sheet forming are typically obtained by techniques such as explosive forming, electrohydraulic forming (EHF) and electromagnetic forming (EMF). Explosive forming is sufficiently expensive and carries inherent worker safety issues that it is not being seriously investigated as a commercial automotive manufacturing technology. This work considers the two technologies that appear to have the highest degree of commercial relevance for high-volume manufacturing: EMF and EHF. Since they are significantly different technologies, the state of the art of the processes need to be treated separately.

3.1.1 Electromagnetic Forming

Electromagnetic Forming (EMF) is perhaps the most heavily researched and widely deployed type of PPF technology. Psyka et al [17] describe EMF as an impulse or high-speed forming technology that uses pulsed magnetic field to apply Lorentz' forces to workpieces without mechanical contact or working medium (i.e. without water or rubber contact). EMF is most suitably applied to workpieces that are made of a highly electrically conductive material, such as aluminum and copper alloys since the workpieces must support a high current density during the process.

One of the earliest applications of the EMF technology was developed and documented by Harvey and Brower [18] in a United States patent application. Figure 3 contains a select set of figures from this original patent, which showed three general configurations of the EMF process. The top left of the figure shows the concept where an initially flat sheet metal is placed against an EMF coil that is also flat. In this configuration, an electrical current pulse is discharged through the coil and creates a pressure pulse that drives the sheet metal into a die opposite the coil. This is likely the most relevant type of forming process that is applicable to the automotive manufacturing industry. In this configuration there is the possibility of manufacturing sheet metal components using EMF as an alternative to conventional stamping or deep drawing. Also shown in figure 3 are two additional

applications where coils are used to either expand a tube into a die (top right), or shrink a tube down to a mandrel configured to a particular shape (bottom left). Each of these configurations has some advantages over conventional tube expansion or swaging operations by enabling both extended ductility and noncontact pressure pulses. This early work was important for establishing the methodology that would be investigated and developed by others later for more sophisticated applications with greater commercial relevance.

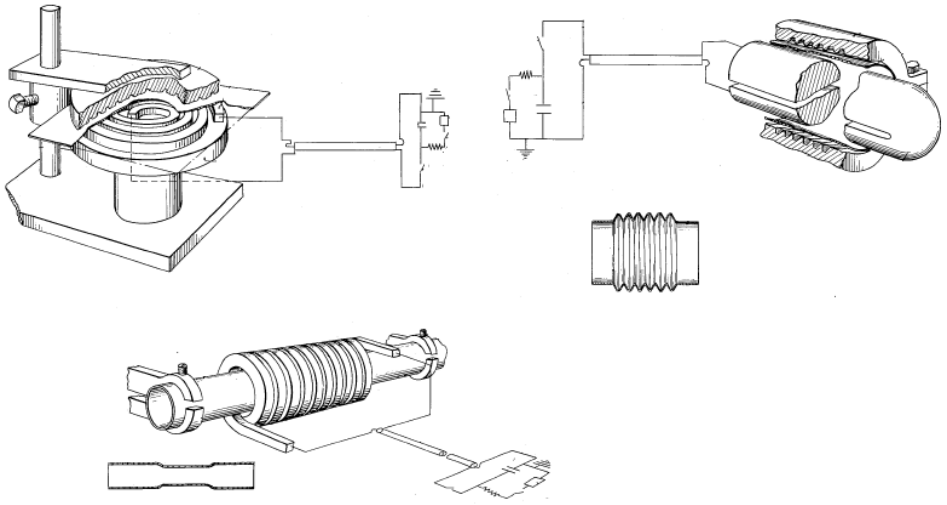

Figure 3 - Early documentation of the application of EMF [18].

Psyka et al [17] describe conventional single-step EM forming methods using flat sheet as typically involving the following elements and process characteristics:

- Stored electrical energy in low inductance, high capacitance circuit. Figure 4 illustrates a basic circuit diagram for an EMF capacitor bank with both a charging power supply and a discharge switch for releasing the stored energy into the coil.
- The capacitor bank discharges electrical energy through a low inductance switch/bus to a working coil (inductor)
- A transient magnetic pulse induces electric current though the coil and repels the conductive workpiece away from the coil. Figure 5 illustrates the typical coil assembly with the LRC circuit and current flow through the coil.
- A pressure pulse, with duration estimated to be 50-200 μs, accelerates the workpiece to velocity on the order of 100 m/s. Figure 5 shows how the sheet metal is proprolled from the initially flat sheet to a formed dome.
- The dynamic event typically results in increased ductility.

- The dynamic interaction of the workpiece with the die leads to further ductility enhancement as well as reduced springback.

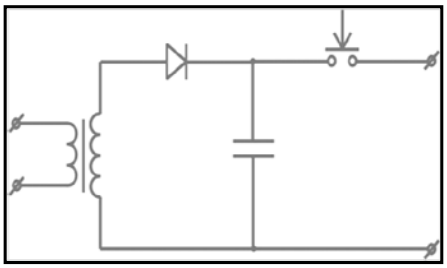

Figure 4 - Typical capacitor bank charging circuit and discharge switch for EMF process.

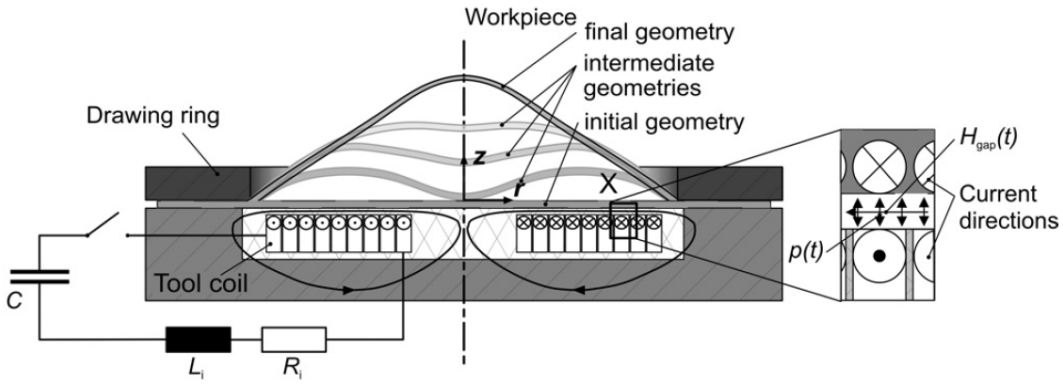

Figure 5 - Illustration of sheet EMF process from Beerwald et al [20]

Figure 6 shows a concept where a single coil operating on an initially flat sheet will propel the sheet into a highly contoured single-sided die in order to produce the sheet metal component desired. This has been the approach of many of the most significant research endeavors in the past [5, 17, and 19]. Under this metal forming scenario, the single electromagnetic pulse will need to be sufficient in magnitude and shape to fully form the part from initially flat to fully matching to the contour of the die. Delivering this magnitude of energy to the coil may damage the coil itself during the forming event. Therefore, significant research has been dedicated to finding ways to reduce the size of the energy pulse that the coil must endure; while still maintaining the ability to form highly-contoured parts at high strain rates.

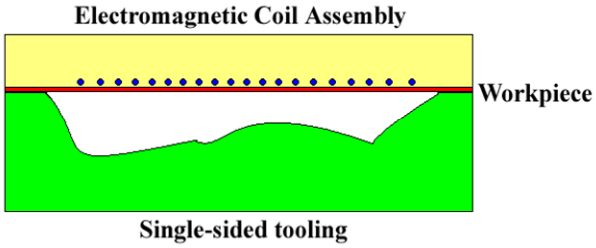

Figure 6 - Conceptual applications of EMF where an initially flat sheet is driven by a flat coil.

Golovashchenko et al. [21] introduce a two step forming method where a stamped component is submitted to EMF to create the final, detailed features in an automotive component. Their general concept was to use conventional stamping to make a nearly completed part, and subsequently use an EMF coil and die to produce the difficult-to-form local feature on the part. This allows for minimizing the coil size and the overall size of the press and supporting manufacturing equipment to make parts. An alternative approach to using a secondary process to implement EMF after stamping is to embed coils into the forming punch to allow a two-step process in one forming operation. Figure 7 is a concept where EMF coils are embedded in a punch, where the EMF process is initiated after the conventional stamping portion of the operations has concluded. Similar to Golovashchenko et al. [21], the intent is to utilize small coils and modest current pulses to employ extended ductility in localized areas where the most challenging forming exists.

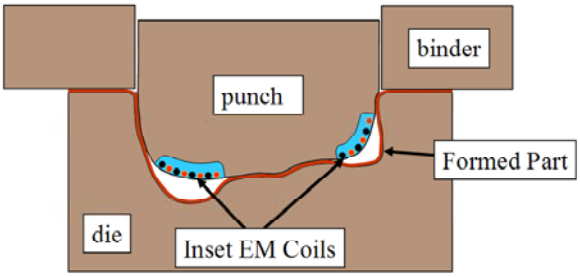

Figure 7 - Conceptual applications of EMF where EM coils are inserted into a conventional punch to form local areas.

A final variation of the EMF process uses EMF coils embedded in the forming punch and discharges the EMF process intermittently during the forming operation [22]. In this case, the deforming sheet makes contact with the forming punch, and then a large area forming coil is discharged to effectively drive the material away from the punch.

A final consideration for high-volume automotive manufacturing is managing the heat imparted to the EMF coil assemblies during forming at high energy levels and low cycle times [1]. The materials most commonly used to make EMF coils are copper and bronze, with perhaps aluminum alloys and steels employed less often. These materials all possess an electrical resistance that generates heat during discharge of the capacitor bank through

the coil. This results in heat generation that can be problematic with rapid, successive forming events at low cycle time. Therefore, research and development efforts have investigated cooling methods.

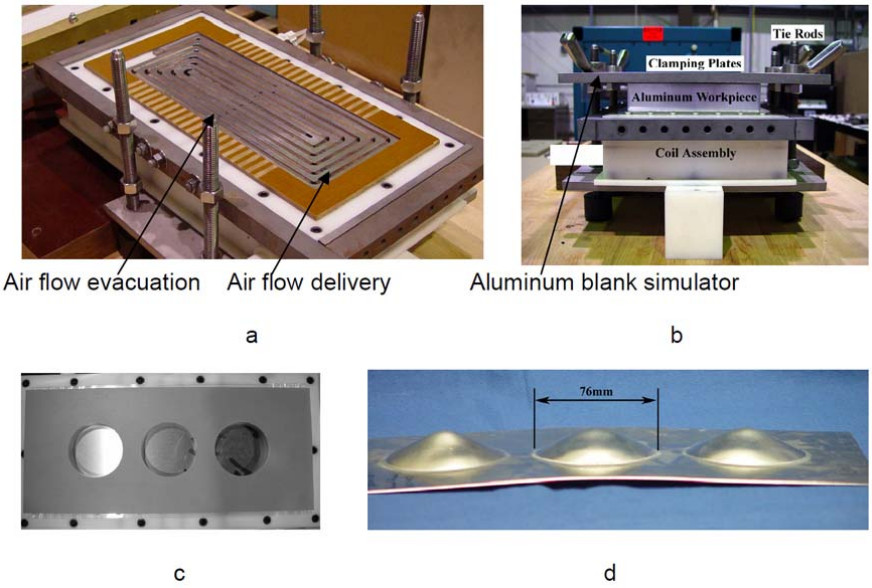

Figure 8 - Experimental fixture employed for an experimental study of coil durability and heat accumulation: a – flat coil with air cooling system; b – assembled fixture for testing coil durability; c - experimental die for estimating the energy of the coil testing procedure; d – formed blank [1]

Figures 8a and 8b shows a low cost cooling assembly designed for high-volume automotive sheet metal manufacturing [1]. This assembly was used to investigate the cooling process, and was conducted using a flat EMF coil made of steel with micarta (canvas reinforced phenolic) insulation plates. Air flow was delivered through the slots between the micarta plates and in the corners of the coil. The spiral surface was insulated from the blank by a thin plate of insulation material. The air flow was directed between the spiral surface and insulation plate so it would provide cooling of the working surface of the coil where a maximum amount of heat is generated. In this experimental study, the energy of the process was specified based upon the energy needed to form cones made of 1 mm thick aluminum sheet into the die (figure 8c) with open round windows 76 mm in diameter (figure 8d). In a durability study the aluminum blank was replaced by an aluminum plate which was clamped to the coil with four bolts, as indicated in Figure 8b. An experimental study showed that after 5000 discharges the coil did not have any signs of damage and, therefore, has the potential to be used in high volume production conditions.

EMF has been actively investigated and developed for more than 50 years. There have been many alternative approaches used to employ EMF. This work has resulted in limited commercialization of the technology in the automotive manufacturing industry. However, as will be shown later, the ability to achieve enhanced formability using the process remains attractive to manufacturers. However, alternative methods exist to achieve high energy pressure pulse and rapid method forming.

3.1.2 Electrohydraulic Forming

The technology of Electrohydraulic Forming (EHF) appears at approximately the same time as EMF in the 1950s and early 1960s. According the Golovashchenko et al. [21], the EHF forming process was originally developed by Yutkin [23]. This technology received much attention from researchers in sheet metal forming in 1960s [24-26], and multiple methods of apply EHF technologies are described by Bruno [27] in 1968. Most of this early work was investigating methods to exploit the observed ductility enhancement in materials subject to EHF.

Figure 9 illustrates a simple EHF process. The pulsed electrohydraulic forming is an electrodynamic process based upon high-voltage discharge of capacitors between two electrodes positioned in a fluid-filled chamber. The electrical discharge is believed to result in the vaporization of a small volume of the liquid and/or plasma creation, which results in a high intensity, high velocity shock wave in the liquid. The shock wave is directed toward a sheet metal workpiece, which is ultimately driven into a die to create the part of the desired shape. A critical advantage of EHF over EMF is that the process does not lose process efficiency when the electric conductivity of the workpiece is low; such as when subjecting steel to EMF.

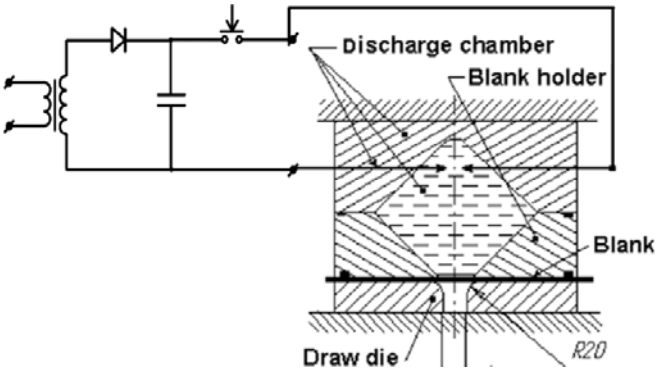

Figure 9 - Schematic of the EHF process in a simple arrangement.

Oyane and Masaki [28-30] conducted a series of basic experiments to gain understanding of the pressure pulse and the general physics of EHF forming. In their initial work [28], they conducted a series of experiments to investigate the intensity of the pressure pulse generated during EHF as a function of the electrode geometry, as well as investigating the influence of placing a small pilot wire between the two electrodes to better enable the discharge of energy between the electrodes. The results of this work concluded that varying the geometry of the electrode set up had little influence on the shape of the pressure pulse, which had 5 μs rise time and a 15 μs duration. In the same work, they also concluded that introducing a small wire between the electrodes increase the efficiency of the discharge, with a fine aluminum wire appearing to maximize the intensity of the pressure pulse. They concluded that efficiencies were relatively low when no wire was placed between the electrodes to initiate the pressure pulse, and that the aluminum wire was most efficient because of the relatively low boiling point and low heat of vaporization of the material. Oyane and Masaki [29] also concluded that the performance of the pilot wire between the electrodes was influenced both by the charge voltage of the capacitor bank as well as the elemental composition of the wire itself. For example, tungsten wire had the effect of creating a second

more intense pressure pulse in the chamber with increasing charge voltage, whereas aluminum and copper wire appeared to have no such effect.

In their final publication on the topic, Oyane and Masaki [29] conducted a systematic investigation of the charge voltage of the capacitor bank as well as changing the characteristics of the LRC circuit that comprised the overall forming system. In this work, they conclude that the shape of pressure pulses is dependent on the LRC circuit characteristics, and investigated the pilot wire diameter for copper wires to yield a rise time of the pressure pulse being approximately 4 μs and its duration being approximately 10 μs. However, the magnitude of the pressure pulse is influenced by both the wire diameter and inductance of the LRC circuit used in the forming equipment. They further conclude that when the charge energy to vaporize a wire is sufficiently large, larger wire diameters result in larger pressure pulses as well as an overall increase in the efficiency of the process. Figure 10 shows a summary of the EHF shock wave energy versus system charge energy with different copper wire diameters and system inductance. The figure shows the greater shockwave energy is produced using increasingly larger diameters of copper wires introduced between the electrodes in the forming system, and generally that the lower inductance of the forming system has advantageous effects on shockwave energy.

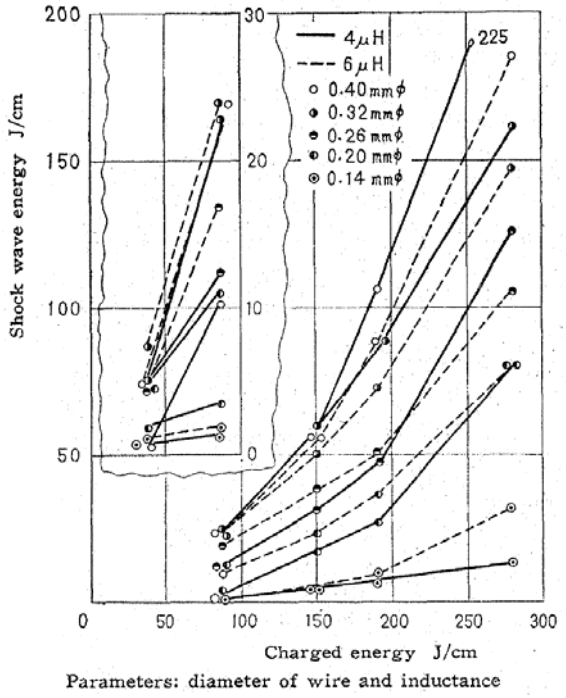

Figure 10 - Illustration of the shock wave energy of EHF versus the charge energy in the system from Oyane and Masaki [29]

More recent investigation for laboratory scale EHF has been performed by Balanethiram et al [31-33]. This work focused on the formability of interstitial free (IF) iron, copper, and aluminum alloy sheet materials using in the EHF forming system. This research team investigated the formability of the sheet materials using a forming blank with approximately 100 mm diameter domes that were driven into a conical die. They concluded that enhanced

ductility was achieved using this EHF process, and in some cases the formability improvement was 2 to 3 times more than material formability under free forming conditions at quasistatic strain rates. This research team primarily focused on the velocity of materials undergoing deformation, and referred to the phenomena of extended ductility at high velocity as *hyperplasticity*. This research always involved contact of the sheet material with a die during the forming event, but does not appear to differentiate formability of materials that contacted the die from the free forming formability determined under quasistatic testing. Later in this work, the importance of differentiating formability of materials under free forming and die contact conditions will be discussed.

Most of the technical work on EHF has focused on using an apparatus with a single set of electrodes inside the metal forming chamber. Golovashchenko et al [34] introduced the concept of using an array of electrodes within a single or across multiple chambers in order to affect a pressure pulse across a wide region or area of a workpiece. Figure 11 illustrates this concept; where the individual electrodes are spaced within a forming chamber in order to form a rectangular pocket into a work piece. In this particular case, the application was the liftgate of an automotive structure, which was not formable using conventional metal stamping technology. However, this work does not address the specifics of the forming process and is limited to a conceptual overview of the process and how it might be applied commercially. The question of how to initiate the forming event across multiple electrodes either separately or simultaneously is not addressed. However, Golovashchenko et al [34] did describe a key advantage of EHF over EMF, which is the ability to incrementally form a component through multiple EHF pulses into a single die cavity. Thus, by allowing the addition of water into the expanding EHF cavity, a succession of EHF discharges can incrementally form the component into a die. Using this methodology, their team was able to completely form a part made of aluminum sheet metal that was otherwise incapable of being manufactured using EMF.

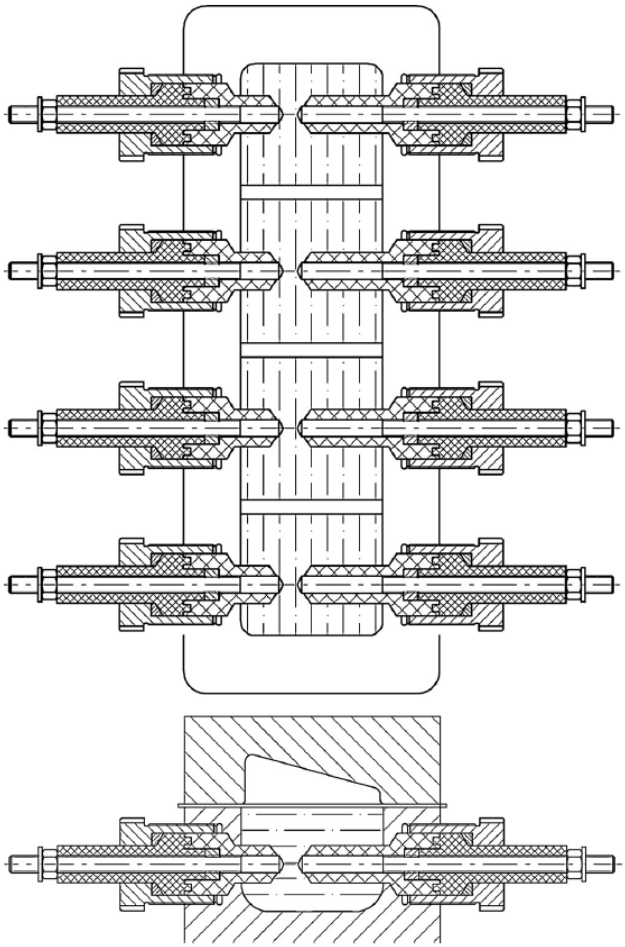

Figure 11 - Multiple electrode forming chamber from Golovashchenko et al [34].

3.2 Formability Enhancement during PPF

The primary commercial motivation for utilizing PPF technologies is the ability to achieve extended ductility in sheet metals beyond what is capable under quasi-static forming conditions. Therefore, much of the prior investigation has focused on determining the forming conditions and processes necessary to achieve extended ductility. However, there exists significant variability in the results reported in the literature regarding extended ductility.

The more recent EMF works in the literature has yielded some important process developments in understanding. There are three primary conclusions in the technical literature from experimental investigations on the formability of sheet metals and tubes under PPF processing. These conclusions, which in some cases contradict each other, are:

1. Limited or no ductility enhancement being observed during free forming (without dies)

2. Major ductility enhancements being observed during free forming (without dies)
3. Major ductility enhancements observed with forming die contact (initial free forming with die impact)

The conclusions 1 and 2 imply contradictory data about the ability to achieve enhanced formability when using free forming of sheet metals without dies, as the conflicting data is found in the literature. One of the most notable reported increases in formability in free forming experiments was that reported by Tobe et al. [35, 36]. They used EHF free forming to investigate the high strain rate deformation behavior of different aluminum alloys. There results indicate that the forming limit increased by approximately 35% for alloys that showed strain rate dependence in their mechanical properties. Golovashchenko et al. [34] compared the rate-dependence of formability of several materials (Al, Cu, steel and Ti alloys) and observed that EHF into an open die (free-forming) could increase the local deformation by 40-90%. More recently, Oliveira [19] concluded that the role of high rate forming under free-forming conditions showed no significant increase in formability for free formed aluminum alloys. Imbert et al. [37, 38] showed that enhanced ductility was achieved during free forming experiments that were carried out on 1 mm AA5754 sheet, which yielded safe strains beyond the conventional forming limit diagram (FLD) in a narrow region in the free form experiments. The ability to achieve extended ductility in free forming conditions in aluminum alloys is still a matter of technical debate in the literature. Moreover, the exact forming conditions and material properties that result in extended ductility are not well understood. Chapter 4-6 of this thesis will directly address this technical question. However, the literature is much more consistent on the results of PPF into a closed die cavity.

Golovaschenko et al [21] show that enhanced ductility could be achieved by forming sheet metal into a V-shaped die, where enhanced ductility was not seen using an open or free forming condition. Imbert et al. [37, 38] also showed that enhanced ductility was achieved by including die contact as part of the forming event. They studied the effect of die–sheet interaction on damage evolution in aluminum alloys during EMF, and conducted conical die forming experiments using 1 mm AA5754 sheet. They determined that enhanced ductility was present in a significant region of the sheet metal when forming into a conical die. This suggests that the die–sheet interaction is likely to play a significant role in the reported increases in formability of parts formed into a die. Furthermore, the majority of recent formability-related research has employed EHF and EMF techniques that incorporated die contact to enhance formability. For example, Balanethiram and Daehn [31] deformed interstitial free (IF) iron into a conical die (90° apex angle) using EHF technique and measured engineering plane-strains on the order of ~160% near the fracture region and ~120% away from the fracture. Figure 12 illustrates these results where the high rate data shows a major increase in formability compared to the quasi-static forming limit strains in IF iron, which is typically 30-40%. Using the same EHF procedure, the same authors in subsequent publications [32, 33] observed large plane-strains near failure in 6061-T4 aluminum (~engineering strain ~120-130% at high-rate vs. ~20% at quasi-static rates) and in oxygen-free high-conductivity copper (engineering strain ~100% at high-rates vs. ~30% at quasi-static rates).

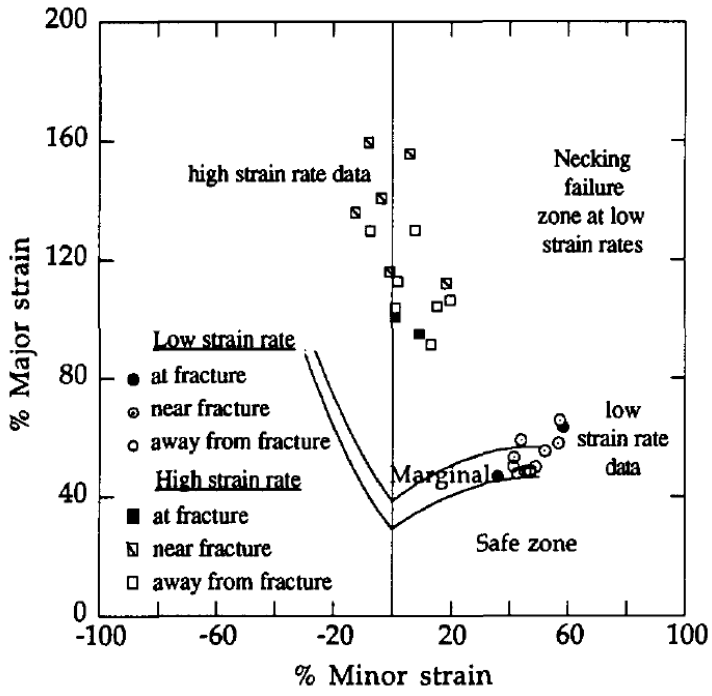

Figure 12 - Forming Limit Diagram comparing low strain and high strain rate forming data for interstitial free Iron from Balanethiram and Daehn [31].

Further evidence exists that die interaction is a major factor for the existence of extended ductility. Seth et al. [5] used EMF to impact steel sheets on axisymmetric and wedge-shaped dies and measured engineering plane-strains at failure to be ~50-60% as compared to ~10% under quasi-static deformation. Golovashchenko et al. [34] also observed higher failure strains (~60% strain at high-rates vs. ~25% at quasi-static rates) in 6111-T4 Al when using the EMF technique and forming the Al sheet into a V-shaped die. Imbert et al. [38] investigated EMF of AA5754 sheet into an open die (free-forming) and a conical die (112° apex angle) and observed maximum strains on the order of ~35-45% at high rates as compared to quasi-static strains of 20-30%. In another study, Imbert et al. [37] measured maximum engineering strains of ~65% for AA5754 formed by the EMF technique using free forming and conical die forming (100° apex angle), as compared to quasi-static strains of ~20-30%. Figure 13 shows the formability of an EMF dome produced via free forming, and the varying strain across regions of the dome on an FLD. In other work, Oliveira and Worswick [39] measured maximum engineering strains of ~40-50% when forming AA5754 by EMF into a rectangular die.

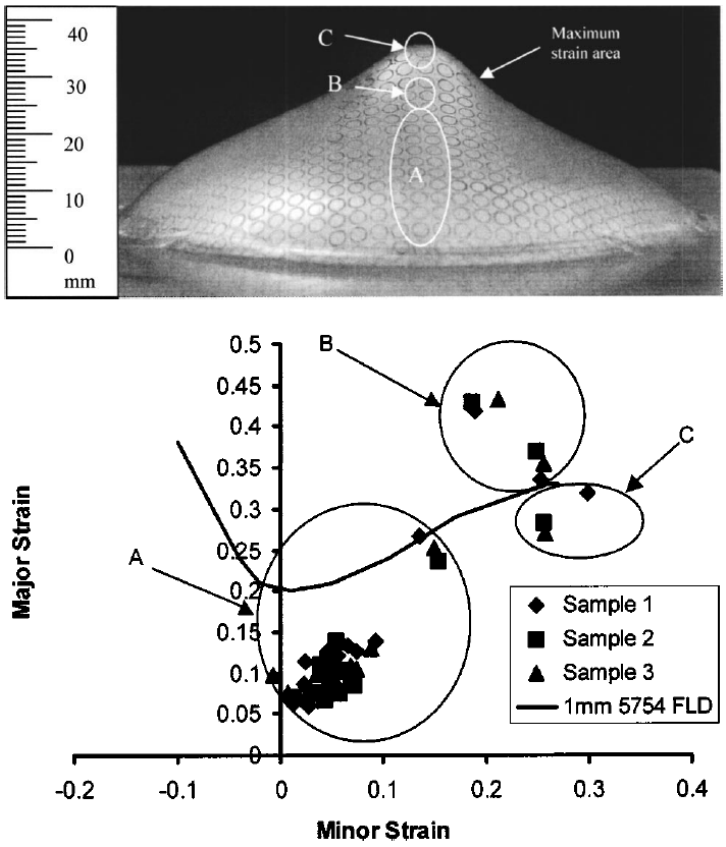

Figure 13 - Results of EMF free forming experiments from Imbert et al [37]. Photograph shows the strain grids on a deformed specimen and regions A, B, and C. The FLD shows the experimental formability of these regions.

The formability of high strength steels at high strain rates has been much less characterized than that of the aluminum alloys. Kim et al [40] investigated the formability of the high strength steel DP590 at quasistatic and elevated strain rates. Figure 14 contains the comparison of these FLDs. These results show little change in the FLD across these strain rates, and perhaps even a slight decrease in formability at the elevated strain rates. However, the maximum strain rates in this work are approximately one order of magnitude below the strain rates typically associated with PPF.

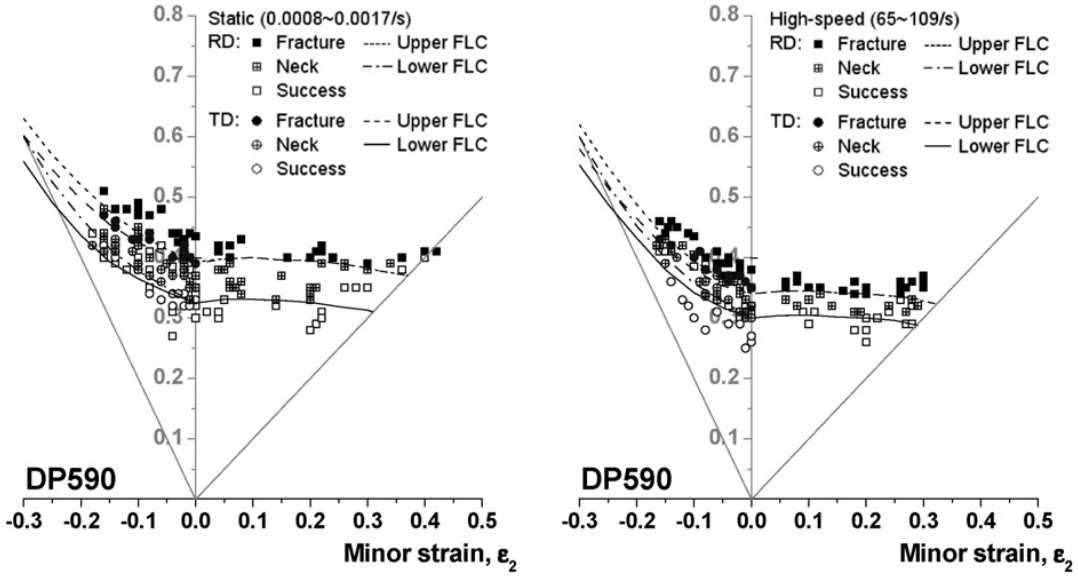

Figure 14 - Comparison of the FLD for DP590 at quasistatic strain rates and intermediate strain rates from Kim et al [40].

Thus, the observation of increased formability at high-strain-rates has been generally established in the literature for materials that are formed into a closed die where contact occurs during forming. However, the quantification of deformation history of the sheet metal, subjected to high-rate deformation, has not been clearly established. Additionally, the general understanding of how enhanced formability is achieved in free forming conditions requires further definition. This further understanding of the enhanced forming will require a greater understanding of the actual strains, strain rates, velocities, and temperature of the materials subject to forming.

3.3 Measuring Strain and Velocity during PPF

The formability in high-rate deformed sheets is typically determined by measuring strains using the circle grid analysis, as outlined by Taylor [41]. While this strain-measuring technique determines the final strain distribution in the deformed sheet, it is unable to determine the strain and strain-rate history at different sheet locations. Consequently, there is lack of in-process deformation behavior in the literature, which has contributed to a lack of consensus on the mechanisms responsible for the enhanced-formability in sheet metals.

Balanethiram and Daehn [31] estimated sheet metal peak velocities of 300 m/s and a strain rate of ~1050 /s during EHF of IF steel sheet, and they attributed formability improvement to inertial stabilization on account of high velocity. These authors estimated similar velocity and strain rates, as well as similar conclusions for EHF tested 6061-T4 Al and OFHC Cu [32,33]. Seth et al. [5] experimentally measured the impact velocity of steel sheets on a steel punch and attributed the enhanced formability to inertial stabilization and compressive stresses generated during impact, though strains were still measured by the conventional etched-circle grid technique [41]. Other authors, [3, 34, and 42], determined only the post-mortem strain via the etched-circle grid technique in EMF and EHF experiments. They attributed the observed improvement in sheet formability to high strain-rates

and high-rate impact with the tooling. However, these authors had no direct measurement of the strain and strain-rate history of the deforming sheet.

Imbert et al. [37] numerically modeled EMF of Al alloy sheet and concluded that high-strain rates and inertial stabilization alone could not be responsible for enhanced formability. They estimated the strain rates to be on the order of 30,000-69,000/s in the locations where sheet impacts the die. Further, they claimed that high through-thickness compressive and shear stresses and strains as well as non-linear strain-paths were the responsible factors for enhanced formability of the materials during PPF. However, the authors noted that such conclusions about extremely high strain-rates and strain-path need to be validated experimentally. Finally, modeling efforts, such as those by Oliveira and Worswick [39], tend to validate their numerical models using final strain distribution as the key criterion, but they generally neglect the prior strain and strain-rate history owing to the lack of corresponding experimental data.

There has been some recent progress in obtaining deformation-history from high-rate forming experiments. Daehn et al. [6] used Photon Doppler Velocimetry (PDV) that appears to offer significant advantages over other techniques. In this system, newly available fiber optic lasers and components as well as higher speed oscilloscopes are applied. Daehn et al. [6] consider this a technical breakthrough in robust and inexpensive velocity measurement during high speed forming. Johnson et al. [43] used the Photon Doppler Velocimetry technique in electromagnetically expanding ring experiment to determine in-process velocity versus time at four locations. However, the authors did not demonstrate the actual strain or strain-rate history for the expanding rings from this data, as there data is limited to velocity and does not yield full field strain measurements.

Mercier et al. [44] used VISAR and Doppler Laser Fabry-Pérot Interferometry technique to measure velocity (at 3 locations) during explosive-driven expansion of tantalum and copper hemispheres, respectively. Again, experimental strain or strain-rates could not be determined by their method. Wielage and Vollertsen [45] used high-speed imaging to determine velocity of laser shock formed metal foils (20-50 μm thick) that were subject to bending and used geometrical arguments to estimate the total bending strain and the corresponding strain-rate. Finally, Badelt et al. [46] developed a method that uses contact-pins and laser-shadow methods to determine displacement-time history of individual locations on a sheet during electromagnetic forming. However, their method was unsuitable for direct measurement of strains and strain-rates and necessitated the use of mathematical modeling to estimate the same.

The measurement of the forming conditions during EMF has been performed using several methods in the past. However, no reports were found in the literature where real-time strain and strain rates were measured directly on the deforming materials. Most cases appear to measure the strain that developed in the material at the end of the forming event, and then use process simulations or other indirect methods to estimate or approximate the real-time strain and strain rate of the materials. Thus, it is concluded that prior research has principally relied upon final strain measurements, and estimated strain-rates and numerical models to postulate mechanisms responsible for enhanced formability. Further, the numerical models themselves are validated by the post-mortem strain measurements and neglect the prior strain and strain-rate history. Chapter 4 of this thesis

develops a full-field, real-time measurement of strain, strain rate, and velocity of the materials in-situ to the forming event.

3.4 Constitutive Relations during PPF

The constitutive relations of materials during PPF is a particular technical challenge as the strain rate ranges from quasistatic up to perhaps 10^4/sec (though the literature varies significantly on the peak strain rate). The mechanical properties of most metals are rate dependent, and can display wide variations in strain rate sensitivity across this range of strain rates. Furthermore, the high rate forming can result in adiabatic heating of the materials, which is usually not experimentally measured during testing. Aluminum alloys are a prime example of the varying strain rate sensitivity across a wide range of strain rates.

Higashi et al. [47] used hydraulic tensile machines and Split Hopkinson Pressure Bar (SHPB) to determine the room temperature uniaxial tensile behavior of annealed AA5182 across the strain-rate range of $1x10^{-3}$/s to ~$2.5x10^3$/s. Figure 15 shows the summary of the results across the ranges of strain rate and plastic strain. The definition of strain rate sensitivity throughout this work is $m = \log(\sigma_2 / \sigma_1) / \log(\dot{\varepsilon}_2 / \dot{\varepsilon}_1)$[48]. The figure shows that the material exhibits negative strain rate sensitivity (a reduction in flow stress) from quasistatic strain rates up to approximately 10^1/s. Furthermore, the data shows that the strain rate sensitivity of the material becomes increasingly positive (and with increasing flow stress) at strain rates above of 10^2/s. Moreover, Higashi et al. [47] showed that at strain rates above 10^3/s that the increase in flow stress and strain rate sensitivity increased dramatically relative to quasistatic or intermediate strain rates.

Figure 15 also shows that the rate of hardening of the materials appears to be relatively consistent across the strain rates tested. The multiple curves in figure 15 showed that the strain of 0.05 has a similar shape to the strain of 0.20. The general trend in the data shows that the strain hardening of the materials remains relatively similar across the entire screen rate regime tested for these materials. This relatively consistent strain hardening is later exploited in the constitutive model developed for these materials in Chapter 5.

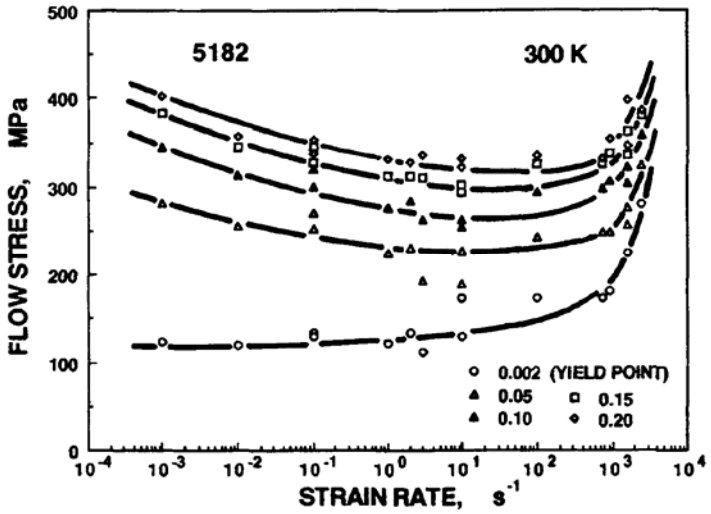

Figure 15 - Flow stress of AA5182-0 as a function of strain rate and strain at room temperature from Higashi et al. [47].

Figure 16 shows the results of further work investigating the strain rate sensitivity of aluminum alloys by Higashi et al. [49]. This work shows a relatively consistent trend of near-zero to slightly negative strain rate sensitivity of aluminum alloys in the quasistatic to 10^2/s range of strain rates. In the cases shown, the low alloy materials (1050, 3003, and 3004) show lower overall flow stresses and less tendency for negative strain rate sensitivity at the quasistatic strain rate ranges. The more highly alloy materials (5182 and 7N01) show a greater propensity for negative strain rate sensitivity in the quasistatic regime, but equal to or higher strain rates sensitivities in the high rate strain rate regime above 10^3/s.

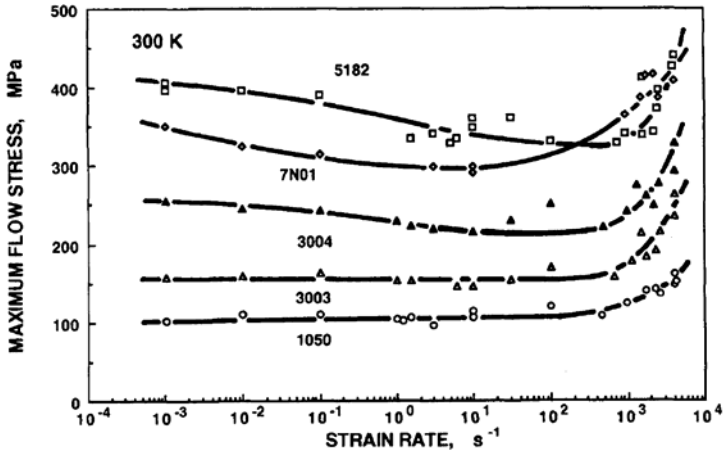

Figure 16 - Maximum flow stress for a set of aluminum alloys as a function of strain rate and strain at room temperature from Higashi et al. [49].

Lin et al. [50] conducted an investigation of the mechanical properties of an Al-6%Mg alloy using a combination of conventional tensile testing and Split Hopkinson Pressure Bar (SHPB). Figure 17 illustrates the results of their

experiments. The data show similar results as those generated by Higashi. Their results show a general decrease in flow stress from quasistatic strain rates until the strain rates approach 10^2/s. The data then shows a reversal of this trend and a general increase in the flow stress of the material with increasing strain rates up to $3.02x10^3$/s. This significant increase in the strain rate sensitivity (as evidenced by the increasing flow stress) is consistent with the results of the material tested by Higashi et al. [47], which is also a high magnesium bearing alloy.

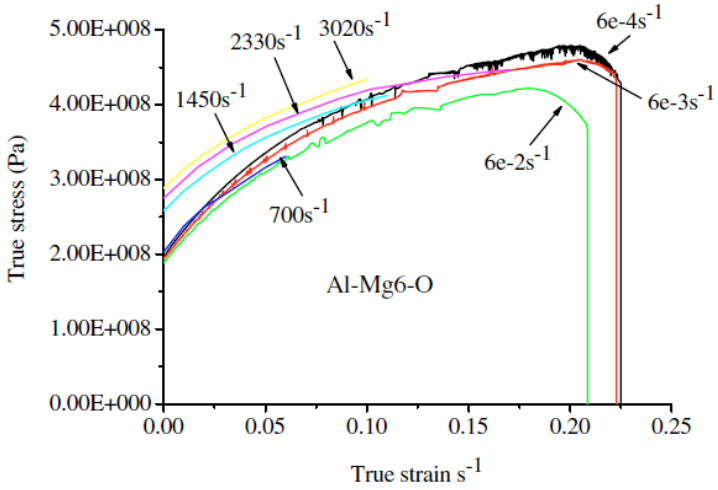

Figure 17 - The stress-strain curve of Al-Mg6-O from Lin et al. [50].

Lin et al. [50] also conducted fractography of their materials. Figure 18 contains a comparison of the fracture surfaces evaluated using a scanning electron microscope (SEM) for specimens tested under quasistatic conditions and $3x10^3$/sec. In this case, the general appearances of the fracture surfaces are very similar, and exhibit classical signs of ductile fracture resulting from void nucleation and growth that leads to coalescence of voids and subsequent fracture. The similar failure surface features indicate that the mode of deformation and failure are similar for these materials regardless of the strain rate regime evaluated up to $3x10^3$/sec. These results are consistent with Imbert et al [37], who showed that conventional damage evolution equations that account for void nucleation and growth during forming adequately describe the failure of materials during EMF. This apparent consistency of microstructural evolution and failure across the entire strain rate regime of PPF is critical to understanding and predicting the forming limits of materials under PPF conditions.

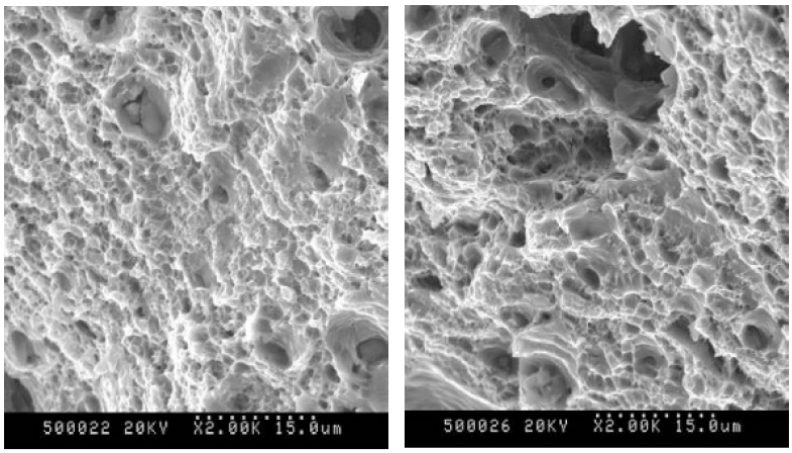

Figure 18 - Al-Mg6-O fracture surface after tensile testing at strain rate of (left) $6x10^{-4}$/sec and (right) $3x10^{3}$/sec from Lin et al. [49].

Mukai et al. [51] also investigated and compared the mechanical properties of a series of magnesium bearing aluminum alloys. Figure 19 shows the comparison of the yield stress of these alloys across the strain rate regime of quasistatic up to $3x10^{3}$/sec. These results show a similar pattern of relatively consistent flow stress up to 10^{1}/sec, and a significant increase in the flow stress in the strain rate regime of PPF. Smerd et al. [52] also conducted a series of experiments to investigate the flow stress of AA5182 and AA5754 aluminum alloys across the strain rate regimes relevant to electromagnetic forming. These authors confirm the constitutive relations reported across the literature, where very low or negative strain rate sensitivity was observed at quasistatic strain rates, and positive strain rates sensitivities of the materials being reported at strain rates above 10^{1}/sec.

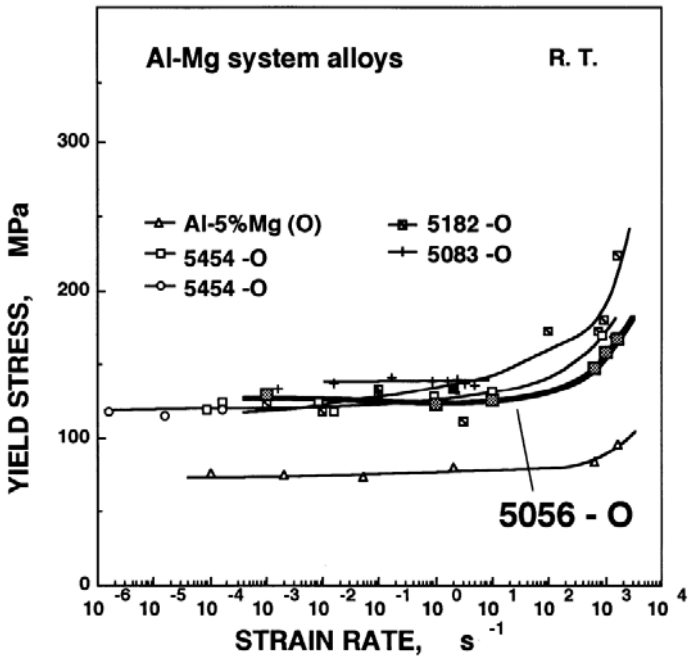

Figure 19 - Yield stress of 5056-O aluminum compared to several other aluminum alloys from Mukai et al. [51].

Many of the aluminum alloys of interest to automotive manufacturing can be considered quasi-single phase materials of relatively low alloy content. Therefore, the relatively consistent constitutive relations that are exhibited above should be expected. However, by comparison, the high strength steels (HSS) and advance high strength steels (AHSS) have significant variations in chemistry and microstructure.

Huh et al. [53] investigated the influence of strain rate on the mechanical properties of TRIP600, TRIP800, DP600, and DP800 steels. The results of this work are shown in figure 20. All four of these materials show slightly positive strain rate sensitivity at quasistatic strain rates, and a moderate increase in the strain rate sensitivity as the strain rates increase. This data shows that the change in strain rate sensitivity appears to be less dramatic in the steels compared to the quasi-single phase aluminum-magnesium bearing alloys report above. However, all four of these materials show a relatively consistent hardening characteristic with increasing plastic strain in the specimens, as evidenced by the relatively consistent and common shape of the curves with increasing plastic strain. This relatively consistent strain hardening across all strain rates help simplify the constitutive models needed to adequately describe the mechanical properties of these materials. The limitation of this particular data is that the investigated strain rate regimes appear to be lower than is typically associated with PPF. However, other investigators have investigated the higher strain regimes necessary to describe the mechanical properties during PPF.

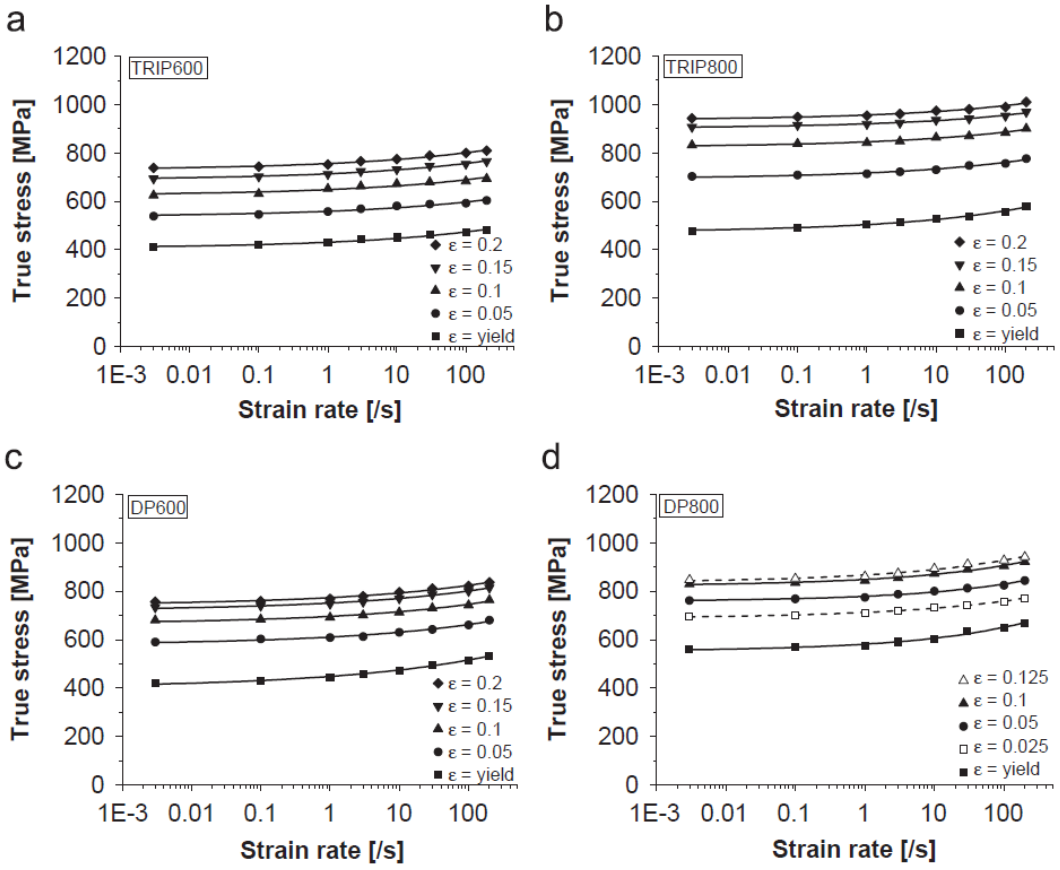

Figure 20 - Strain rate sensitivity curves at various strains: (a) TRIP600; (b) TRIP800; (c) DP600; (d) DP800 from Huh et al. [53].

Yu et al [54] investigated the mechanical properties of DP600 across the strain rate regime from quasistatic up to and above 10^4/sec. Figure 21 contains the results of this external investigation. The data shows relative agreement with the work presented by Huh et al. [53]. However, the additional data in the high rate regime show that there exists a general increase in flow stress with increasing strain rate even above the intermediate strain rates investigated by Huh et al. Therefore, the strain rate sensitivity of the materials appears to be positive at quasistatic strain rates and generally increase with increasing strain rate – but only modestly. This relative consistency in the strain rate sensitivity increase can be exploited by relatively simple constitutive relations; which will be shown in Chapter 5.

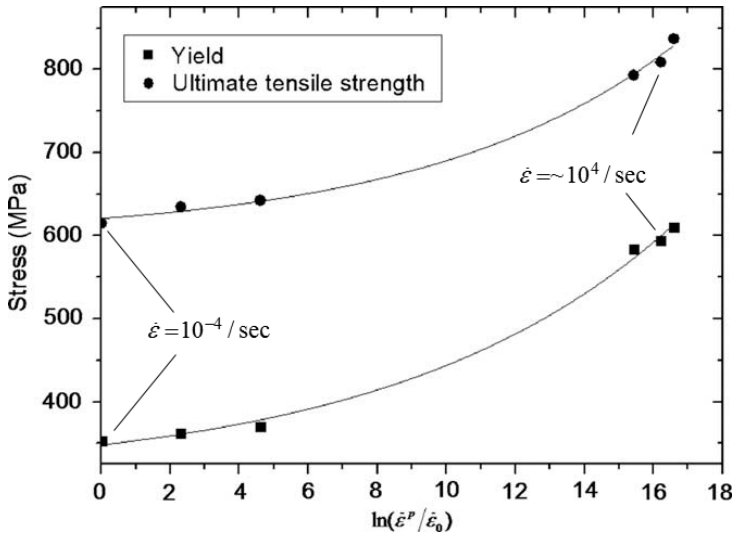

Figure 21 - Experimentally determined flow stress for DP600 across the strain rate regime of quasistatic to dynamic from Yu et al [54]. The strain rate is normalized to a quasistatic strain rate of 10^{-4}/sec.

The constitutive relations of material subject to metal forming is known to have a significant influence on the formability of the materials under PPF or almost any other forming process. There has been significant work in the past to attempt to generalize the formability predictions of sheet metal materials subject to PPF.

3.5 Generalized Formability Models during PPF

The adoption of the manufacturing process into the automotive industry generally requires that the process be predictable and stable. One of the major barriers to implementing PPF into automotive manufacturing processes has been the inability to reliably describe and predict material formability during processing. In order to overcome this barrier, significant research has been directed at developing a generalized formability model for PPF. These past techniques have generally been focused on continuum damage models and classical instability models, such as the M-K method [55].

Imbert et al. [38] performed numerical and experimental investigations of the evolution of damage internal to the materials during electromagnetic forming. They concluded that the nucleation and growth of voids during EMF could be accurately modeled using classical damage evolution equations. In their numerical models, they employed a pressure sensitive yield function which incorporated damage to track for localization as a result of the damage, and ultimately predict the fracture of the materials. Most notably, their research was able to differentiate and describe the performance of the formability of the materials under free forming and conical die forming conditions. The pressure sensitive yield function, which included hydrostatic stress during die contact, showed how the high velocity impact of the sheet metal with the die suppressed the evolution of the damage during the forming event. Their approach appears to be the methodology most likely to be able to describe complex forming that includes dies and die impact during automotive manufacturing.

Jie [56] investigated the strain rate dependence of Aluminum Killed Drawing Quality (AKDQ) steel, and showed that the positive strain rate sensitivity of the material was theoretically responsible for the forming limit diagram positively shifting in the strain rate range of 10^{-5}/s to 10/s. Figure 22 illustrates the authors observed difference in theoretical FLD calculations utilizing both conventional rate independent and rate dependent methods. Their theoretical analysis involved deploying a power law stress-strain hardening curve and using the M-K method imperfection modeling. In their model, they treated strain rate sensitivity as a variable function of the strain in the material. The theoretical forming limit diagrams they developed showed good correlation with the results for this AKDQ steel. Their work was limited to a maximum strain rate of 10/s. Furthermore, there subject material is known to exhibit positive strain rate sensitivity, and does not show the transition from negative to positive strain rate sensitivity that is typically exhibited in 5000 series aluminum. Nevertheless, Jie et al showed that capturing the rate sensitivity in the constitutive models for material can have a significant influence on the predicted forming limit diagram for that material.

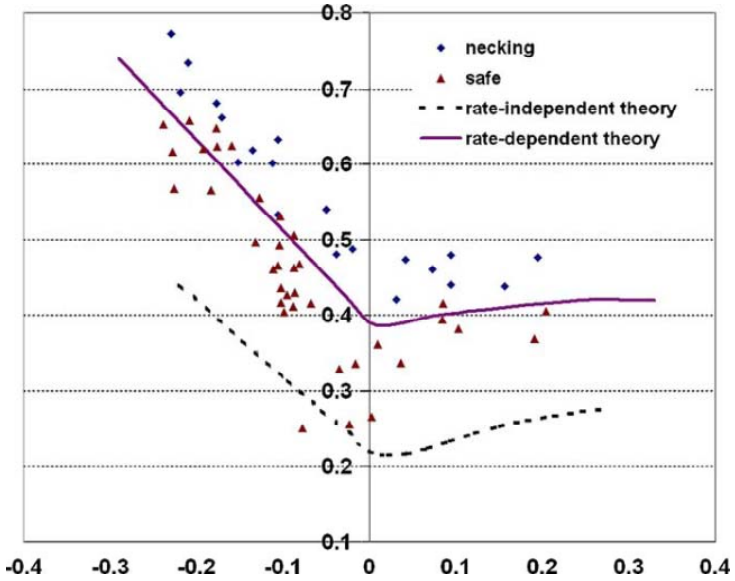

Figure 22 - Comparison of a theoretical FLD incorporating rate dependent and rate independent constitutive models from Jie et al [56].

Khan and Baig [57] also developed a predictive theoretical FLD model that employed both an anisotropic yield locus and a sophisticated constitutive model to capture the variable mechanical properties that are apparent across a wide strain rate regime of PPF. The model was based on the M-K method and employed the Khan–Huang–Liang (KHL) constitutive model [59, 60] and the anisotropic yield locus defined by Barlat's yield function (YLD96) [61]. Figure 23 shows the results of their predictions for the FLD at four strain rates: 10^{-4}/s, 10^{-2}/s, and 10^{0}/s. These results show that across this range of strain rates, little change in formability should be expected. The reason for this prediction is that the constitutive relations, and particularly the strain rate sensitivity of the materials, are relatively constant across this strain rate regime. Later analysis will show that strain rates in excess of 10^{0}/s are necessary to evoke higher formability from AA5182-O.

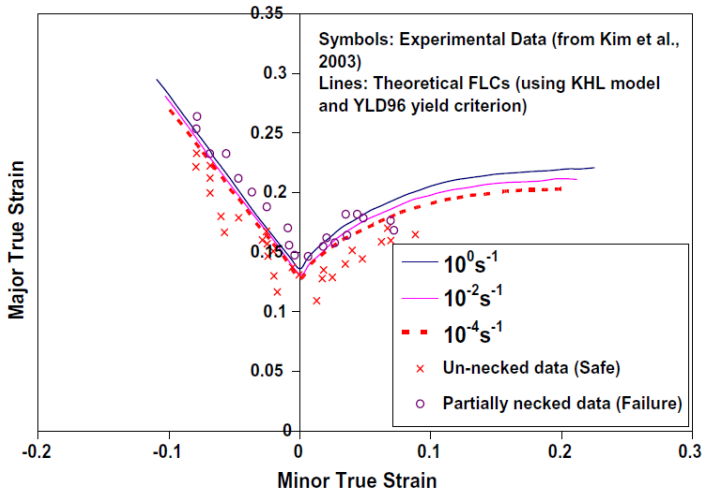

Figure 23 - Theoretical FLD for AA5182-O based on M-K theory from Khan and Baig [57]. Experimental data from Kim et al. [58].

Thomas and Triantafyllidis [62] investigated the theoretical forming limit diagrams (FLDs) of aluminum alloy sheets (AA6061) subjected to EMF. Their model incorporated the influence of the material constitutive relations at high strain rate, the influence of the current density produced in the workpiece by the EMF coil, as well as the adiabatic heating as a result of plastic work. Thomas and Triantafyllidis [62] successfully ignored the so-called inertia stabilization effects, which will be discussed later.

Figure 24 contains representative results of their models, which showed that the constitutive relations of the material at high strain rate can be responsible for significant increases in the representative FLD. Furthermore, they primarily attribute this increase in FLD to the apparent increase in the strain rate sensitivity of the materials at high strain rates. Their work showed that adiabatic heating of the materials during deformation has only minor theoretical influence on formability prediction, and that the current density produced in the workpiece as a result of the EMF process can contribute significant increases in ductility. However, Thomas and Triantafyllidis [62] had no experimental data to support the accuracy or validity of the theoretical FLD.

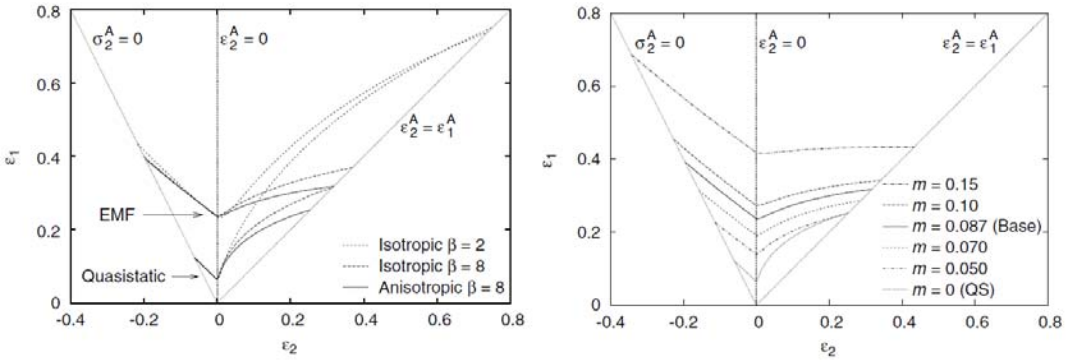

Figure 24 - Theortical FLDs from Thomas and Triantafyllidis [62]. (Left) The results showing EMF FLDs are theoretically higher for EMF compared to quasistatic. (Right) The results showing the influence of the material strain rate sensitivity on theoretical FLDs.

Hu and Daehn [63] investigated the theoretical effects of inertia stabilization on the enhanced ductility of materials in uniaxial tension. This work effectively investigates the homogeneity of plastic deformation in uniaxial tension specimens when monotonic loading is applied from one end of the specimen. The results clearly show that the velocity of loading influences the observed plastic elongation in the specimens. However, this work does not attempt to explain the enhanced formability during biaxial stretching of sheet metal. Balanethiram et al [31-33] argue that inertia stabilization is primarily responsible for the so-called hyperplasticity of materials during PPF. However, their arguments appear to be based largely on speculation as an attempt to de-convolute complex EHF process, which was the basis of their experiments. Moreover, Khan and Baig [57] and Thomas and Triantafyllidis [62] both produced predictive theoretical models of the FLD of materials subject to PPF without including the so-called inertia stabilization mechanism. Therefore, inertia stabilization may not be a primary mechanism of enhanced ductility.

In order to resolve many of the question regarding observed formability enhancements materials during PPF, a more thorough and complete experimental understanding of the process must be developed. These enhance experimental methods are the subject of Chapter 4.

4 Experimental Formability Investigation of Metals during PPF

The work under Chapter 4 aims to overcome the technical barrier that is the lack of understanding of the interrelationship between formability and measured strain rates that develop during PPF processing. There have been past works measuring sheet metal speed and general shape using videos [5], or measuring surface velocity of the materials [6]. But, this past work does not yield direct measurement of biaxial strains and strain rates during forming. This work investigates the formability and fracture of metals during PPF, and characterizes the strain rate, strain rate heterogeneity, formability, and fracture of sheet metal during PPF. This work is also designed to quantify the extended ductility of lightweight metals during PPF under proportional and variable strain rate loading using a unique experimental apparatus. The design of the system, methods of characterizing the materials and the experimental results are presented below and in recent publications of this work [7, 8, 64-66].

4.1 Experimental Apparatus

The experimental apparatus consisted of a PPF metal forming system, a set of high-speed cameras, and a digital image correlation system. A conceptual schematic of the system is shown in figure 25, where the basic components and operations have the following characteristics:

- A high energy capacitor bank delivers an electrical pulse that results in a plasma burst in the water chamber between two electrodes
- A shock wave propagates to impact the sheet metal, resulting in a pressure pulse being imparted on the work piece and the sheet is propelled away from the pressure
- Plastic strain develops during biaxial stretching, which is measured by *in-situ* camera assembly that reports real-time results using a digital image correlation (DIC) system
- Digital image correlation (DIC) system delivers continuous, real-time elastic and plastic strain, strain rate, and displacement data up to the point of fracture.
- The DIC results are post-processed to yield experimental results.

In an alternative setup, the EHF chamber can be replaced with an EMF coil and workpiece that serves to deliver the pressure pulse and impart the velocity on the sheet metal. The identical capacitor bank and high speed camera arrangements are employed regardless of the use of EHF or EMF. In this work, results for both EHF and EMF are presented, but the vast majority of the results will focus on EHF.

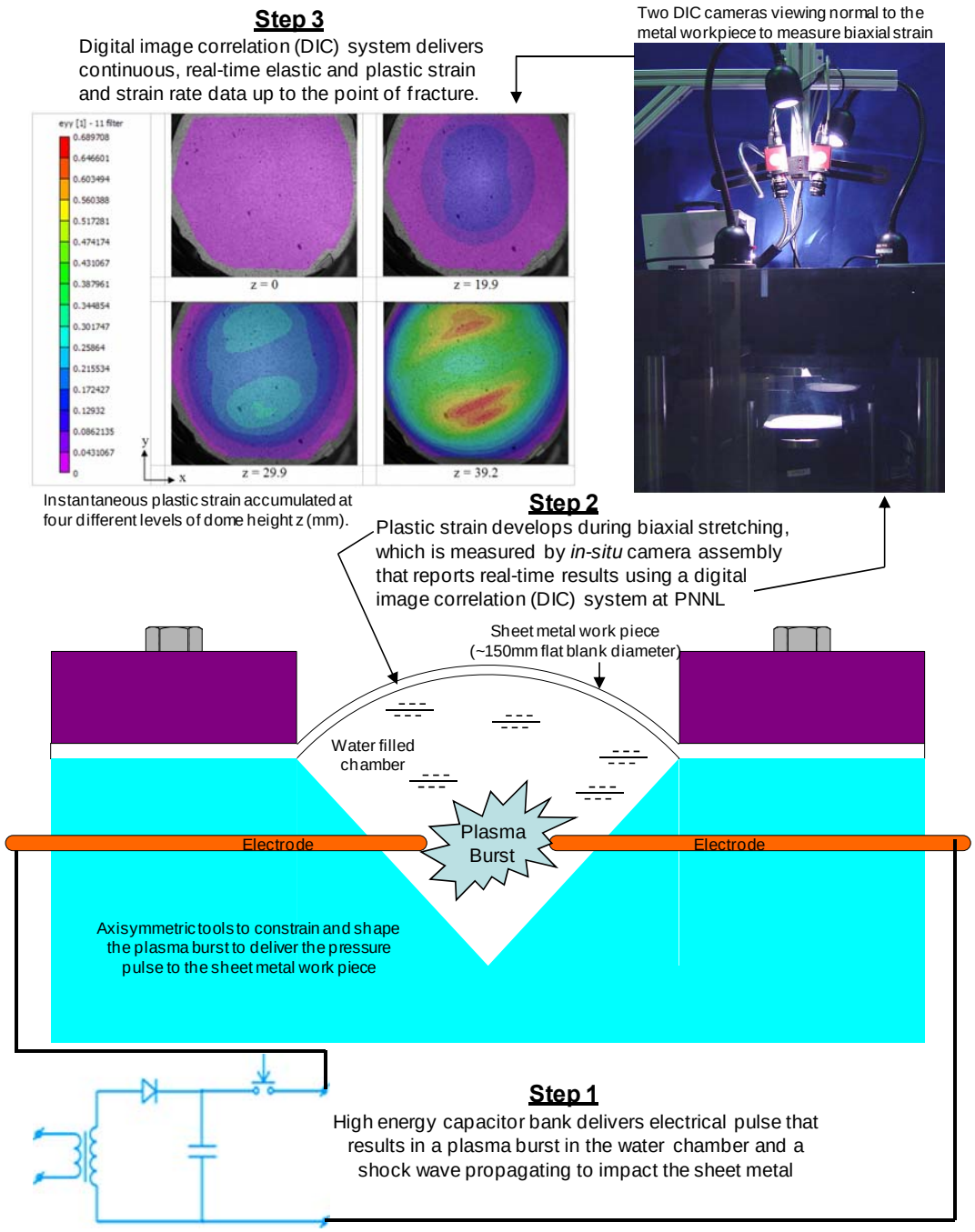

Figure 25 – Conceptual illustration of the test apparatus showing the capacitor bank, EHF chamber, in-situ cameras, and the real-time strain measurements.

The most important element of this work is the quantification of the *in-process* deformation parameters (displacement, velocity, strain and strain-rate) that have typically been unknown, or estimated at the best, in the literature. The quantification method, as well as the equipment and the test procedures employed in this research are described below, and are detailed and described in a publications [7, 8, and 64].

The approach to quantifying sheet deformation behavior is comprised of painting a speckle pattern on the undeformed metal sheet. The sheet was then deformed via PPF and the deformation process was imaged by a pair of high-speed cameras. The images of the deforming sheet were captured and post-processed by the digital image correlation (DIC) software to calculate the displacement, velocity, strain and strain-rate, as a function of time, at any given point on the sheet.

Digital image correlation is an optical method to measure deformation on an object surface. This method uses white-light speckle correlation to measure deformation in each image of an image sequence where any two consecutive speckled images, captured by a video camera, represent the incremental stages during the deformation process. In this work, digital image correlation software (Vic-3D, Version 2009.1.0) from Correlated Solutions, Inc., in conjunction with the image sequence captured by the high-speed cameras, was used to quantify the in-process sheet displacement, velocity, strain and strain-rate, as a function of time. A software calibration was performed at the start of the experiments by imaging a pre-measured geometrical test-pattern using the cameras. This calibration essentially defines the cameras' orientation in space, relative to each other. Following calibration, the cameras position was held fixed such that the sheet deformation was imaged without disturbing the camera's relative orientation to each other. Therefore, when the software analyzes the sequential images of the sheet captured during the EHF or EMF test, the software is able to quantify the displacement of the speckles in the image sequence and the strain tensor can be determined at any point on the sheet surface. Once the in-process displacement and image capture rate is known, the velocity, strain, and strain-rate at each point on the sheet can be plotted as a function of time. A quick check of the software's analysis was performed by comparing the final dome heights determined by the DIC software with those measured physically on the deformed sheet (as a global validation of accuracy).

A schematic of the EHF forming chamber is shown in Figure 26, and a close-up photograph of the EHF forming chamber is shown in Figure 27. The EHF fixture was machined out of steel and consisted of a hemi-spherical cavity (~152 mm diameter) with two opposing electrodes inserted through the chamber walls. The electrodes were copper rods, 6.35 mm in diameter with a gap of ~11.5 mm between the two ends. A thin copper wire can be used to join the electrode ends, thus, creating an electrical "short" between the electrodes. The system can also operate without the copper wire, though the efficiency of the system is reduced. External to the chamber, the copper electrodes were connected to a capacitor bank with ~2.44 m (8 ft.) long cables, and a program written in LabView software was used to control the charge-discharge process. For a given capacitor bank charge voltage V, the electrical energy input was calculated as $\frac{1}{2}CV^2$ where C is the capacitance (750 uF) of the bank. The voltage at the positive electrode at the EHF chamber was measured using a single-ended high voltage probe (Tektronix P6015A with ~7.62 m (25 ft.) cable and a 1000X attenuator) and Tektronix oscilloscope model TDS3034B. The

discharge currents were measured by Rogowski coils and recorded by the data acquisition system. The chamber was filled with water prior to each test.

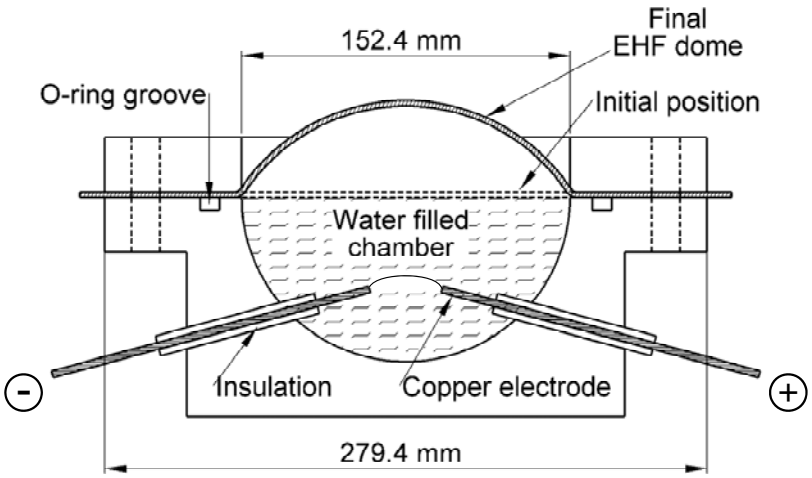

Figure 26 - Illustration of the EHF forming chamber showing the initial undeformed and the final deformed positions of the sheet.

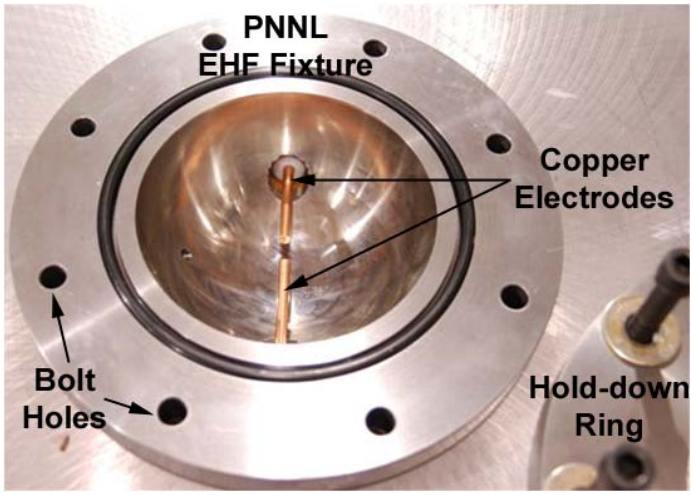

Figure 27 - Photograph of the internal forming chamber of the EHF apparatus.

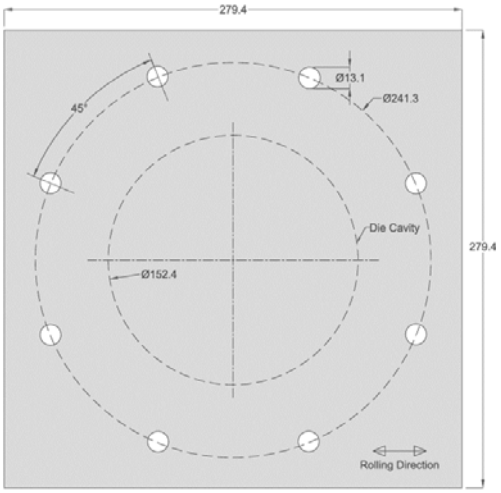

Figure 28 - A drawing of the sheet metal specimen subject of EHF.

The typical specimen geometry is shown in Figure 28. One face of the sheet specimen was speckle-patterned by spray-painting it with white automotive paint and then creating a random pattern of spots with a black-color marker, as shown in Figure 29. The sheet was bolted to the EHF chamber (Figure 26) through a hold-down ring with the speckled face facing the cameras and illuminated by several high-intensity lights as shown in Figure 30. This testing configuration is referred to as "free-forming" in that the sheet is constrained circumferentially by a ring and a central region (~152 mm diameter) of the sheet is free to deform when subjected to the pulse-pressure wave originating from the underlying hemispherical EHF chamber. Consequently, the final deformed shape of the sheet was in the form of a dome, as shown in Figure 31. The center of the 152 mm circular portion of the undeformed sheet was marked and is referred to as the "apex" in subsequent discussion.

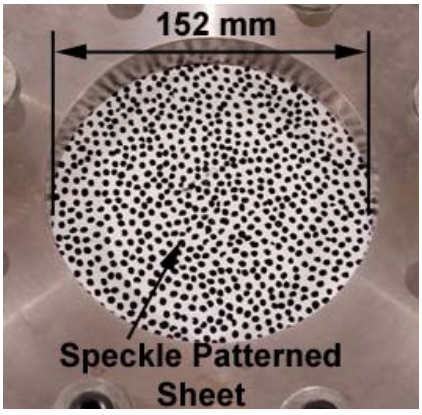

Figure 29 - A photograph of the undeformed specimen showing the speckle patterned sheet clamped in the EHF apparatus.

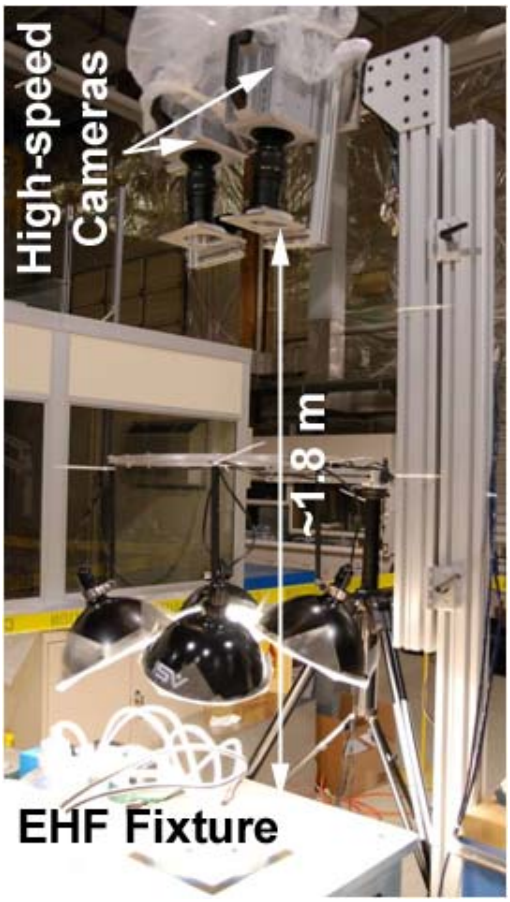

Figure 30 - A photograph of the general arrangement of the experimental setup showing the relative location of the cameras with respect to the forming system.

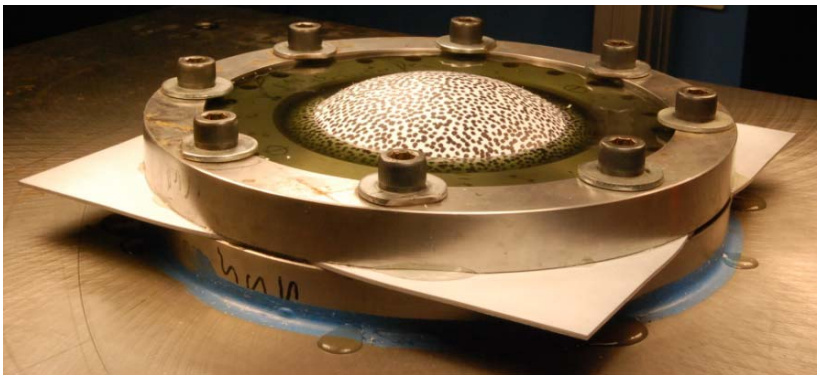

Figure 31 - A photograph of an EHF-deformed sheet. Some water has leaked out from the hemi-spherical chamber owing to fracture (not visible) in the sheet.

The experimental setup used two Photron SA1 high-speed cameras to capture the sheet deformation at a frame rate of 45,000 to 67,500 per second and at an image resolution of 256 x 256 pixels or higher. The cameras were simultaneously triggered to capture the images when the capacitor bank was discharged to initiate the EHF or the EMF process. At the end of the test, the image sequence corresponding to the sheet deformation was saved on the computer for subsequent image analysis.

In order to conduct an experiment, the EHF chamber was filled with tap-water and the speckle-patterned sheet clamped over it ensuring that there was no air gap between the water and the sheet bottom. The capacitor bank was charged to the desired voltage (energy) and discharged immediately upon reaching the set voltage level. The capacitor discharge results in large currents (10s of kA) to flow through the copper wire or the water filled space located between the electrodes that result in rapid melting of the wire, and vaporization and expansion that generates the pressure-pulse.

4.2 Experimental Results of Free Forming

The initial testing of the experimental apparatus was conducted using both EMF and EHF as the systems that generated the pressure pulses. The system used identical methodologies as those described above, except an EMF coil was also used and compared to the results using the EHF chamber. The EMF coil assembly used a conventional coil [1], and the diameter of the free forming dome was 76mm. Figure 8 contains a photograph of the coil, specimen, and tooling used in these EMF experiments for reference. This early and initial validation of the methodology showed that the high speed cameras and DIC system successfully gathered data as expected. Five successful tests were conducted to demonstrate the system performance, and the specimen names, materials, and capacitor bank charge voltages are shown below.

- EMF1 – AA5182-O, 2mm thick, 6.5kV charge (750uF)
- EMF2 – AA5182-O, 2mm thick, 6.5kV charge (750uF)
- EMF3 – AA5182-O, 2mm thick, 7.2kV charge (750uF)
- EHF1 – AA5182-O, 2mm thick, 5.5kV charge (750uF)
- EHF2 – AA5182-O, 2mm thick, 6.2kV charge (750uF)

Figure 32 shows the results of five tests – three EMF and two EHF. The EMF specimens had a 76 mm diameter working area, where the EHF had 152mm diameter working area. The dome height achieved in the EMF specimens was 8-10mm, where the dome height of the EHF specimen was 16-22mm at the apex of the dome. Figure 33 shows the velocities that were achieved while forming the domes at the apex of the dome. The figure shows that the velocities of the EMF dome were 80-105 m/s, where the EHF domes were 42-50 m/s. Figure 34 shows the Lagrangian strain rate of the materials in one direction of the x-y plane of the material at the apex of the dome. The figure shows that all five specimens achieved similar levels of plastic strain, though the velocities, strain rates, and dome heights were all significantly different (due mainly to the specimen geometry difference). This initial round of testing showed that the high-speed cameras and the DIC system were capable of measuring and differentiating the forming events. This was a promising initial conclusion from the apparatus, and the

decision was made to employ the EHF apparatus to further investigate the formability and failure of sheet metal during high rate forming.

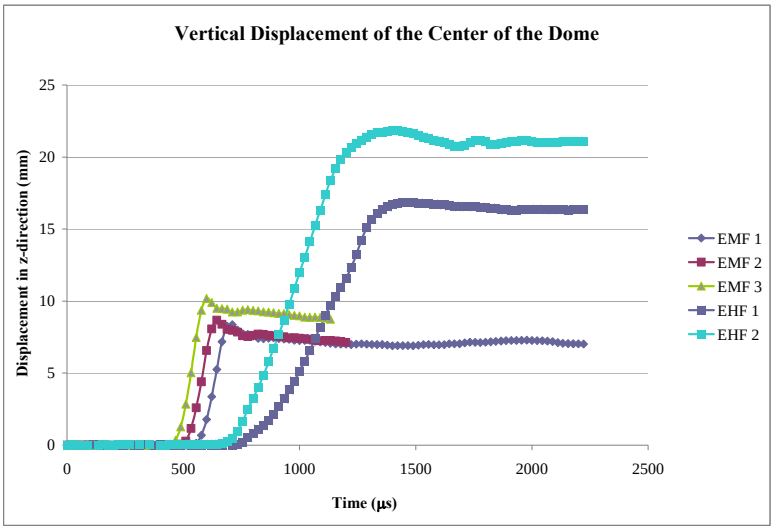

Figure 32 - The displacement versus time for three EMF specimens and two EHF specimens at the apex of the forming dome.

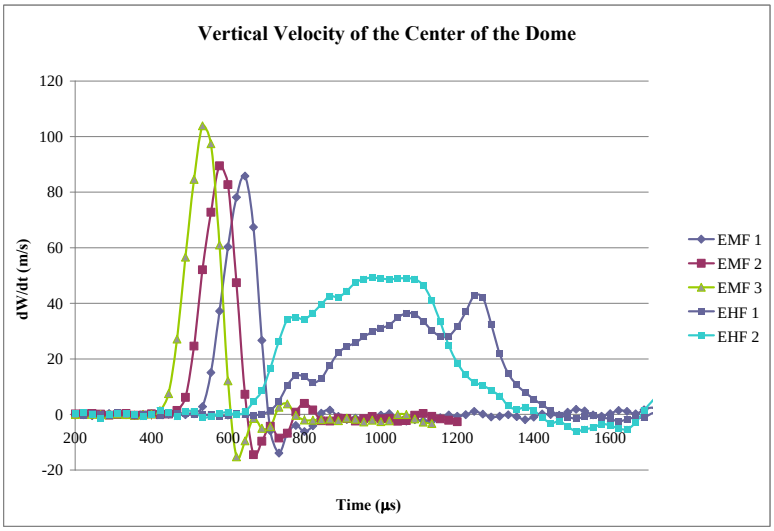

Figure 33 - The velocity versus time for three EMF specimens and two EHF specimens at the apex of the forming dome.

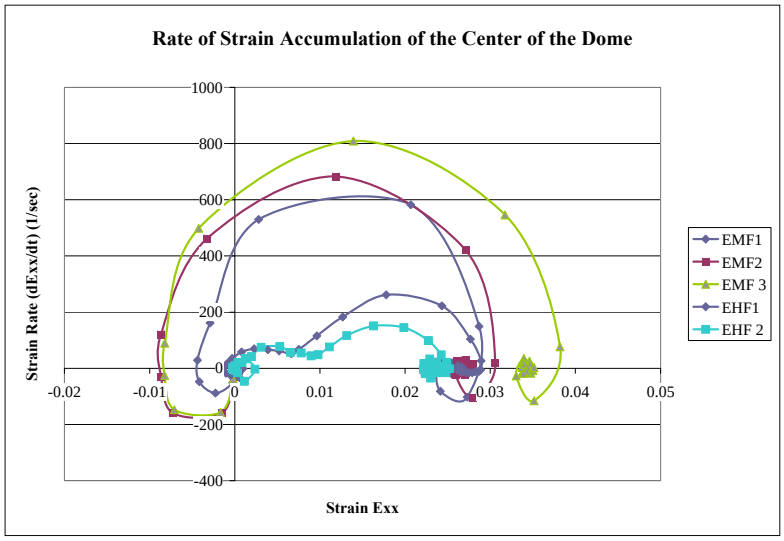

Figure 34 - The Lagrangian strain rate in one direction on the x-y plane of the work piece at the apex of the forming dome.

The EHF experiments initially and primarily focused on 1 mm thick 5182-O aluminum. Tests were conducted at voltages of 5000, 6500 and 7500 V corresponding to an energy (stored in the capacitor banks) of ~9.4, 15.8 and 21.1 kJ. The entire deformation event for each test was captured by the high-speed cameras and the images were stored for subsequent analysis. Table 1 lists the experimental details for various tests, with the noted test name (specimen name) for later discussion. Table 1 also compares the physically measured dome height (measured relative to the top surface of the undeformed portion of the test sheet) and thickness strain at the apex relative to those calculated by the image analysis DIC software.

Table 1 - Summary of EHF test results of 1 mm thick 5182-O Al sheet deformed under free- forming conditions.

Test Name	Voltage (V)	Energy (kJ)	Dome Height Measurements (mm)		[a]Thickness Strain at Apex (Engineering)		Max. Velocity (m/s)			Max. Strain Rate (Lagrangian strain) (1/s)		
			Calipers	*DIC*	*Calipers*	*DIC*	*Loc. 1*	*Loc. 2*	*Loc. 3*	*Loc. 1*	*Loc. 2*	*Loc. 3*
T-26	5000	9.4	37.9	37.1	0.13	0.13	65	62	58	207	166	196
T-24	6500	15.8	40.7	40.0	0.19	0.19	70	70	64	237	283	435
T-28	7500	21.1	47.5	49.0	0.22	0.23	94	83	100	271	383	664

[a]Thickness strain at the apex, measured by the DIC technique, was converted from Lagrangian into engineering strain.

The data generated by the DIC system requires some explanation of the coordinate systems employed and the quantification of strains. The displacements and velocity of any point on the sheet were calculated by the DIC software in the *global* coordinate system i.e. the x and y axes correspond to the horizontal and vertical direction in the 2-dimensional camera images, while z-axis is normal to the plane of the image and corresponds to the normal to undeformed sheet. The strain and strain-rate at any point on the surface of the sheet are presented in *local* coordinate system, which is constructed (by the software) as follows:

- A tangent plane is drawn at the point of interest on the sheet.
- The local z-axis is normal to the tangent plane.
- The local x-axis is the projection of the global x-axis in the tangent plane.
- The local y-axes is perpendicular to the x-axis and also lies in the tangent plane
- The DIC software calculates the strain in Lagrangian formulation, which is presented in this paper unless indicated otherwise.

The DIC system delivers results in Lagrangian strain, but the more conventional metal forming strain measures are engineering strain and true strain. The Lagrangian strain is related to engineering strain by the following relation:

$$\varepsilon_{xx}^{Lagrangian} = e_{xx} + \frac{1}{2}e_{xx}^2$$

Solving this equation for engineering strain yields:

$$e = \sqrt{1 + 2\varepsilon^{Lagrangian}} - 1$$

And the engineering strain is converted to true strain using:

$$\varepsilon = \ln(e + 1)$$

Solving for true strain in terms of Lagrangian strain yields:

$$\varepsilon = \frac{1}{2}\ln\left(2\varepsilon^{Lagrangian} + 1\right)$$

The default presentation of strain data throughout the experimental work is Lagrangian strain. However, further characterization of the results and subsequent formability discussions are based in more conventional engineering and true strain throughout the paper.

Figure 35 shows photographs of specimens formed into domes via EHF, which were free-formed at 5000, 6500 and 7500 V capacitor bank charge voltages. The dome formed at 6500 V is shown with the speckle pattern cleaned-off around the apex as well as sectioned across the middle (to machine out a specimen from the apex for microstructural examination). Figure 36 shows the software reconstruction of dome profiles, corresponding to the end of the test and at the indicated time (from the beginning of

deformation). The DIC technique allows the deformation history to be obtained for any point on the dome. As an example, the deformation parameters were determined at specific locations identified as locations 1-3. Location 1 refers to the dome apex while locations 2 and 3 lie at a distance of ~22.5 mm and ~45 mm from the apex along the x-axis. Table 1 summarizes deformation parameters for various tests and the data from test done at 7500 V is analyzed in the subsequent sections as an example. It is noted that in Figures 37-39, the electrodes are positioned along the x-axis in the images and each data point in the associated graph represents a camera frame captured during the EHF test.

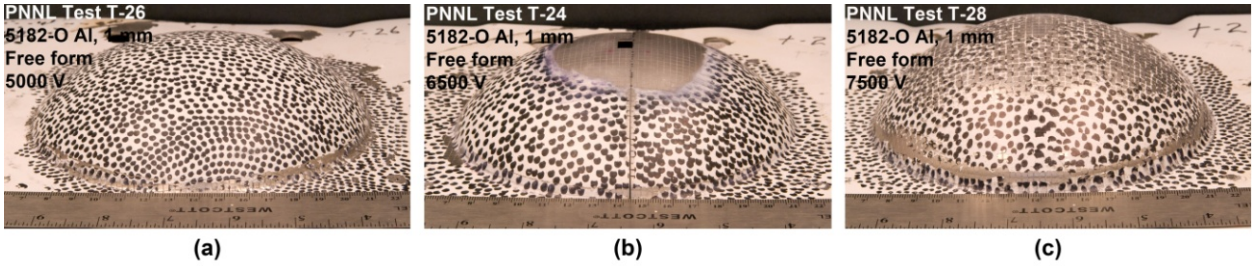

Figure 35 - Post-test photographs of the domes that were EHF free-formed at (a) 5000 V, (b) 6500 V and (c) 7500 V.

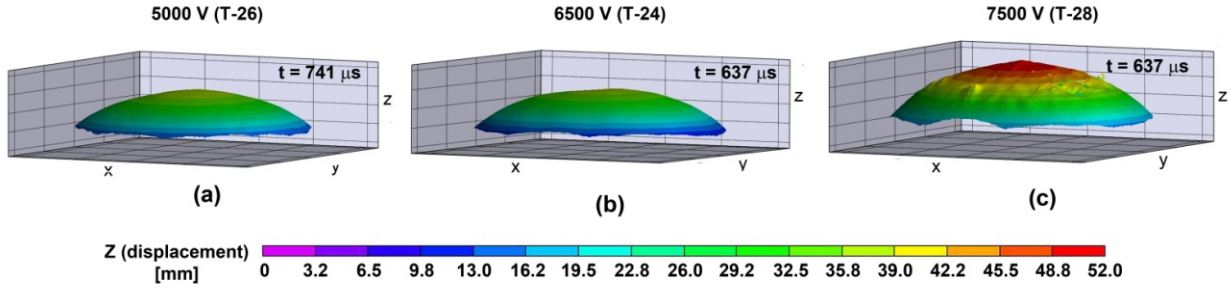

Figure 36 - Dome profiles reconstructed by the DIC software for the test at (a) 5000 V, (b) 6500 V and (c) 7500 V.

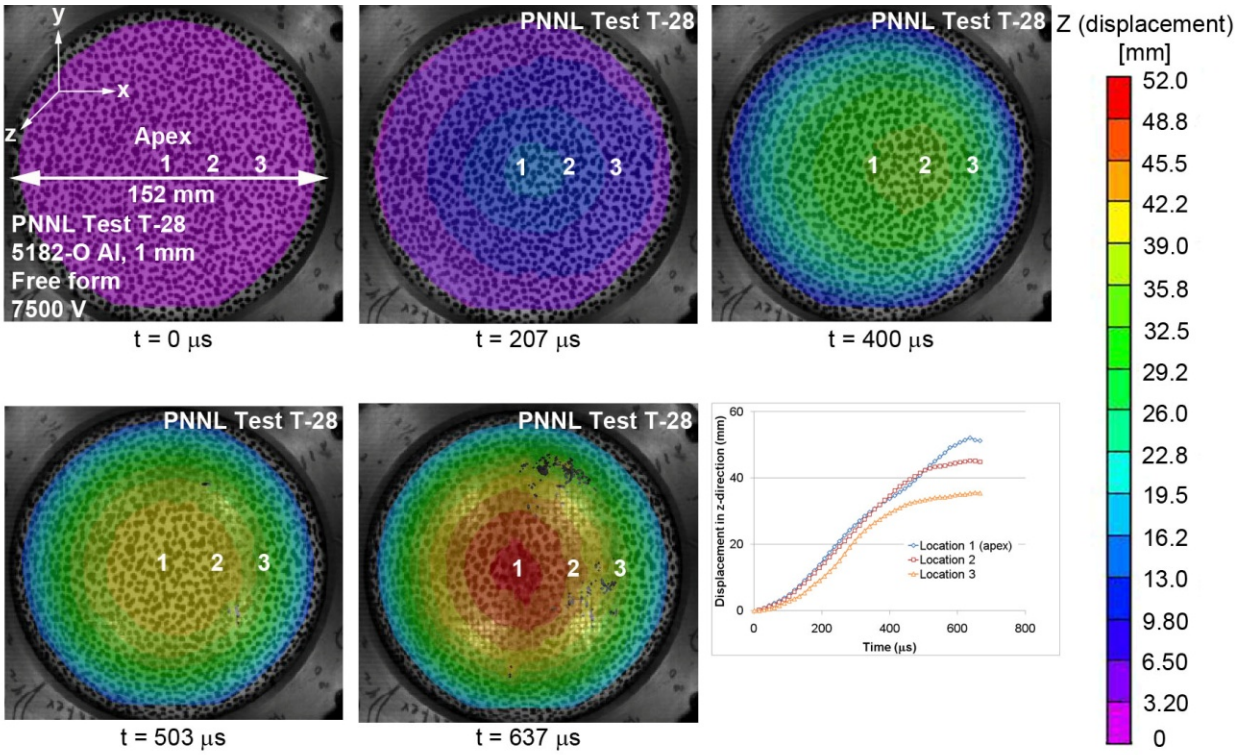

Figure 37 - Dome height evolution (z-displacement in the global coordinate system) contours of EHF formed sheet (7500V) at selected instances during the test with the graph showing the entire displacement-time history for three locations (identified as 1, 2 and 3) on the sheet.

Figure 37 shows the out-of-plane displacement contours at selected times during the sheet deformation under free forming conditions and at a charging voltage of 7500 V. The contours are generally symmetrical in nature. The graph in figure 37 shows the z-displacement-time history for three locations on the sheet. The data shows that the vertical displacement of the sheet at the end of the test (~600-650 μs from start), as calculated by the DIC software, was ~50 mm at the dome apex. Similar contours and plots can be obtained for displacements in the x and y directions as well as for tests done at any charging voltage.

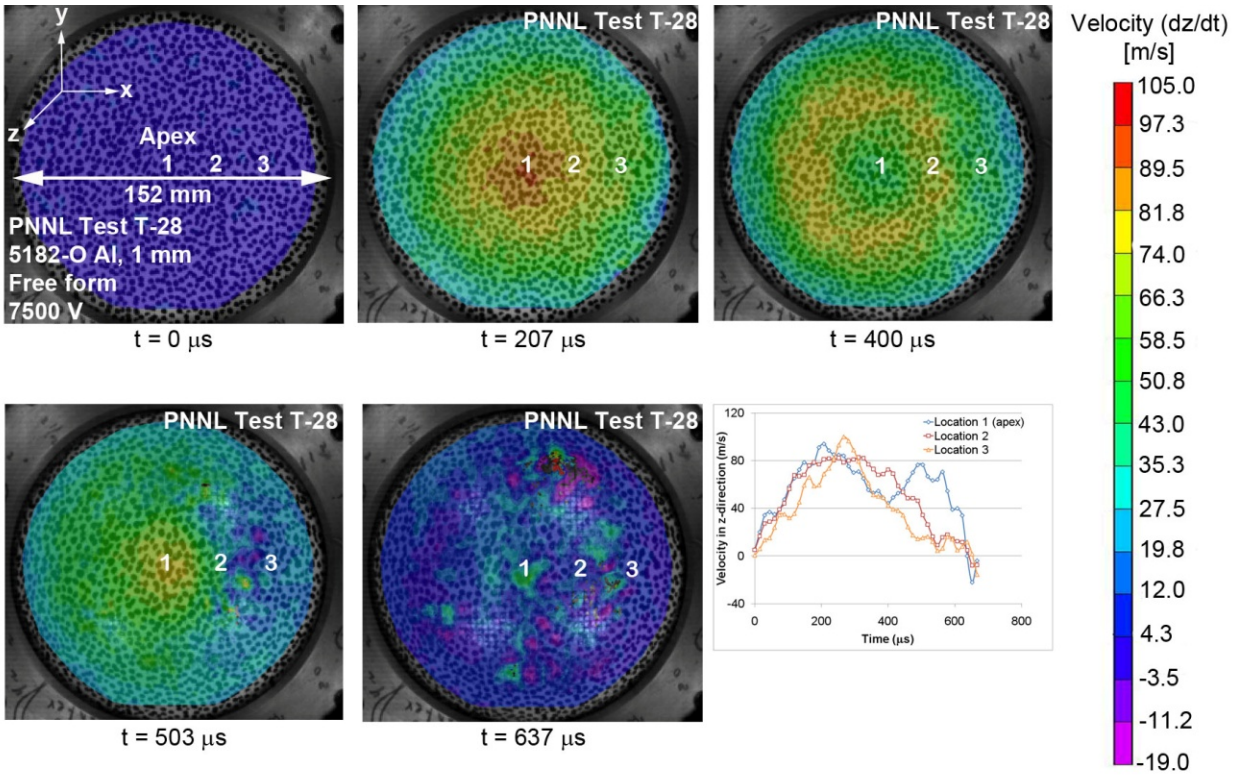

Figure 38 - Velocity contours (z-direction in global coordinate system) of EHF formed sheet (7500 V) at selected instances during the test with the graph showing the entire velocity-time history for three locations (identified as 1, 2, 3) on the sheet.

The sheet velocity is one of the more critical attributes of the PPF process, and the variable that has significant variation and speculation in the technical literature. Figure 38 shows the velocity of the sheet during dome formation (out-of-plane velocity contours) at selected times corresponding to the displacement data (7500 V) shown in figure 37. The velocity contours are generally symmetrical in nature up to ~400 μs following which (e.g. at *t* = 503 μs) the right half of the sheet undergoes deceleration that is not observed in the remainder of the sheet. The graph in figure 38 shows the entire velocity-time history for three locations on the sheet. At these locations, the velocity rises to a maximum by 200-300 μs from the start, followed by a decrease. The velocity-time profile at the apex (location 1) shows a double-peak behavior with velocity peaks of ~94 m/s at ~207 μs and of ~76 m/s at ~503 μs. On the other hand, location 2 has a broad maximum of 80-90 m/s between 200-300 μs and location 3 has a single velocity peak of ~100 m/s at ~267 μs. Similar contours and plots can be obtained for velocity components in the x and y directions as well as for tests done at any charging voltage. The data also shows some velocity oscillations superimposed on the overall velocity-time curve of any given location. These velocity oscillations are likely due to the pressure-wave reverberations within the EHF chamber. The graph in figure 38 shows that the system captures the elastic rebound of the dome after the forming event, where a small negative velocity is seen in the dome prior to reach zero final velocity.

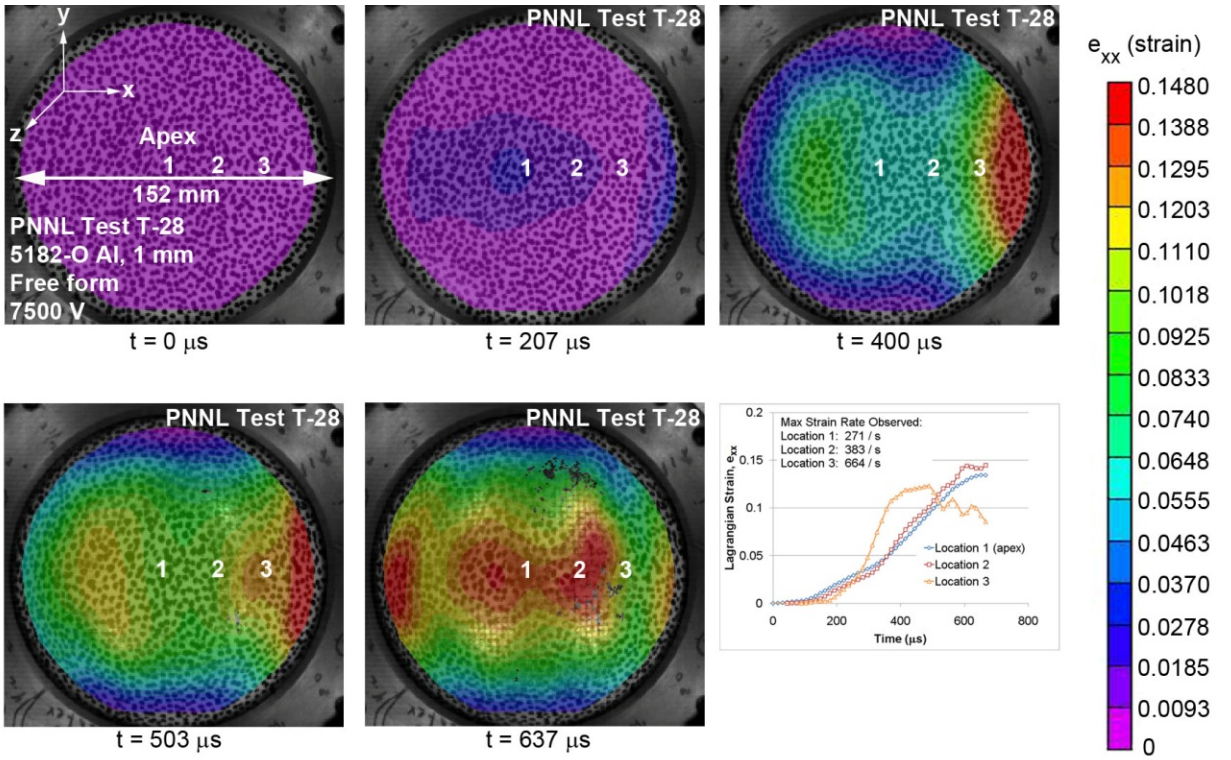

Figure 39 - Lagrangian strain contours in the x-direction (local coordinate system) of EHF formed sheet (7500 V) at selected instances during the test with the graph showing the entire strain-time history for three locations (identified as 1, 2, 3) on the sheet.

The plastic strain accumulated in the sheet is of primary interest from a metal forming perspective. Figure 39 shows the strain (Lagrangian strain in the x-direction) contours at selected times corresponding to the displacement data (7500 V) shown in figure 37. Figure 40 compares the time evolution of e_{xx} and e_{yy} strains. Unlike the symmetrical nature of displacement and velocity contours in figure 37 and 38, respectively, the e_{xx} strain contours in figure 39 are not symmetrical, and generally show strain concentrations that moves from the right side of the sheet to the apex and to the left of the sheet in the figure. The strain-time graph shows that locations 1 and 2 have a similar strain-time history for the duration of the test, but that location 3 deviates from the trend at ~267 μs and accumulates strain at a higher rate than locations 1 or 2. The maximum strain was accumulated at location 2 and was ~0.15, while location 3 accumulated a total strain of ~0.09. The rate of strain accumulation is indicated by the maximum strain rate, over the entire test duration, observed at each of the three locations in this test.

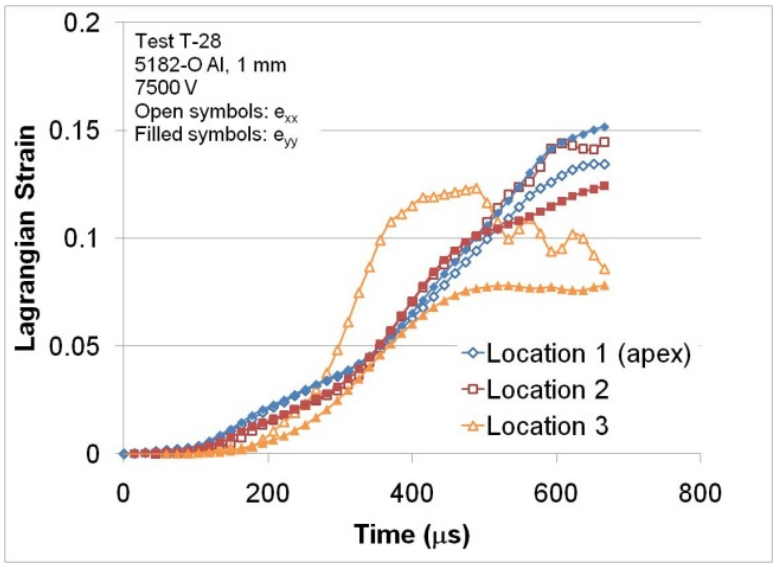

Figure 40 - Time evolution of Lagrangian strains at three reference locations on the EHF formed Al sheet (7500V).

The most critical unanswered question from the technical literature is regarding the strain rate of the sheet materials during the forming event. Figure 41 plots the strain-rate (de_{xx}/dt) as a function of strain (e_{xx}) at three locations in the sheet at three different capacitor bank charge voltages. The data shows that the maximum strain-rates achieved were ~207, ~435 and ~664/s at 5000, 6500 and 7500 V charging voltage, respectively. At any given charging voltage, the maximum was observed at location 3 (except at 5000 V) while location 1 (apex) showed lower strain-rate. The strain-rate vs. strain data in figure 41 is characterized by "jumps" in the strain-rate. For example, at 7500V and location 3, the strain rate rapidly increases to ~213 /s and after a brief interval, rapidly increases to ~664 /s followed by a decrease to ~524 /s and a final decrease at a faster rate. The data in figure 41 also shows the strain-rate swings to negative values towards the end of deformation. The minimum strain-rate (i.e. most negative value), though somewhat lower in absolute magnitude, was of similar order of magnitude (~423 /s) as the maximum positive strain-rate (~664 /s). A critical note on the existence of negative strain is that the system does not differentiate elastic and plastic strains, and total strain and strain rates are reported.

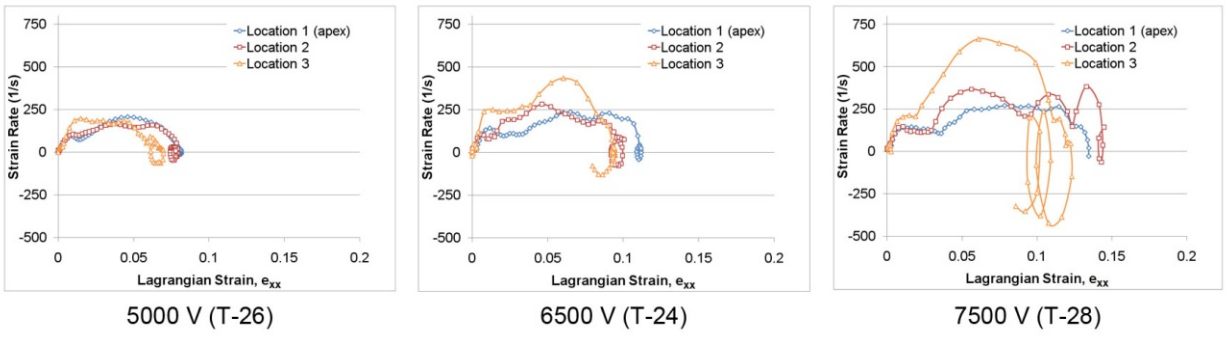

Figure 41 - Strain vs. strain-rate data (local coordinate system) at the three locations on a sheet deformed at the charging voltages shown.

The differences in strain and strain rate for each of the three specimens are of the most critical interests. Using the strain data from the DIC technique, the equivalent plastic strain at the apex was calculated to be ~0.143, ~0.213 and ~0.268 for tests at 5000, 6500 and 7500 V, respectively. Using stress-strain data for AA5182 aluminum developed by Smerd et al. [52], the strain energy density (area under the stress-strain curve) for above mentioned equivalent plastic strains is ~36, 61 and 82 MJ/m^3, respectively. Relative to the test at 5000 V, the strain energy density increases by ~69% and ~128% for 6500 and 7500 V tests. Increasing the test voltage from 5000 V to 6500 and 7500 V increases the electrical energy ($\frac{1}{2}CV^2$) by 69% and 125%, respectively. Thus, it is interesting to note that the increase in plastic strain at the apex (described by the plastic strain energy at equivalent plastic strain) is almost proportional to the % increase in electrical energy. In other words, the proportion of input electrical energy converted to plastic deformation of the sheet appears to remain constant within the range of energy employed in this work.

Plotting the strain-rate vs. strain to describe the sheet deformation, as shown in figure 41, provides valuable information on the strain-rates associated with plastic deformation at any given location on the deforming sheet. Such strain-rate information is especially critical in modeling the deformation behavior of strain-rate sensitive materials. Further, such quantitative strain-rate data is also critical in addressing the possible causes of extended ductility during sheet metal forming that has typically been attributed to (among other factors) “high” strain-rates by prior researchers [3, 31-34, and 37], despite the lack of actual strain-rate information. Furthermore, figure 41 demonstrates that ascribing one particular strain-rate to the entire sheet and for the entire forming event, as it has been generally done in the existing literature, may not be correct. Instead, different locations in the sheet may undergo plastic deformation at vastly different strain rates, especially at higher voltages. For example, figure 41 shows that while locations 1-3 experienced a majority of deformation at a similar maximum strain rate of ~200 /s at 5000 V, increasing the discharge voltage to 7500 V moved the location of overall maximum strain rate to location 3 where the strain-rate magnitude (~664 /s) was ~2.5 times that observed at location 1 (~271 /s). Figure 41 also shows that plastic deformation at locations 2 and 3 (6500 and 7500 V) was associated with non-monotonic variations in strain-rate during the entire test. Therefore, figure 41 shows the wealth of information that can be obtained from the DIC data measurement/analysis technique. The detailed spatial and time dependence of strain-rate is necessary for accurate modeling of sheet deformation during the EHF process, as well as an important understanding for the mechanisms underlying enhanced formability in sheet metals during high-rate forming processes.

4.3 Experimental Results of Conical Die Forming

The results of free forming described above allow an unprecedented understanding of the deformation history of the materials during PPF. However, the real application of PPF for automotive manufacturing will require the interaction of the sheet metal with a die. This work will focus on characterizing the differences in the forming between free forming and forming involving die contact. This testing will focus exclusively on using electrohydraulic forming (EHF) as the experimental apparatus that generates the pressure pulse. The EHF system was configured in two ways. First, the forming was conducted under free forming conditions as described above, where no dies were introduced to restrict the shape

or velocity of the material. Second, the forming was conducted under conical die forming conditions, where a conical dies was introduced to restrict the shape and velocity of the material. Figure 42 shows the addition of a conical die to the free forming apparatus described above. The conical die subtends an angle of 84° at the apex and is truncated below the apex to yield a ~38 mm opening to allow cameras to view the sheet. In the results presented subsequently, the x-direction in the plane of the test sheet is along the electrodes while the z-direction corresponds to the out-of-plane normal to the test sheet. The sheet metals used in this work are 1 mm thick AA5182-O and DP600 steel.

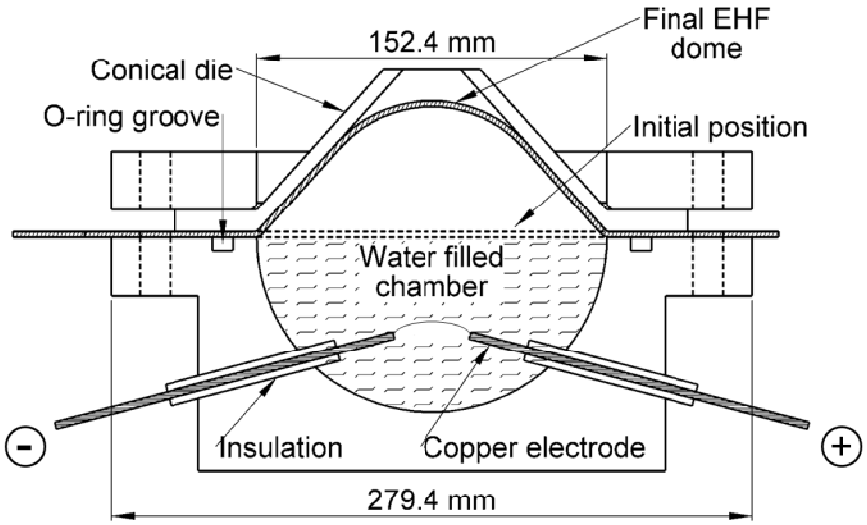

Figure 42 - Illustration of the EHF forming chamber showing the initial undeformed and the final deformed positions of the sheet. This system has a conical die introduced to restrict the expansion of the sheet metal.

Under free-forming test configuration described above, the entire 152.4 mm deforming area of the sheet was visible to the high speed cameras. However, introducing the conical die caused the effective viewing area to be limited to ~25 mm central portion of the sheet. Figure 43 shows the conical die clamped on the EHF chamber and the inset shows the interior of the die. Figure 44 shows a picture of the cameras' view through the conical die and looking at the speckle-patterned sheet. The DIC software analyzes the speckle pattern in the image sequence from the EHF test and determines the displacement and strain tensor at a given location on the viewable area of the sheet. Knowing the in-process displacement and image capture rate, the velocity, strain, and strain-rate can be plotted as a function of time. Again, a validation of the software's analysis was performed by comparing the final dome heights determined by the DIC software with those measured physically on the deformed sheet.

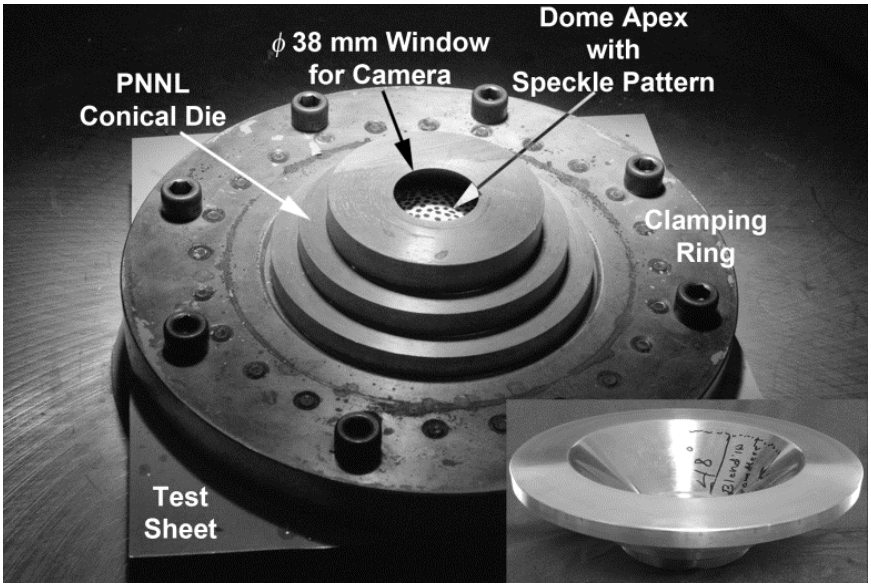

Figure 43 - Photograph of EHF apparatus with the conical die inserted. The inset shows the die inverted.

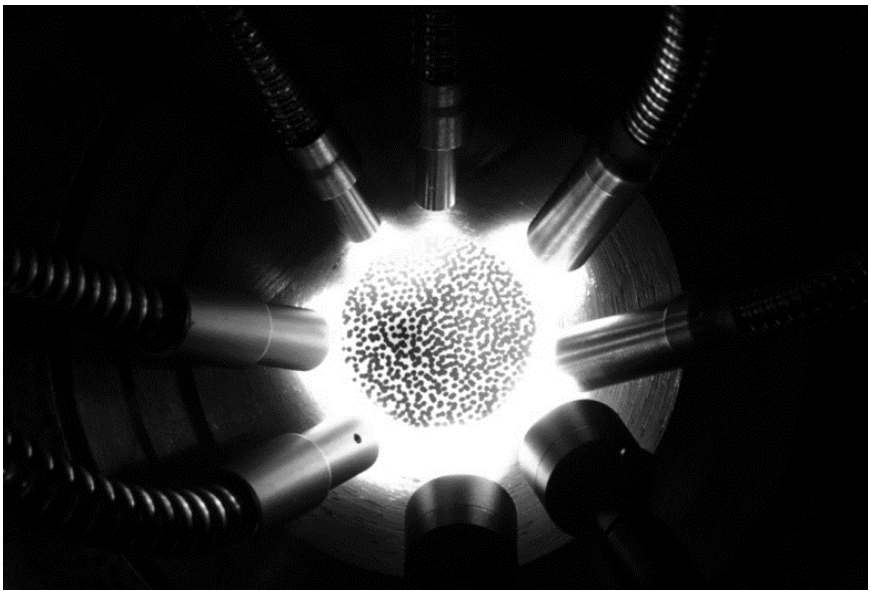

Figure 44 – High speed camera point-of-view looking down into the conical die on the speckle-patterned sheet that is illuminated using multiple light sources.

Table 2 summarizes deformation parameters and dome heights achieved for various tests. The data in Table 2 shows that with the exception of test DP6-4, there is a good correspondence between the physically measured dome height and that determined by the DIC software. Further, for a given charging voltage, the conical-die formed Al domes were ~10% higher than their free-formed counterparts while the heights were similar in the case of steel domes. Figures 45-47 show the post-test

photographs of the EHF domes. Under the conditions employed in this work, none of the domes were strained to failure. The images also show that the free-formed domes posses a "rounder" profile relative to the conical-die formed domes, since the die restricted expansion of the sheet.

Table 2 - Summary of EHF tests comparing free forming and die contact

Material	Die	Test Name	Voltage (V)	Energy (kJ)	Dome Height (mm)		Camera frames per second
					Calipers	*DIC*	
5182-O Al (1 mm)	Free-forming	T-26	5000	9.4	37.9	37.1	67,500
		T-24	6500	15.8	40.7	40.0	
		T-28	7500	21.1	47.5	49	
	Conical die	T-30	6500	15.8	44.9	44.1	45,000
		T-34	7500	21.1	51	46.1*	
DP600 Steel (1 mm)	Free-forming	DP6-4	9500	33.8	33.8	37.1	67,500
	Conical die	DP6-6	9500		34.2	33.6	45,000

*Height from the last analyzable image frame; subsequent images of still deforming sheet could not be analyzed because of the delamination of paint/speckle pattern.

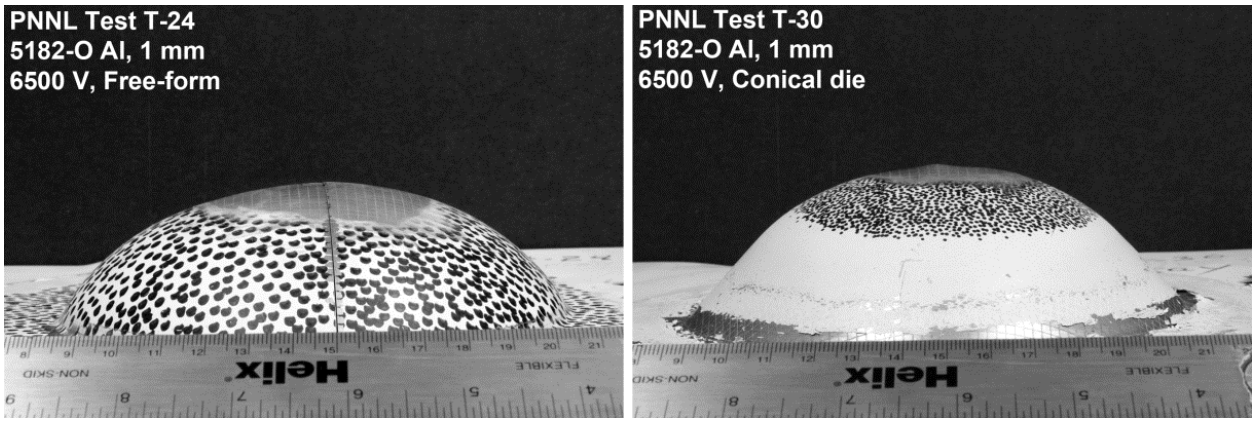

Figure 45 – Images comparing free forming and conical die forming for AA5182-O at 6500V.

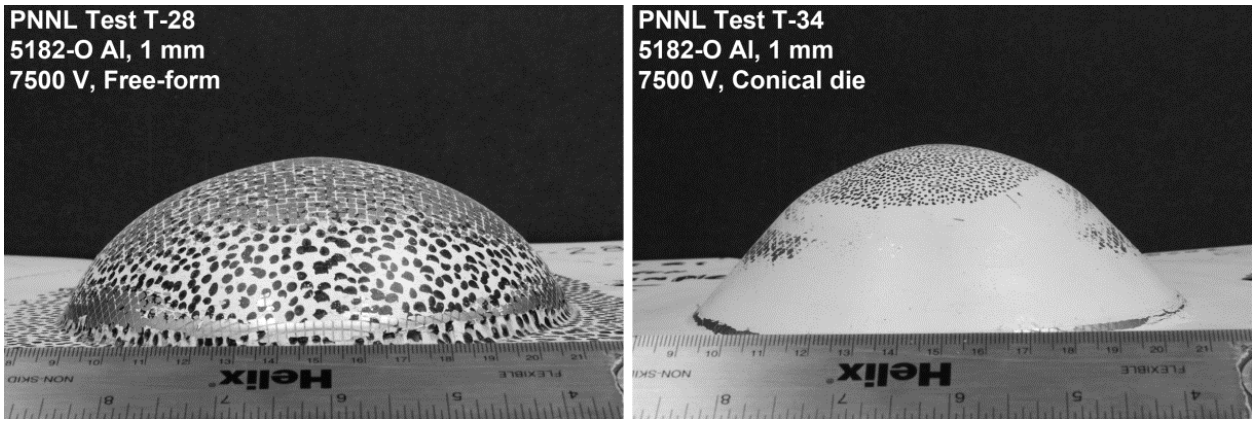

Figure 46 - Images comparing free forming and conical die forming for AA5182-O at 7500V.

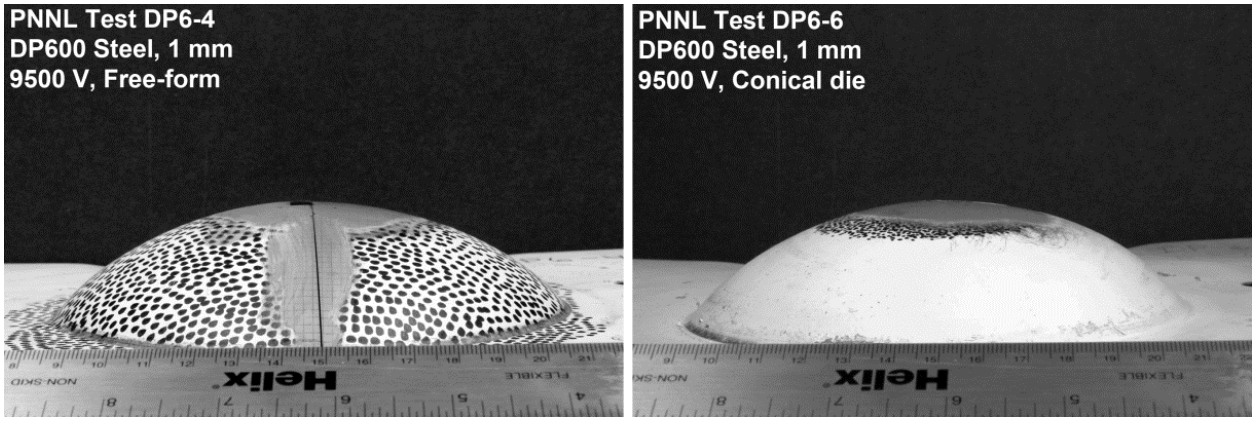

Figure 47 - Images comparing free forming and conical die forming for DP600 at 9500V.

The DIC system yielded the displacement, velocity, strain, and strain rate results for each of the specimens in Table 2. Figure 48 shows the velocity-time history at the apex of the EHF formed Al sheets at different charging voltages. The velocity-time curves for all the voltages display a similar trend with the magnitude of the sheet velocity increasing with increasing voltage. The curves are characterized by the presence of two broad maxima in sheet velocity, which occur between ~207-326 microseconds and between ~460-622 microseconds, with small undulations (e.g. at 60 and 160 microseconds) superimposed upon the overall curve. These specimens exhibited maximum observed velocities at the first maxima and were ~65 m/s, ~70 m/s and ~94 m/s at 5.0 kV, 6.5 kV and 7.5 kV, respectively. At ~650 microseconds, the sheet velocity is observed to swing from positive to negative values implying sheet's displacement away from the cameras, which is indicative of reverberations in the sheet at the end of the forming process.

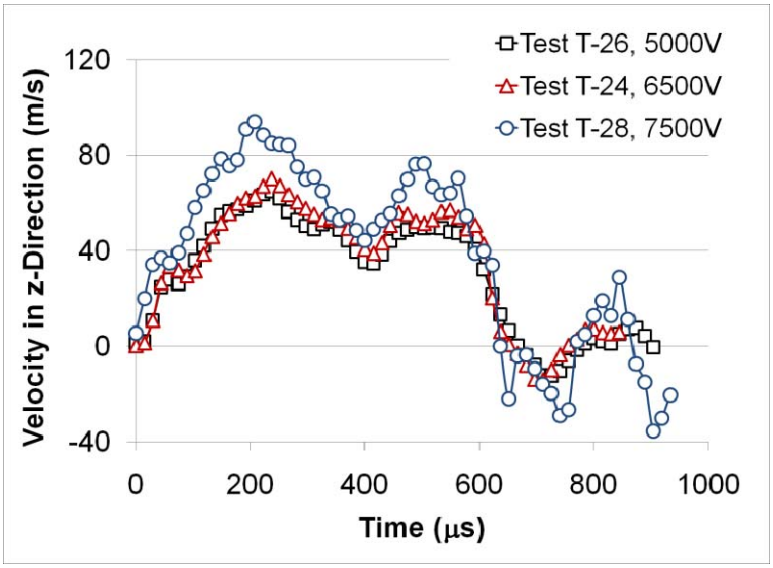

Figure 48 – Sheet Velocity (z-direction) at the apex of the free-formed AA5182 domes at different charging voltages.

Figures 49 and 50 compare the apex velocity of the free-formed and conical-die formed AA5182-O and DP600 steel domes, respectively. These curves show that the velocity-time profile for both the materials is similar and is characterized by the presence of double maxima irrespective of the charging voltage or boundary conditions (i.e. free-forming or conical-die forming). However, while the general shape (double maxima) is similar for free-forming or conical-die forming, the magnitude of the velocity is greater in the latter case for any given voltage. Specifically, for the case of Al (figure 49), at the first maximum in the velocity-time curve, the peak apex velocity in conical-die forming is ~34% and 21% greater relative to the peak apex velocity in free-forming at 6.5 kV and 7.5 kV, respectively. Further, at the second maximum (figure 49), the increase in conical-die forming velocity relative to free-forming velocity is 72% and 28% for 6.5 kV and 7.5 kV, respectively. In the case of forming of DP600 steel at 9.5 kV (figure 50), the first and the second velocity peaks in conical-die forming are ~26% and ~16%, respectively, greater than the corresponding peaks under free-forming.

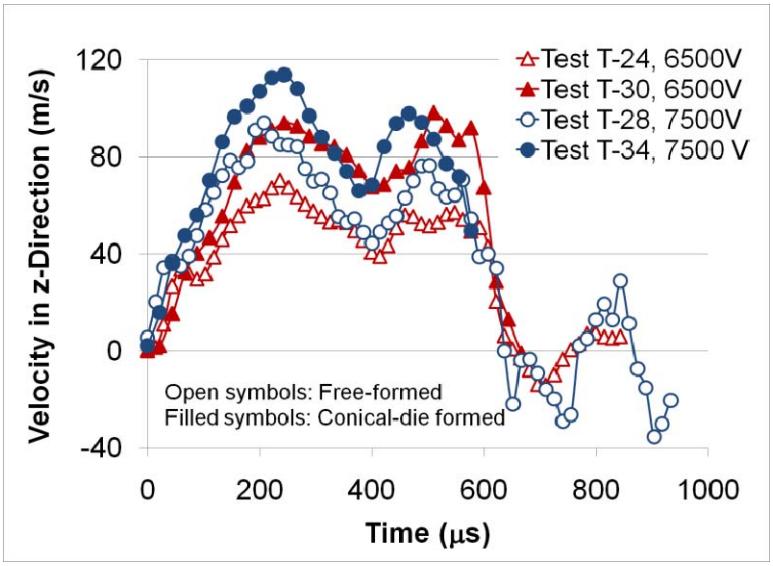

Figure 49 - Comparison of velocity (z-direction) at the apex of free-formed and conical-die formed for AA5182.

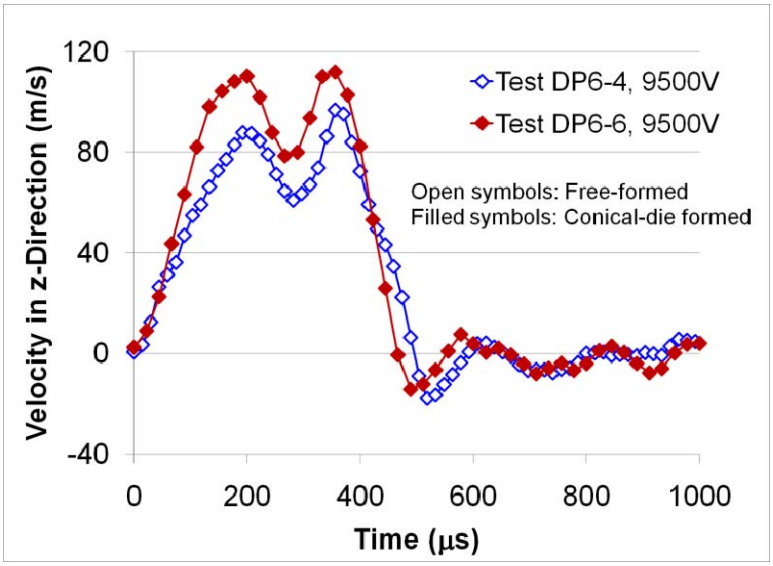

Figure 50 - Comparison of velocity (z-direction) at the apex of free-formed and conical-die formed for DP600.

Figures 51 and 52 compare the in-plane strain-rate at the apex of free-formed and conical-die formed Al and DP600 steel domes, respectively. The curves in these figures show that for both the materials, the strain-rate during conical-die forming is greater than during free-forming for the same voltage. However, unlike the case of velocity-time profiles in figures 49 and 50, the strain-rate-time profile for free-forming is quite different from that of conical-die forming. Specifically, the strain-rate curves in Al during free-forming (figure 51) show gradual rise and fall while the conical-die forming curves show many large oscillations in the strain-rate, leading up to a rapid increase (or amplification) shortly before

the end of the deformation. The maximum Lagrangian strain-rates during conical-die forming of Al are ~846 /s and ~1213 /s at 6.5 kV and 7.5 kV, respectively. These strain-rates represent an amplification of ~3.5x and ~4.5x relative to the maximum strain-rate under free-forming (~237 /s and ~271 /s at 6.5 kV and 7.5 kV, respectively). In the case of DP600 steel (figure 52), the strain-rate during free-forming shows a smooth rise and fall analogous to free-forming Al. However, the strain-rate during conical-die forming of DP600 steel shows two peaks that exceed the free-forming strain-rate curve. Thus, the maximum strain-rate during conical-die forming of DP600 steel is ~583 /s that represents an amplification of ~2.6x relative to the maximum strain-rate (~224 /s) during free-forming.

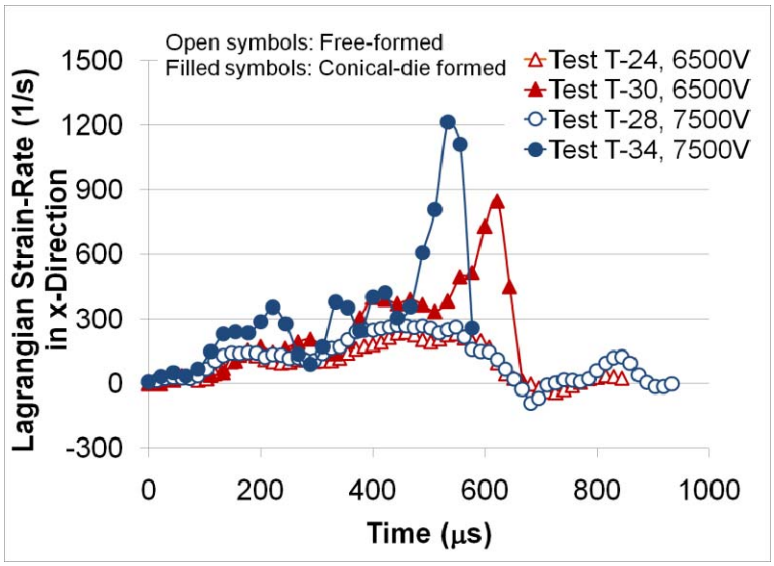

Figure 51 - Comparison of in-plane strain-rate (x-direction) at the apex of free-formed and conical-die formed AA5182.

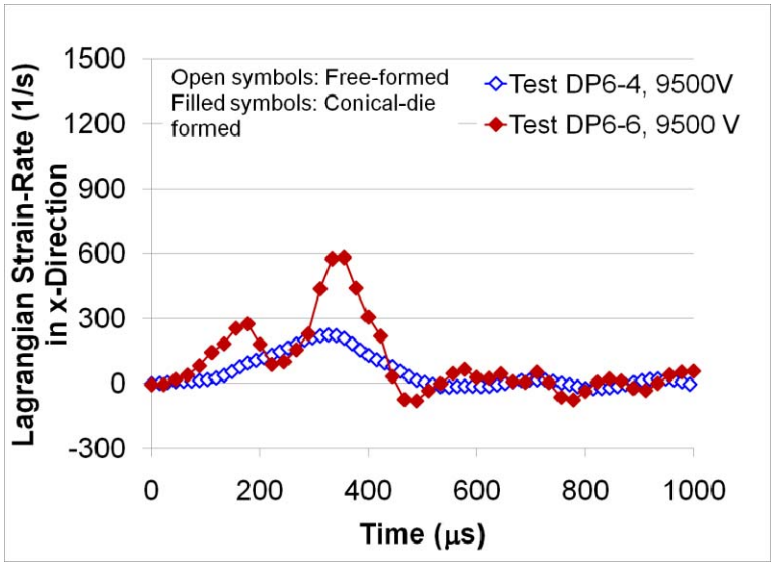

Figure 52 - Comparison of in-plane strain-rate (x-direction) at the apex of free-formed and conical-die formed DP600.

Figures 53 and 54 compare the strain-path at the apex of AA5182-O and DP600 steel domes, respectively, under free-forming and conical-die forming conditions. The data for both the materials shows that for a given voltage, the final strain achieved at the apex is greater under conical-die forming relative to free-forming conditions. For example, figure 53 shows that the final strain (x-direction) in AA5182 deformed at 6.5 kV is ~0.18 under conical-die forming as compared to ~0.11 under free-forming conditions. In the case of DP600 steel, figure 54 shows that the final strains in either direction are ~0.10 under conical-die forming as compared to ~0.07 under free-forming conditions.

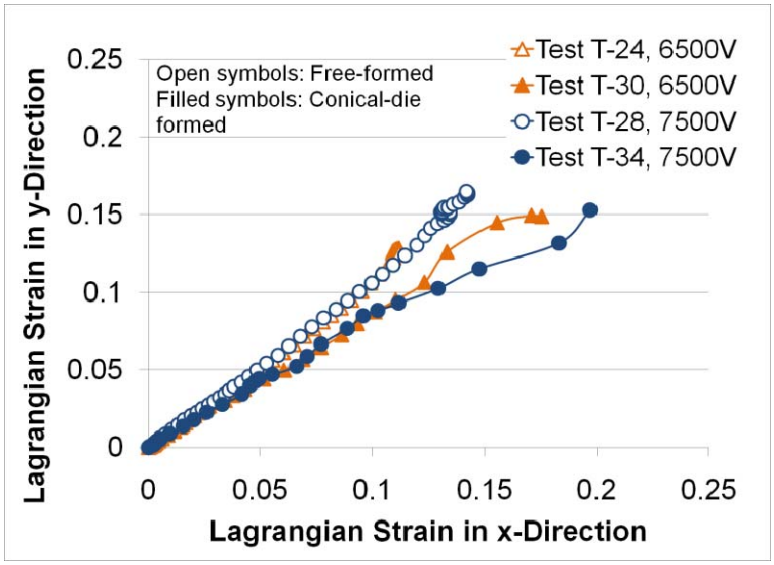

Figure 53 - Strain-path at the apex of the free-formed and conical-die formed AA5182 domes.

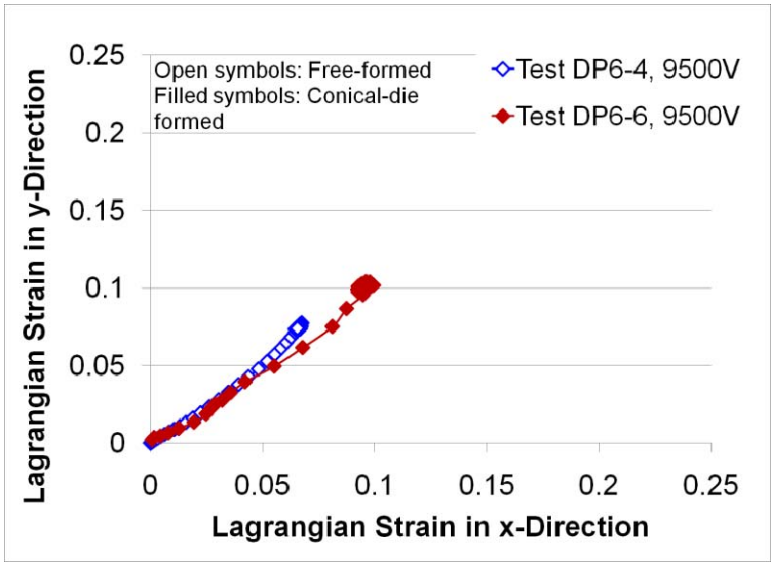

Figure 54 - Strain-path at the apex of the free-formed and conical-die formed DP600 steel domes.

Figures 49 and 50 show that the use of higher voltage, and hence, greater input energy for deformation, leads to a greater velocity. Figure 50 shows that the DP600 steel, being stronger than AA5182-O, required a higher voltage (9500 V) than Al (6500-7500 V) to achieve similar velocity magnitudes as AA5182. However, other than the difference in velocity magnitude or the voltage necessary to achieve a certain velocity, all the velocity-time curves are similar in shape, which suggests a corresponding similarity in the spatial and temporal profile of the incident pressure-pulses generated by the EHF process. However, the double-peak velocity and conical die velocity amplification features of the velocity-time curves in figure 49 and 50 require further discussion.

The double-peak velocity behavior is observed for both AA5182 (figure 49) and DP600 (figure 50). Considering that these two materials have vastly different strengths and constitutive behaviors, the double-peak behavior is attributed to the pressure-pulse profile during the EHF process. It is generally known that under-water electric discharge generates an expanding, high-pressure plasma/gas-bubble within the water that eventually collapses towards the end of the discharge process. It is this expansion and collapse of the bubble that results in a pressure-pulse whose interactions with the deformable sheet and rigid chamber walls result in a double-peak velocity-time curve of the sheet. This description of the EHF process is supported by high-speed imaging results and analysis of Tobe et al. [36], who used EHF to deform aluminum sheets. They concluded that the non-monotonic displacement-time profile of the sheet center is due to pressure wave reflection off of the moving sheet and collapse of bubbles under the sheet. Figure 55 shows the displacement-time profiles, where the inflexion points are labeled (a-c) are similar to the results of Tobe et al. [36]. However, it should be noted that the double peak behavior was obtained at the center of the sheet/dome apex. Since the pressure-pulse profile is likely to vary laterally across the specimen, the velocity-time behavior at off-center/non-apex locations may be different from that at the center/apex.

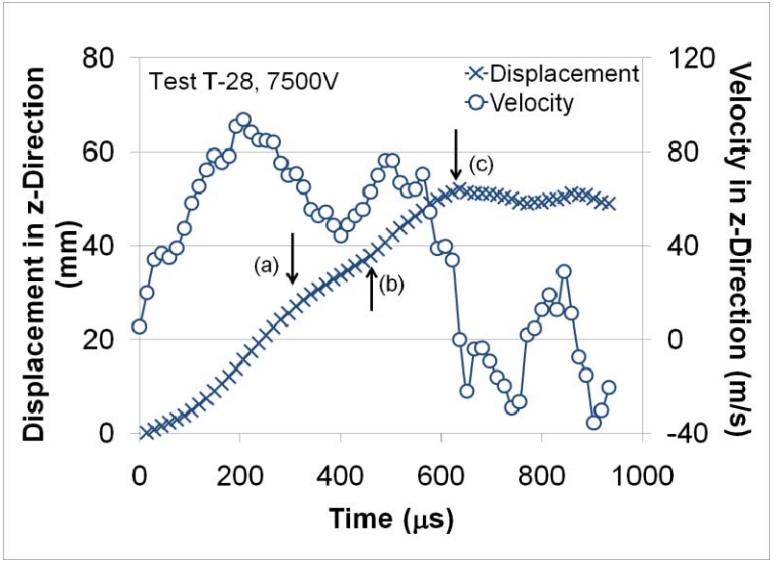

Figure 55 - Vertical displacement and corresponding velocity at the center of EHF free-formed AA5182 sheet showing the inflexion points of the displacement and velocity.

Figures 49 and 50 also show that conical die forming results in the amplification of the forming velocity. For any given voltage, the apex velocity is greater in conical-die forming than in free-forming conditions. Although the incident EHF pressure-pulse profiles are not known at present, the incident pulse magnitude at any given voltage and during the initial stages of the deformation is expected to be independent of the presence/absence of the conical die since the test sheet has not yet impacted the die. Moreover, the velocity amplification is seen in both the AA5182 and DP600 materials. Therefore, the greater velocity during conical-die forming cannot be attributed to differences in the incident pressure-pulse or material behavior. The conical shape of the die appears to result in a "focusing" action as the pressure-pulse moves from the EHF chamber towards the die apex, as the rigid die constrains the sheet upon impact with the die and forces the deformation to occur in a gradually decreasing area. Based on this argument, the focusing effect is expected to be a function of the die angle when all other conditions stay the same. In this work, a die angle (apex) of 84° was used. Although EHF with additional dies of different angles was not attempted in this work, initial numerical modeling assuming an exponentially decaying pressure-pulse has confirmed the dependence of maximum apex velocity on the die angle.

In the prior literature, EMF inside a conical die has been shown to result in larger regions with enhanced formability [37] or greater formability [34] as compared to free-forming conditions. However, the reasons behind improved formability, when forming inside a conical die, were not clear. While early work by Balanethiram and Daehn [31, 32] used a conical die and attributed enhanced formability to "high" strain-rates, the strain-rates were estimated at best and no attempt was made to clarify the role of conical die in comparison with free-forming conditions. Using numerical modeling and experimental analysis of post-mortem strain distribution on EMF formed parts, Imbert et al. [37]concluded that a combination of high strain-rates and sheet-die interactions (through-thickness and shear stresses and strain-path changes) were responsible for enhanced formability when forming inside a die. However, this work appears to be the first to provide experimentally measured strain-rates as well as to quantify the differences in the deformation history under free-forming and conical-die forming conditions.

Numerical modeling of EMF of AA5754 sheet inside a conical die [37] has shown that the sheet location that impacts the die shows significantly non-proportional loading following impact. Imbert et al. [37] also noted that the non-proportional strain-path makes direct comparisons of formability with conventional forming limit diagrams difficult, since the latter were developed with the assumption of a linear and proportional strain-path. Hence, a priori assumption of a proportional and linear strain-path during EHF or EMF can lead to incorrect analysis and conclusions. Although the experimental technique developed in this work can be utilized to verify the strain-path under free-forming, it is somewhat limited when forming inside a die since the technique is image-based and the die blocks the cameras' access to the speckle pattern on the sheet. Nevertheless, in an experimental setup, it may be possible to machine openings inside the die and allow cameras to view the sheet deformation, as demonstrated in this work. Quantitative information from such investigation can be used to validate models which can be used, with a greater degree of confidence, to model the sheet locations that are hidden from the camera.

4.4 Experimental Results of Formability

The experimental investigations described above provide significant insight into the displacement, velocity, strain, and strain rate developed in sheet metal during PPF. However, this element of the experimental research involves characterizing the forming limits of the materials under different modes of deformation. The enhanced ductility of sheet metals during PPF is one of the most attractive commercial advantages of the overall process, and the methods to attain it must be further described. The results above demonstrate the methodology and approach to experimentally evaluating PPF, but do not show a significant increase in formability. Therefore, additional work is required to achieve enhanced ductility.

Figure 56 shows a compilation of various free forming and conical die forming experiments shown on a conventional forming limit diagram (FLD). The plot shows the true plastic strain that developed in each of the specimens in both the x and y directions during the forming event. The plot also shows the peak true strain rate that was developed and measured in the specimen during the forming event. The most remarkable element of this plot is that no significant enhanced ductility was achieved in any of the specimens in the region of the specimen that was undergoing free forming. However, the peak true strain rates achieved in all of the specimens is significantly below the true strain rate of 10^3/sec, which was shown in the constitutive relations for aluminum alloys to be a significant inflection point for the strain rate sensitivity of the materials. Therefore, for the given system, the technical focus of the work was aimed to characterize the extended ductility as a result of die impact, and developing and designing a specimen to achieve higher strain rates in the subject materials.

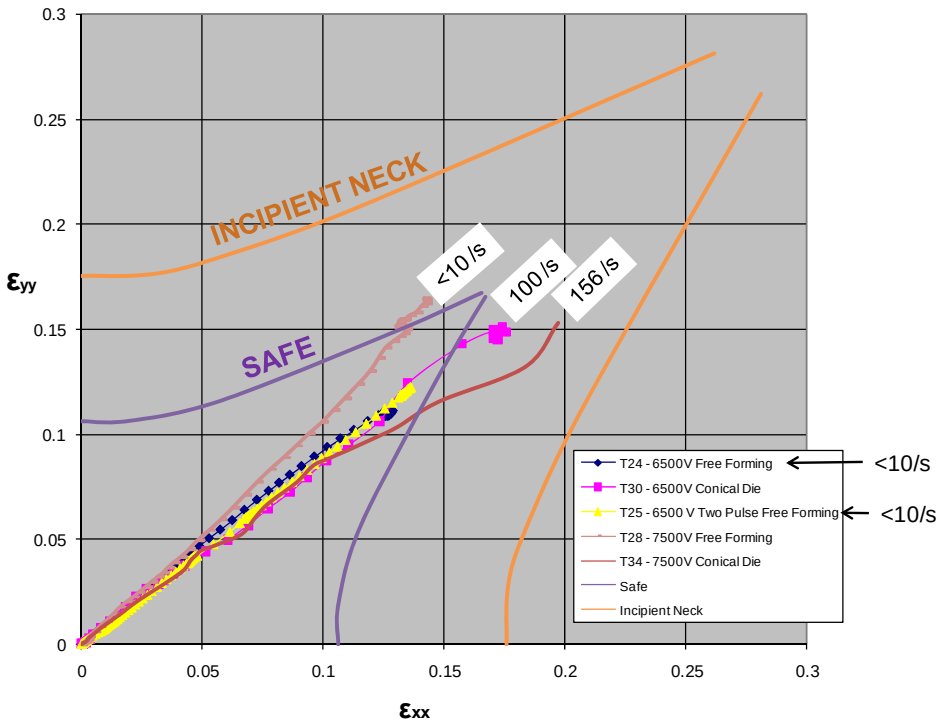

Figure 56 - Various free forming and conical die forming experimental results compiled on an FLD.

Figure 57 is an example of a specimen that was formed using the conical die apparatus, wherethe specimen failed in the region that was in contact with the die. Since the material is in contact with the die, no direct experimental observation can be made of the strain rate that was achieved during the deformation. Therefore, in this case, a strain grid measurement technique was applied to an area adjacent to the fracture to determine the amount of deformation that was developed prior to fracture. The results showed that the material achieved a peak engineering strain of 0.65 in the major direction in a near plane strain condition. This represents a near six times increase in the formability of the material compared to quasistatic forming. During this test, the high-speed cameras and DIC system measured the peak strain rate on the apex of the dome, which was not in contact with the die. These measurements yielded a peak true strain rate at the apex of the dome of ~250/sec. However, numerical modeling has shown that the area in contact with the die experiences both hydrostatic stress and a major amplification of the instantaneous strain rate [37], where both effects are believed to yield higher overall formability. However, this particular conclusion does not permit an explanation of how enhanced ductility is achieved under free forming conditions.

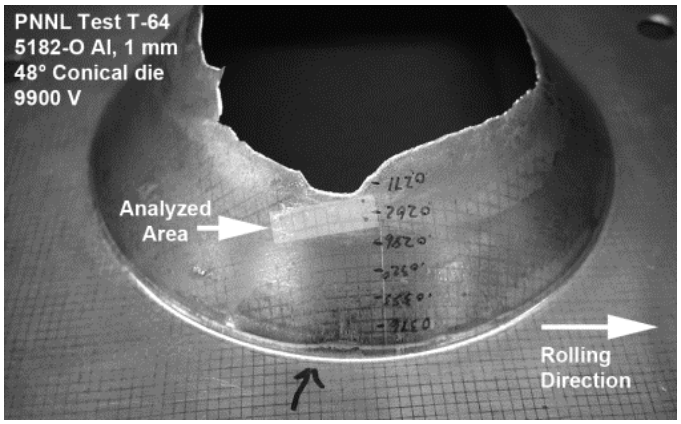

Figure 57 - A specimen formed under conical die forming conditions where failure occurred around the region where the die contact was made.

The need to achieve higher strain rates during free forming resulted in the design of a unique specimen in an attempt to amplify the strain rates using the existing EHF apparatus. Figure 58 contains a modified specimen that was developed in order to achieve strain directions near plain strain, while simultaneously amplifying the strain rate through the gage area of the specimen. Since the material was perforated, the experimental procedure required the use of secondary (i.e. driver) sheet be placed between the water in the EHF chamber and the modified specimen. In effect, the EHF chamber would be driving a single continuous sheet and a perforated sheet, which both consisted of AA5182-O material of 1 mm thickness.

Figure 59 shows a photograph of the modified specimen after testing at a capacitor bank charge voltage of 8500V. The failure in the specimen initiated across the center of the gage area, and inertia caused the further deformation of the specimen to open its final shape shown. Figure 60 contains an instantaneous measurement of the strain that existed in the material immediately prior to fracture from the high speed camera DIC system. This image was obtained from the DIC system at the last possible image before total failure occurred in the specimen. Figure 61 illustrates the velocity profile at the apex of the dome as a function of time during forming. The data shows that the peak performing velocity is approximately 146 m/s, and it also has the characteristic double peak velocity described earlier. However, in this case, the specimen failed midway through the second velocity peak. Figure 62 illustrates the Lagrangian strain rate versus time for the modified specimen. This figure shows that the modified specimen results in a significantly amplified strain rate in the material during the majority of the forming event; with the peak true strain rate achieving ~1800/sec. Figure 62 also shows that the strain rate and accumulation of strain in the minor direction is relatively small.

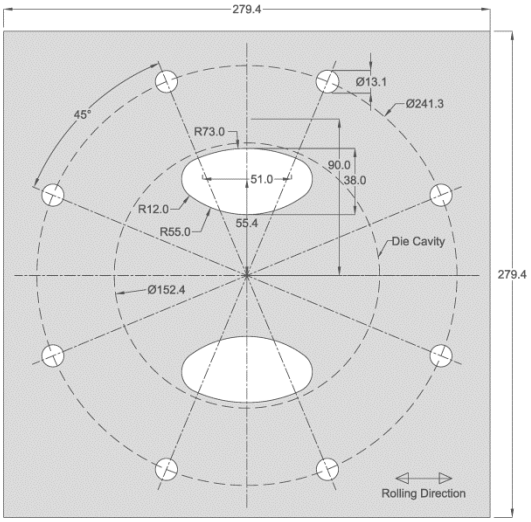

Figure 58 - Specimen designed to amplify the strain rates during free-forming.

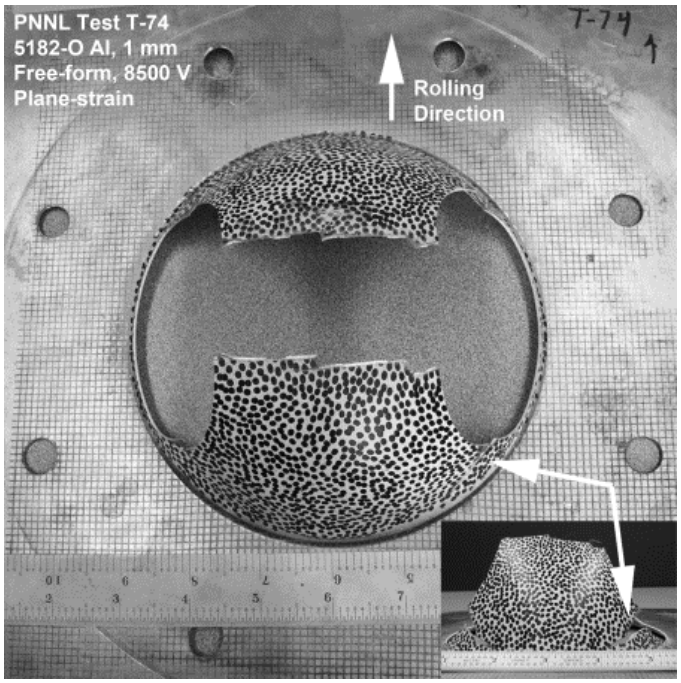

Figure 59 - Photograph of the modified specimen after testing.

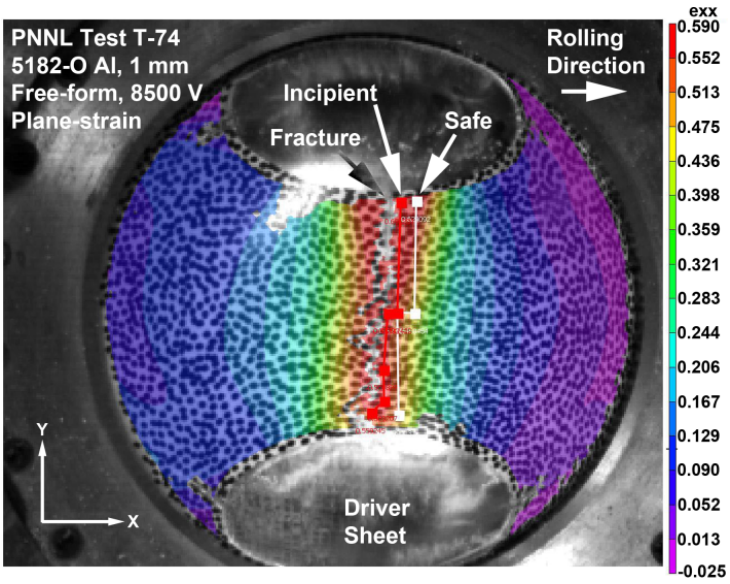

Figure 60 - DIC determined Lagrangian strain in the modified specimen at the instant of failure.

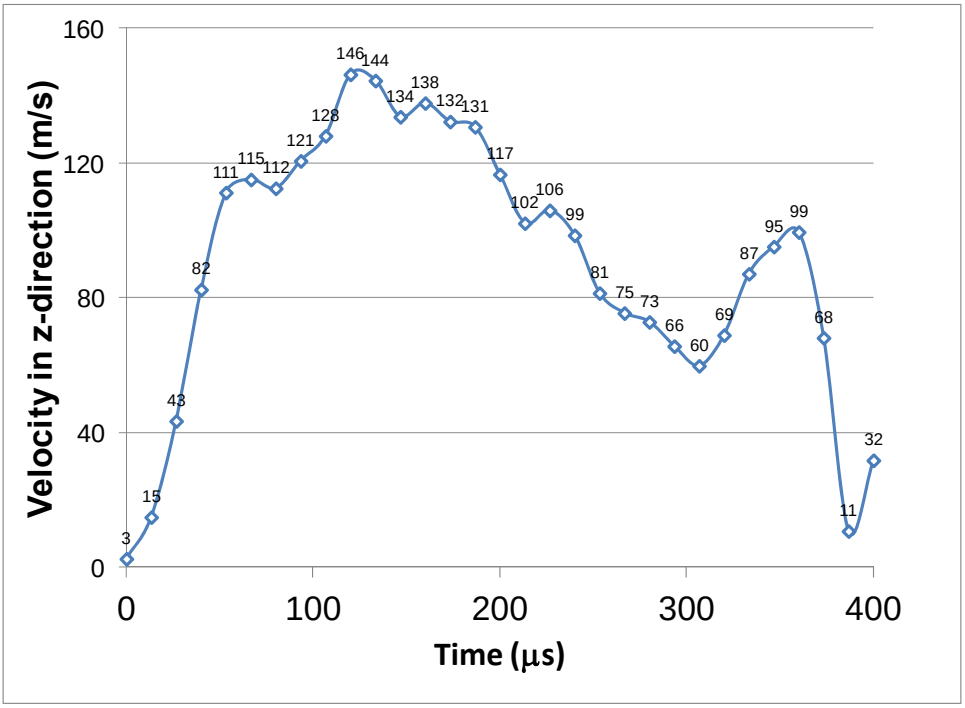

Figure 61 - The velocity at the apex of the modified specimen during the forming event.

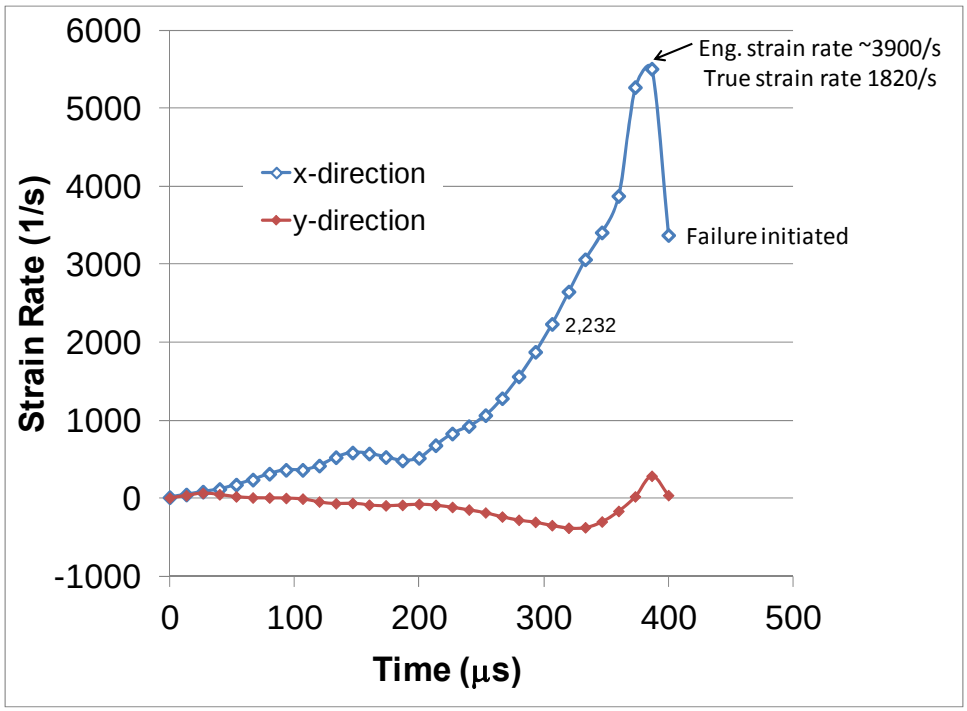

Figure 62 - The Lagrangian strain rate in the specimen as a function of time in the x and y direction, where the x direction is coincident with the gage length of the specimen.

Figure 63 illustrates the combined results of the quasistatic FLD for the AA5182-O material, the results of the specimen formed with die contact (figure 57), and the formability results of the modified specimen (figure 59). All data shown in figure 63 are presented in engineering strain and engineering strain rate for reference. The figure illustrates that die contact at high rates can improve the formability by a factor of six over conventional quasistatic free forming FLD. Furthermore, achieving engineering strain rates of ~3900/sec (true strain rate of 1.8×10^3/sec) during free forming enables formability that is 2.5 times higher than the conventional quasistatic free forming FLD.

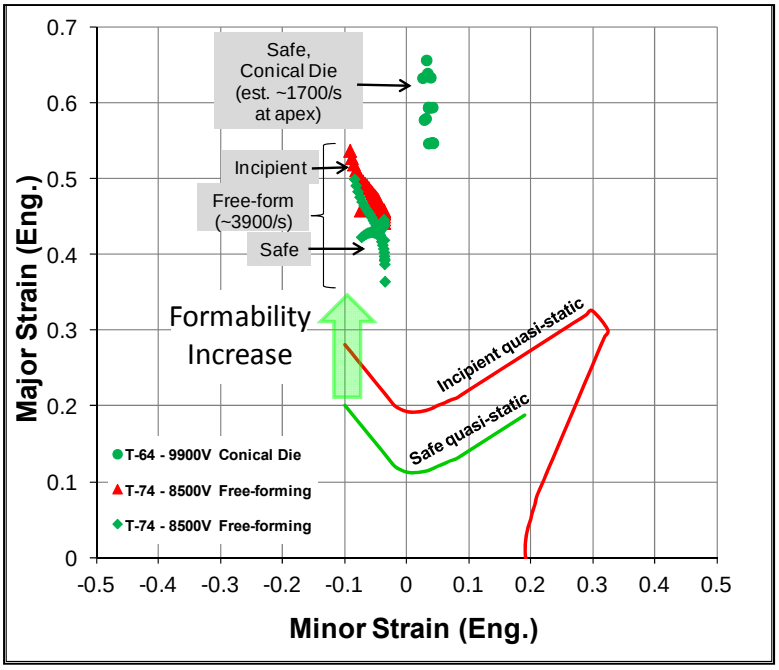

Figure 63 - Combined results of the quasistatic FLD for the AA5182-O material, the results of the specimen formed with die contact, and the formability results of the modified specimen.

This room temperature formability investigation of 5182-O Al alloy sheet (1 mm thick) appears to be the first instance where detailed quantitative deformation history at high strain-rates has been experimentally determined and reported. The work has shown to enhance AA5182-O formability by ~2.5X and ~6X under free-forming and conical-die forming conditions, respectively, via EHF technique. The deformation history associated with the formability enhancement under free-forming conditions was quantified, where the strain-path was experimentally demonstrated to be proportional and close to plane strain; while the maximum in-plane engineering strain-rate and maximum sheet-normal velocity were ~3900 /s and ~146 m/s, respectively.

In order to explain the differences in material formability during free forming across different strain rates, mechanical properties of the subject material were investigated through uniaxial tension testing. Chapter 5 contains the results of this constitutive relation investigation, and is subsequently employed to explain why enhanced formability was not observed during free forming at strain rates less than 10^2/sec.

5 Mechanical Properties during PPF

The work under Chapter 5 is designed to overcome the technical barrier that is the lack of validated constitutive relations for lightweight materials during PPF processing. This work investigates the microstructure and mechanical property evolution in metals during PPF. Most metallic materials exhibit significant changes in flow stress based on strain rates [9] and mechanical property and microstructure variation [10]. The focus of this work is determining the constitutive relations of aluminum alloy AA5182 and high-strength steel alloy DP600 at PPF strain rates. Major elements of this work have been recently submitted for publication [11].

5.1 Experimental Characterization of Mechanical Properties

Strain-rates during room temperature forming of sheets to make automotive components can range from quasistatic (e.g. hydroforming) to those exceeding 10^3/s when applying processes such as electromagnetic or electrohydraulic forming. This work investigates the constitutive relations and develops a constitutive model to describe the room temperature behavior of aluminum alloy AA5182-O (Al-4.5Mg-0.35Mn) and DP600 (Fe-0.07C-1.79Mn) steel across the strain-rate range from $1x10^{-3}$/sec to $2.5x10^3$/s. Both of the sheet materials were 1mm in thickness.

The experimental investigation consisted of uniaxial tensile testing using conventional servo-hydraulic tensile frame and Split Hopkinson Pressure Bar (SHPB). Figure 64 is a drawing of the specimen that was used for the experimental work. The servo-hydraulic tensile testing investigated the materials at constant true strain rates of $1x10^{-3}$/sec, $1x10^{-2}$/sec, and $1x10^{-1}$/sec. The SHPB testing investigated the materials at nominal true strain rates of 10^3/sec, $2x10^3$/sec, and $2.4x10^3$/sec. Figure 65 contains the experimental results of the tensile test for the AA5182-O sheet in the rolling direction. These results show a decreasing flow stress with increasing strain rate from $1x10^{-3}$/sec to $1x10^{-1}$/sec. However, this tread appears to reverse with increasing flow stress with increasing strain rate from $1x10^3$/sec to $2.4x10^3$/sec. Overall, the quasistatic flow stress of the materials appears to be ~140MPa.

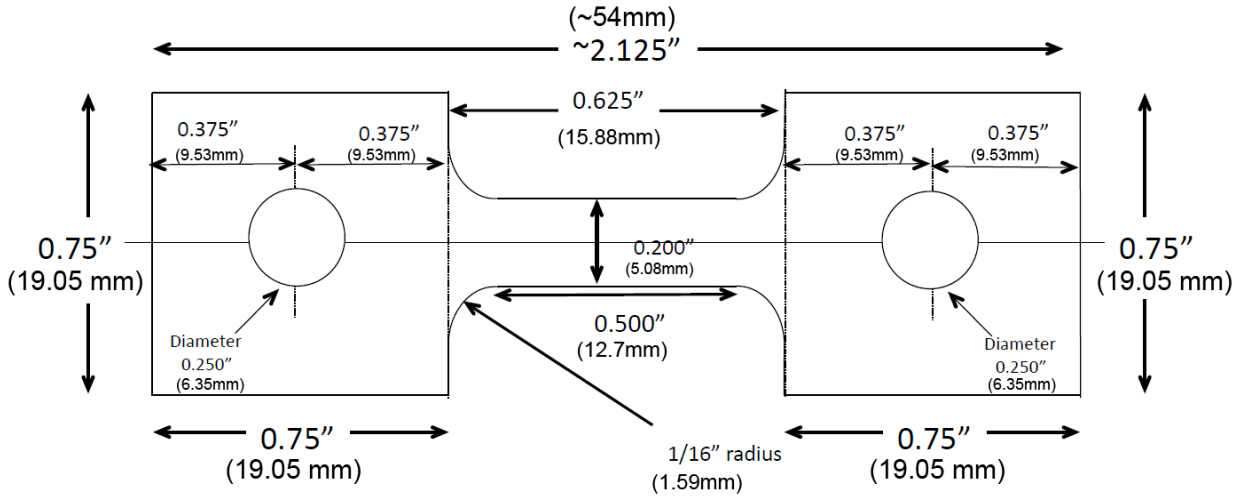

Figure 64 - Drawing of the tensile specimen used to conduct the mechanical testing.

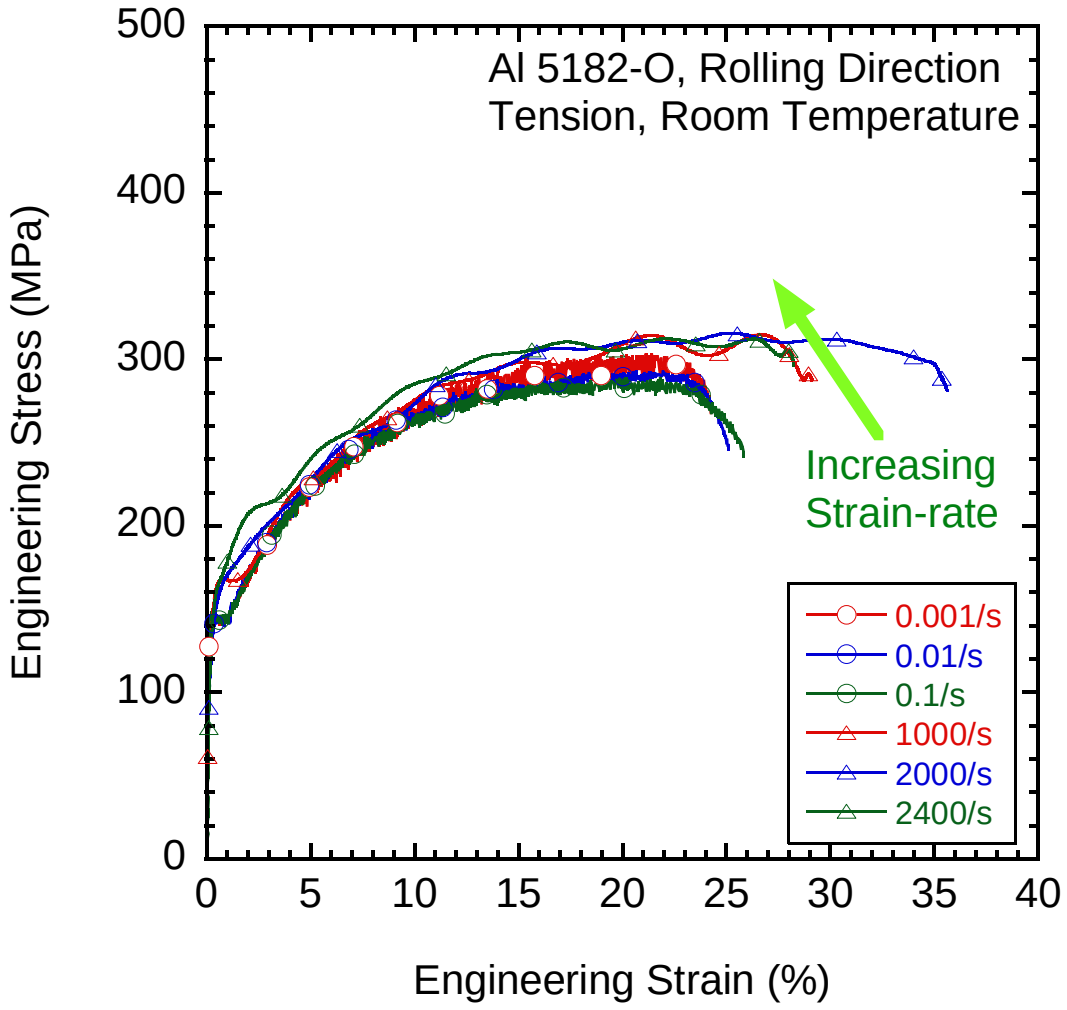

Figure 65 - Tensile test experimental results for AA5182-O in the rolling direction.

Figure 65 also shows that the material exhibits some yield point elongation as well as some serrated flow in the stress-strain diagram, which is a classical behavior of an aluminum alloy with relatively high magnesium content (Dynamic Strain Aging (DSA) effects will be discussed later). The figure also shows that the specimens tested at high rate also exhibited higher elongation during testing. Figure 66 shows the results of the tensile tests where the tensile axis was aligned transverse to the rolling direction. These results show a similar flow stress, and similar trend in the exhibited flow stress across the strain rates tested. The similarity in the strain hardening and the response to varying strain rates in both the rolling and transverse direction permits the material to generally classified as an material with isotropic hardening characteristics, which permits the application of a simplified constitutive model to describe the materials. The constitutive relations determined in this experimental investigation are consistent with the results of past characterization of AA5182-O alloys [46, 49, 50, and 51]

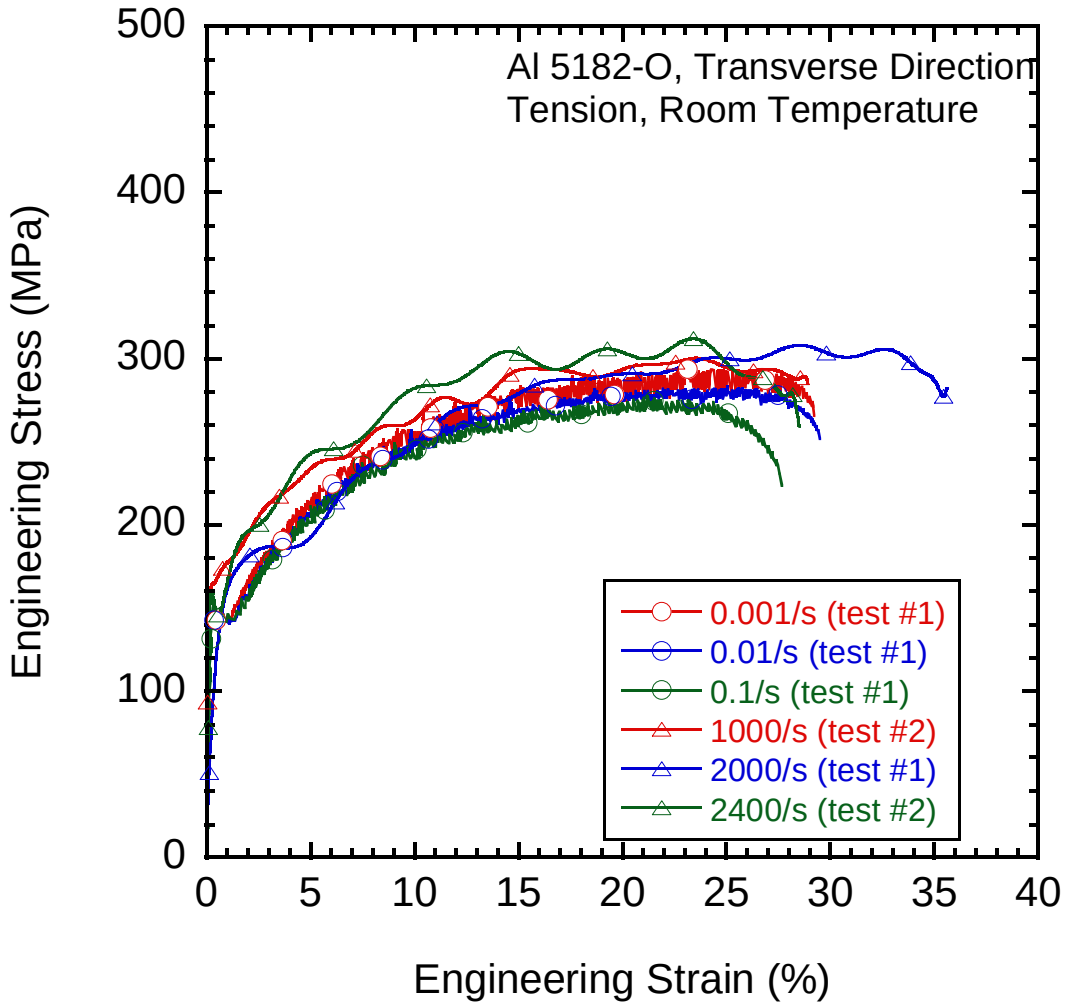

Figure 66 - Tensile test experimental results for AA5182-O transverse to the rolling direction.

The constitutive relations of the DP600 steel were investigated with an identical technical approach as described above. Figure 67 contains the experimental results of the tensile test for the DP600 sheet in the rolling direction. These results show a generally increasing flow stress with increasing strain rate across all tested strain rates. Overall, the quasistatic flow stress of the materials appears to be ~350MPa. In the case of the DP600 steel, one can observe from the engineering stress-strain diagram that the materials reach the ultimate stress relatively early in the testing. In fact, nearly half of the elongation occurs after the ultimate strength of the material is reached, and in a post uniform elongation mode of deformation. This is expected with a material that has positive strain rate sensitivity, and in contrast to the expected and observed behavior of very low post uniform elongation in the AA5182 alloy, which has very low or negative strain rate sensitivity.

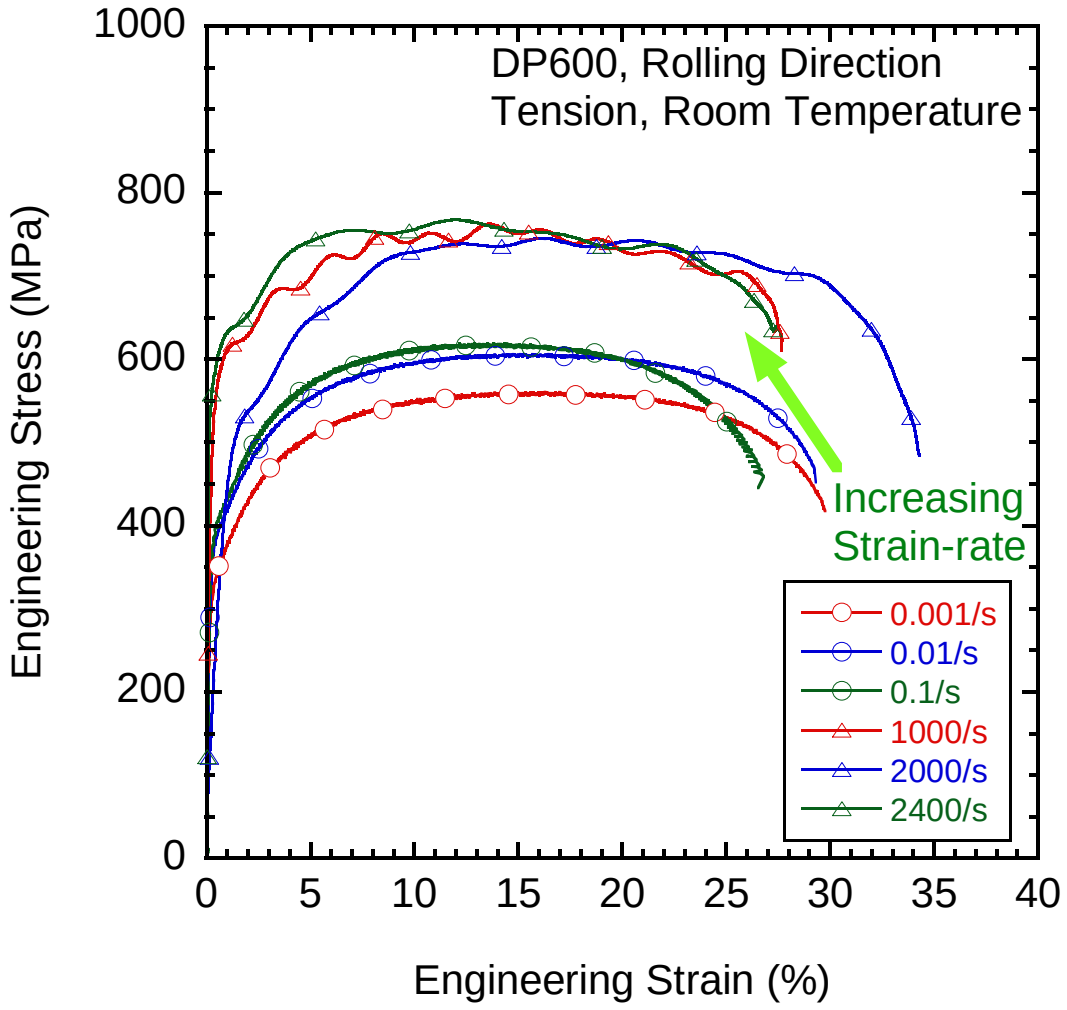

Figure 67 - Tensile test experimental results for DP600 in the rolling direction.

Figure 68 shows the results of the DP600 tensile tests where the tensile axis was aligned transverse to the rolling direction. These results show a similar flow stress, and similar trend in the exhibited flow stress across the strain rates tested in the rolling direction. The similarity in the strain hardening and the response to varying strain rates in both the rolling and transverse direction permits the material to generally classified as an material with isotropic hardening characteristics, which permits the application of a simplified constitutive model to describe the materials. The constitutive relations determined in this experimental investigation are consistent with the results of past characterization of DP600 alloys [53, 54]

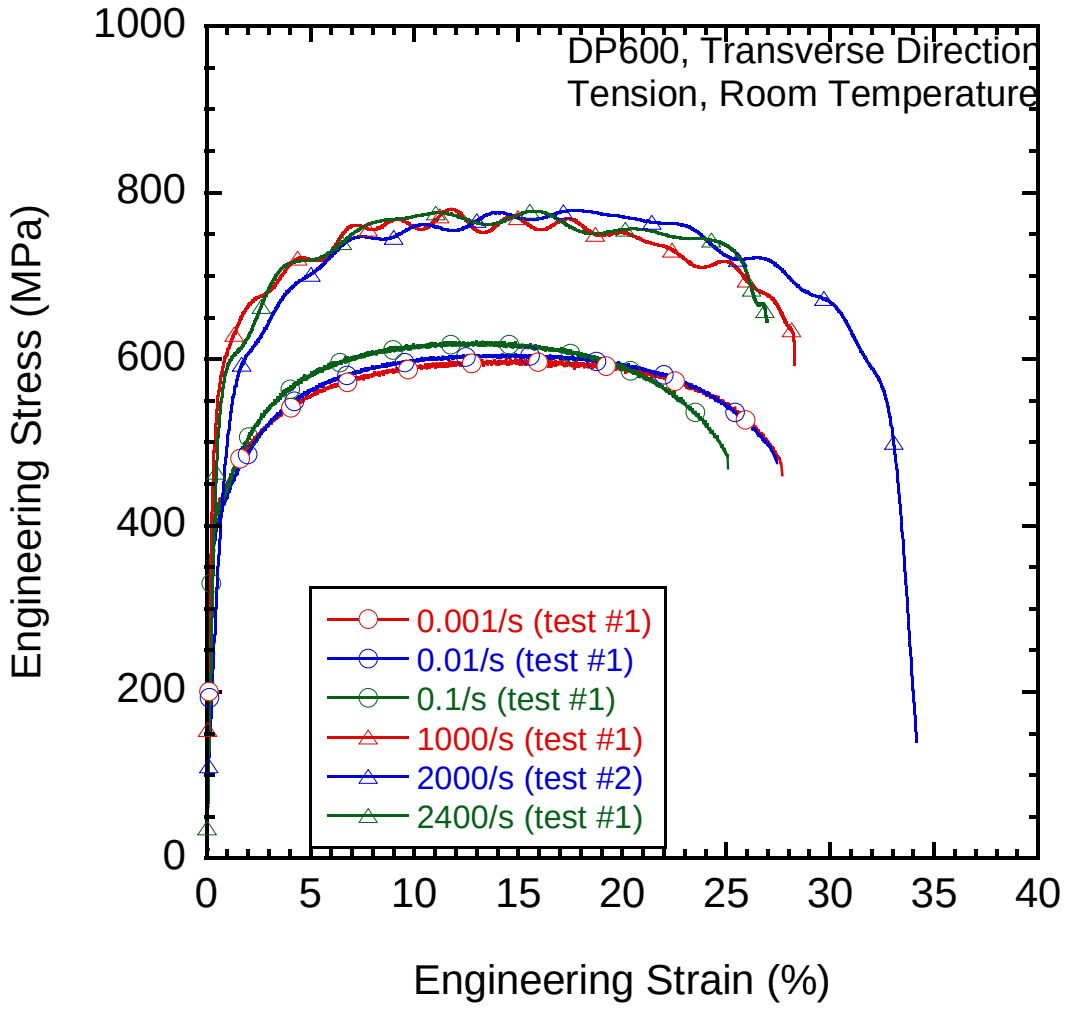

Figure 68 - Tensile test experimental results for DP600 transverse to the rolling direction.

In order to develop a predictive formability model that employs these observed constitutive relations, these experimental observations must be described using a constitutive model. The constitutive model must be effective and valid across the strain rate range of quasistatic to ~10^4/sec if PPF processes are going to be accurately described, since the experimental work that investigated the PPF strain rates (Chapter 4) directly observed this wide range of strain rates.

5.2 Developing a Constitutive Model

There have been many constitutive relations proposed and developed over the past 70 years or more. Liang and Khan [67] conducted a critical literature review and identified four constitutive relations that are widely applied to the present problem: Johnson-Cook, Zerilli-Armstrong, Bodner-Partom, and Khan-Huang models. The Johnson-Cook [68] model appears to be one of the most widely applied rate dependent constitutive relations, and others have proposed modified versions of the same to improve the accuracy of the correlation to the experimental data. However, these and most other models

generally have five or many more material constants or parameters that require extensive data-gathering, as well as require data or assumptions about material properties at various temperatures or under adiabatic heating that may result at high strain-rates. One of the earlier and simple constitutive relations was a power law formulation proposed by Hollomon [69].

Hollomon proposed two versions of a power law where flow stress was proportional to the strain or strain-rate raised to the power *n* or *m*, respectively. However, the more generalized version uses these two power laws in combination as shown in Equation 1 [70].

$$\sigma = K\bar{\varepsilon}^{n}\dot{\bar{\varepsilon}}^{m} \qquad (1)$$

where $\bar{\varepsilon}$ is the effective strain, $\dot{\bar{\varepsilon}}$ is the effective strain-rate and *K*, *n* and *m* are constants to be determined through experiments. The existence of only three material constants makes the constitutive relation elegant for its simplicity. However, the relation suffers from a general lack of flexibility when the behavior of the materials becomes modestly complex. For example, the variability in the strain-rate sensitivity of AA5182, as shown in Figure 1, cannot be captured by Equation 1 in its present form. Therefore, in order to better describe the more complex flow stress behavior of AA5182 using the Hollomon equation (Equation 1), the current work treats the strain rate sensitivity *m* as a variable function of strain-rate. As a first approximation, *K* and *n* are assumed constant as usual, but the strain-rate sensitivity *m* of the material is a linear function of strain-rate as shown in Equation 2:

$$m = A\dot{\bar{\varepsilon}} + m_{quasistatic} \qquad (2)$$

where $m_{quasistatic}$ is the strain-rate sensitivity at some reference quasi-static rate approaching zero. Other alternatives to the linear relation were also considered. However, the linear relation (Equation 2) proved to suitably describe the variable strain-rate sensitivity of the current materials, as shown later by the adequacy of fit to the experimental data, while retaining the relative simplicity of the constitutive relation. Substituting Equation 2 into Equation 1 yields the generalized version of the constitutive relation:

$$\sigma = K\bar{\varepsilon}^{n}\dot{\bar{\varepsilon}}^{(A\dot{\bar{\varepsilon}}+m_{quasistatic})} \qquad (3)$$

Although the above modification to Hollomon's original power law equation increases the number of material constants from three to four, as shown subsequently, the proposed modification significantly increases the flexibility of the power law model to describe material behavior across a wide range of strain-rates.

Equation 3 assumes that the material hardening behavior is isotropic. Furthermore, the model does not include any effect of material temperature due to adiabatic heating resulting from the plastic work in the formulation. No attempt is made to characterize the adiabatic heating in this model for three

specific reasons. First, no temperature data is available from the tensile testing or the PPF tests. Any inclusion of temperatures would be based on estimates that are not explicitly known, and they have been shown to be a margin contribution based on past calculations by Thomas and Triantafyllidis [62]. Second, the PPF specimens are in contact with water during the forming event, and so temperature estimates would be unclear given the near immediate quenching of the materials during forming. Thirdly, adiabatic heating is a significant influence on the flow stress during tensile testing (e.g. at high strain-rates), and the constants in Equation 3 are determined in a way that implicitly includes the effects of adiabatic heating. Therefore, the simplification of the constitutive model to implicitly include the temperature effects is thought to be an adequate approach. Future work may need to address this topic more fully.

The application of the proposed model requires five steps. Step one is obtaining room temperature tensile stress-strain curves across the strain-rate range of interest with multiple samples tested per strain-rate to increase confidence in the data/model. Step two involves determining coupled true stress-true strain data points at discrete plastic strains (e.g. 0.05, 0.10, 0.15, etc.) for each specimen. Step three is to determine the constants *K* and *n* by selecting a reference strain rate and determining the constants via a basic curve fit of the power law (Equation 1) to tensile tests done at the reference strain-rate. Step four is to substitute the constant *K* and *n* values (determined in Step three) into Equation 1 and calculate a unique value for strain-rate sensitivity (*m*) for each discrete set of coupled true stress-true strain data points (from Step two). Thus, Step four will result in *m* values for each coupled true stress-true strain data point with as many *m* values per strain-rate as the number of repeat tests at that strain-rate. Finally, in step five, a linear fit of *m* against the strain-rate will yield the slope and intercept as the constants A and $m_{quasistatic}$, respectively, for Equation 2.

Steps one and two described above simply involve standard mechanical testing and analyzing the stress-strain curves. However, in step three there are two methods to establish the quasistatic strain-rate sensitivity. The first (and preferred) method is to obtain true stress versus true strain tensile data at strain rate of 1 /s, since at this strain-rate the rate term in Equation 1 becomes unity and the values of K and *n* can be determined regardless of the value of strain-rate sensitivity. The second method to establish the strain-rate sensitivity at a reference strain-rate is by conducting two tensile tests or one tensile test with multiple rates (strain rate jump tests) to calculate the strain rate sensitivity at a known reference strain-rate. The determination of two flow stress values at two reference strain rates allows the calculation of the strain-rate sensitivity for the material using $m = \log(\sigma_2 / \sigma_1) / \log(\dot{\varepsilon}_2 / \dot{\varepsilon}_1)$[7]. Having experimentally determined the strain-rate sensitivity *m* at the reference strain-rate, the values of *K* and *n* can then be obtained by curve fitting the power law (Equation 1) to the stress-strain experimental data at the reference strain rate. For subsequent calculation, K and *n* are treated as constants for all the strain-rates. Step four requires calculating the strain rate sensitivity at a given strain, strain rate, and flow stress, which is done by solving Equation 1 for *m* yielding:

$$m = log_{\dot{\bar{\varepsilon}}}\left(\frac{\sigma}{K\bar{\varepsilon}^n}\right) = log\left(\frac{\sigma}{K\bar{\varepsilon}^n}\right)\Big/\log(\dot{\bar{\varepsilon}}) \qquad (4)$$

Using *K* and *n* calculated in Step 3, Equation 4 yields a unique value of strain rate sensitivity for a given stress, strain, and strain-rate combination.

The above methodology provides a simple and generalize constitutive model for room temperature forming across a wide range of strain rates. The suitability and general accuracy of this model will be evaluated by applying the above described methodology to the data of Higashi et al. [47] and to newly obtained results from the current work for AA5182; as well to a DP600 population of material in the sections below.

5.3 Constitutive Model and Microstructure for AA5182

This work develops a constitutive model that describes the room temperature tensile behavior of an aluminum alloy Al-4.5Mg-0.35Mn (AA5182) across the strain-rate range of 10^{-3} /s to $2.5x10^{3}$ /s. The tensile properties of a 1mm thick sheet were experimentally investigated and described above, and are compared with results published in the literature. The modified power law constitutive model is described according the procedure above for the materials. The constitutive model and experimental results are generally compared, and differences between the behaviors of two materials are discussed.

Higashi et al. [47] used hydraulic tensile machines and Split Hopkinson Pressure Bar (SHPB) to determine the room temperature uniaxial tensile behavior of annealed AA5182 across the strain-rate range of $1x10^{-3}$/s to ~$2.5x10^{3}$/s. This previously published experimental data is plotted in Figure 69 as flow stress vs. strain-rate for different levels of plastic strain. The data points in Figure 69 were extracted from individual stress-strain curves obtained at a fixed strain-rate. As shown in Figure 69 and as observed by Higashi et al. [47], AA5182 alloy exhibits generally decreasing flow stress across the strain-rate range of $1x10^{-3}$/sec to $1x10^{2}$/sec (i.e. negative strain-rate sensitivity) and a generally increasing flow stress above $1x10^{2}$/sec (i.e. positive strain-rate sensitivity). The primary purpose of this work is to develop a constitutive model that can capture such variability in the strain rate sensitivity (SRS) and is simple enough to be readily implemented in commercial simulation codes or for use in analytical material modeling.

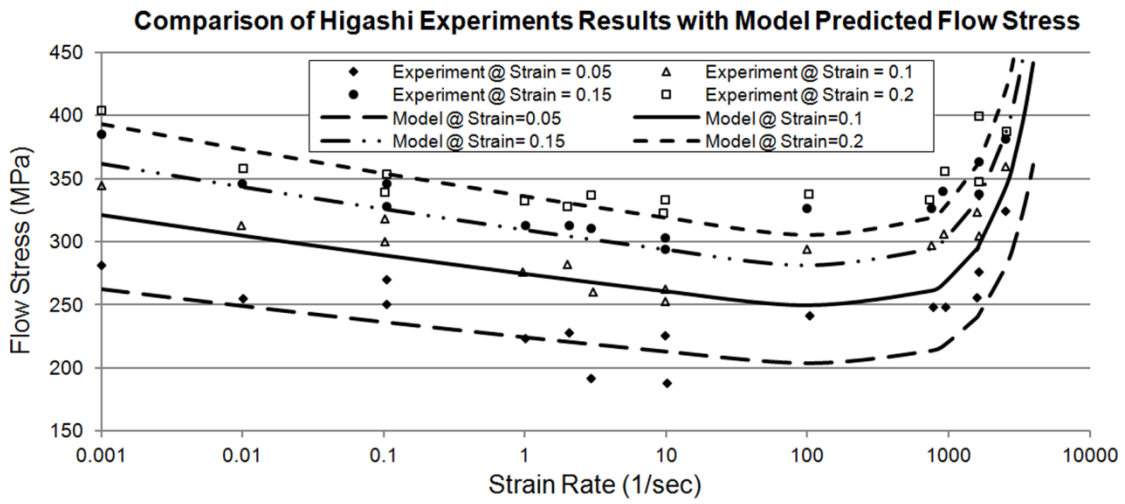

Figure 69 - The experimental flow stress data from Higashi et al. [47] and its comparison with the modified power law constitutive model (Equation 5).

The suitability and general accuracy of the proposed constitutive model will be evaluated by applying the above described methodology to the data of Higashi et al. [47] and to that obtained in the new experimental results presented above. The stress-strain-rate data points in Figure 69 were taken from Higashi et al. [47] and the constants *K* and *n* were determined to be 538 and 0.292, respectively, by fitting the power law (Equation 1) to the tensile data at a strain-rate of 1 /sec. Equation 4 was now applied to determine the unique strain rate sensitivity (*m*) for each data point in Figure 69 resulting in a plot of the calculated strain rate sensitivity versus strain-rate. Figure 70a shows the calculated values of strain-rate sensitivity as well as a linear regression of the data that yields the constants $A=2.47\text{x}10^{-5}$ and $m_{quasistatic}=-0.0227$. Therefore, substituting the four constants (*K*, *n*, *A* and $m_{quasistatic}$) in Equation 3 yields the final constitutive model that describes AA5182 data by Higashi et al. [47] as follows:

$$\sigma = 538\bar{\varepsilon}^{0.292}\dot{\bar{\varepsilon}}^{(2.47x10^{-5}\dot{\bar{\varepsilon}}-0.0227)} \qquad (5)$$

Figure 69 shows the model predicted curves from the constitutive model (Equation 5) compared to the experimental results of Higashi et al. [47] over the strain-rates from 10^{-3} to ~$2.5\text{x}10^{3}$ /sec. The figure shows that the constitutive model is able to reasonably fit the experimental data across six orders of magnitude of strain-rate.

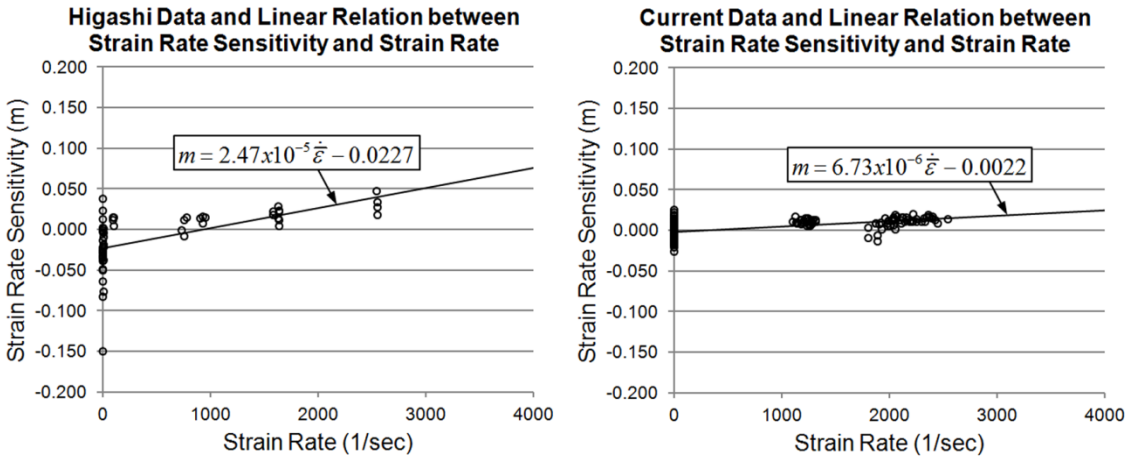

(a) (b)

Figure 70 - Calculated strain-rate sensitivity as a function of strain-rate for AA5182-O using modified power law constitutive model for (a) the data of Higashi et al. [47] (left) and, (b) the current work (right). This data is extracted at true strains of 0.05, 0.10, 0.15, and 0.20.

The applicability of the proposed model will now be further demonstrated on an AA5182-O sheet material (1 mm thick) that is more representative of automotive sheet material than the hot rolled plate (3 mm thick) used by Higashi et al. Tensile tests (as described above) were conducted at six nominal strain rates (10^{-3}/sec, 10^{-2}/sec, 10^{-1}/sec, 1000/sec, 2000/sec, and 2400/sec) and three samples each were tested along the rolling and transverse directions at each nominal strain-rate. Therefore, a total of 36 tensile tests were performed. Since no tests were conducted at a strain rate of 1 /sec, the second method (in Step 3) to determine *K* and *n* was used, where two reference flow stresses and strain rates were used to calculate *m* using $m = \log(\sigma_2 / \sigma_1) / \log(\dot{\varepsilon}_2 / \dot{\varepsilon}_1)$[7]. Using the average flow stress changes between strain-rates of 10^{-1}/sec and 10^{-2}/sec, the strain-rate sensitivity was estimated to be *m*=-0.005 at the reference strain-rate of $5x10^{-2}$ /sec. This permitted the calculation of *K*=560 and *n*=0.303 as the material constants describing the 1mm thick AA5182 sheet representing automotive sheet materials.

For each of the 36 tensile tests, discrete true stress-true strain data sets were extracted at true strains of 0.05, 0.1, 0.15, and 0.20. This resulted in a total of 144 discrete true stress-true strain data sets and correspondingly, 144 calculated strain rate sensitivity values shown in Figure 70b. The data in figure 70b also shows the results of the linear regression used to calculate the constants A=$6.73x10^{-6}$ and $m_{quasistatic}$=-0.0022. Therefore, substituting the values of *K* (560) and *n* (0.303) along with *A* ($6.73x10^{-6}$) and $m_{quasistatic}$ (-0.0022) into Equation 3 yields the final constitutive model to describe the AA5182-O material sheet evaluated in this work, as follows:

$$\sigma = 560\bar{\varepsilon}^{0.303}\dot{\bar{\varepsilon}}^{(6.73x10^{-6}\dot{\bar{\varepsilon}} - 0.0022)} \qquad (6)$$

Figure 71 compares the stress-strain curve predicted by the constitutive model in equation 6 with the experimental data, and shows that the proposed model reasonably describes the stress- strain behavior

of AA5182-O over six orders of magnitude change in the strain-rate. Figure 72 compares the experimental results and the model predicted flow stress across the entire strain-rate regime tested, and demonstrates good correlation between the two across the entire strain-rate regime tested.

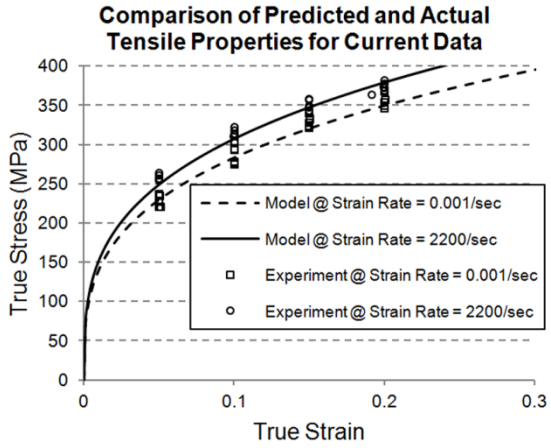

Figure 71 - Representative true stress versus true strain for the current AA5182-O alloy comparing the experimental results and the predictions of the modified power law constitutive model (Equation 6).

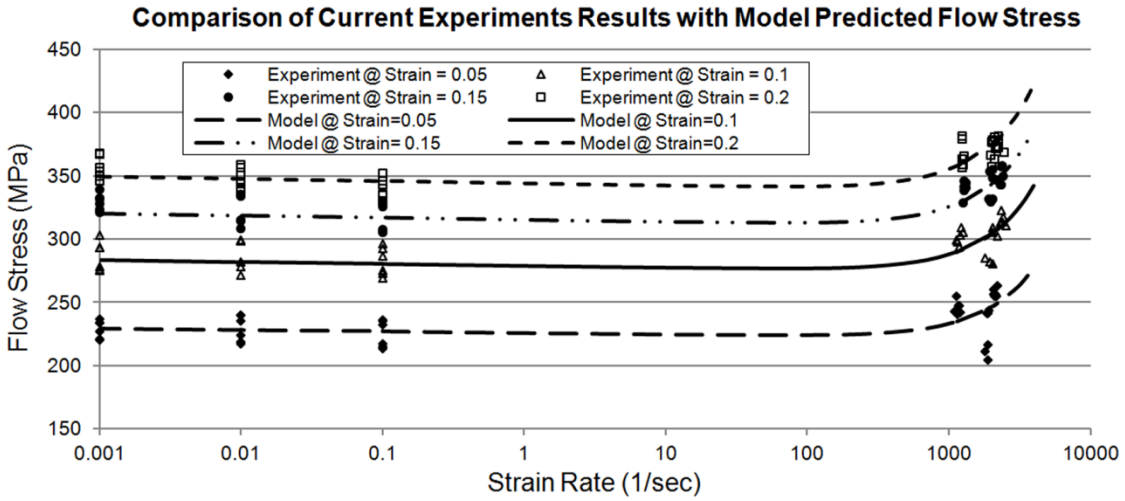

Figure 72 - The experimental flow stress data for the current AA5182-O alloy and its comparison with predictions of the modified power law constitutive model (Equation 6).

Although the material investigated by Higashi et al [47] and that used in this work were both AA5182 alloys, they demonstrate significantly different strain rate sensitivities across the $1x10^{-3}$/sec to $2.5x10^{3}$/sec strain-rate range. Specifically, the Higashi material shows more pronounced negative strain-rate sensitivity in the quasistatic regime and a more significant increase in strain-rate sensitivity with increasing strain-rate. In quantitative terms, the values of A and $m_{quasistatic}$ for Higashi et al. (figure 70a) are an order of magnitude greater than the Al tested in the present work (figure 70b). Generally, it is recognized that variations in chemistry, microstructure, etc. exist at some nominal level between different suppliers (or batches) of material, which may explain the differences in the strain-rate

sensitivities of the two populations of AA5182 material. However, such variations in materials may become increasingly significant if the materials experience varying strain-rates during automotive forming operations. For example, the strain-rate during electrohydraulic forming [7] may vary from quasistatic to $>10^3$/s and hence, two different sources of nominally the same alloy may show significant performance differences during automotive forming due to different constitutive relations at high, or highly variable, strain-rates.

Figures 70a and 70b show that the relative magnitude of the coefficients A and $m_{quasi\text{-}static}$ differ by an order of magnitude in Higashi's and the present work. However, the general trend for SRS is to be negative in the quasi-static regime, and positive with increasing strain-rate such that m > 0 for strain-rates > ~10^3/s. Using TEM, Higashi et al. [47] observed that a sample deformed continuously at 0.5 /s to a strain of 0.1 showed greater dislocation density than if the sample had been deformed incrementally – first at 0.5 /s to a strain of 0.04 and then at 10 /s to a final strain of 0.1. In essence, they explained negative SRS on the basis of dislocation density in the material, where dislocation density was greater at lower strain rate. Elsewhere in the literature, negative SRS in Al-Mg alloys under room-temperature quasi-static testing has been attributed to dynamic strain aging (DSA) [72, 73], whereby Mg solute atoms diffuse to the dislocations and impede their motion. Thus, Mg solute atoms raise the flow stress of an Al-Mg alloy under quasi-static testing, but are ineffective in pinning dislocations at increasing strain rates, which manifests as negative SRS. Under room-temperature quasi-static testing, Mukhopadhyay [73] reported almost identical values of SRS in equi-axed Al-Mg alloys: -0.01 and -0.02 for grain-sizes of 16 um and 26 um, respectively. Although Higashi et al. [47] didn't publish the grain-size, micrographs from their related publication [49] show a pancaked microstructure with grains elongated along the rolling direction with long dimension on the order of ~100 um. Despite the differences in the grain-size and morphology between [73] and [47, 49], the SRS values of [73] are similar to the $m_{quasistatic}$ of -0.0227 calculated in the present work for Higashi's [47, 49] material. By comparison, the present alloy has equi-axed grains with an average size of ~10 um (figure 73), with the $m_{quasistatic}$ being an order of magnitude lower (-0.0022) than that observed in [47, 49, 73,].

Based on a simple dislocation model developed by Barlat et al. [74] for aluminum alloys where the initial average dislocation mean free path is equated to the grain-size, the quasistatic SRS is indeed found to be negative with the value becoming increasingly negative with increasing grain-size. Although the qualitative conclusions from the model [74] may explain (to some extent) the differences in quasi-static SRS between [47, 49, 73] and the present work, other factors such as the presence of second phase particles, actual content of alloying elements (Mg, Mn, Si, Fe etc.), and texture may also play a role. For example, since DSA is attributed to the interactions of solute atoms with dislocations, all the alloying elements in solution may play a role (whereas alloying elements bound in precipitates will not affect DSA). Additionally, although Higashi et al. [47, 49] did not determine the texture of their material, the texture of their hot-rolled plate with pancaked grains is likely to be different from that of the sheet used in this work. In other words, for the same nominal chemistry, prior thermomechanical treatment may alter the relative availability of alloying elements in solution/precipitates as well as produce other microstructural differences that may result in different mechanical behavior. Nevertheless, the results

in figure 70 show that while the SRS may be influenced by various factors, the methodology developed in this work enables one to describe it adequately over a large range of strain-rates.

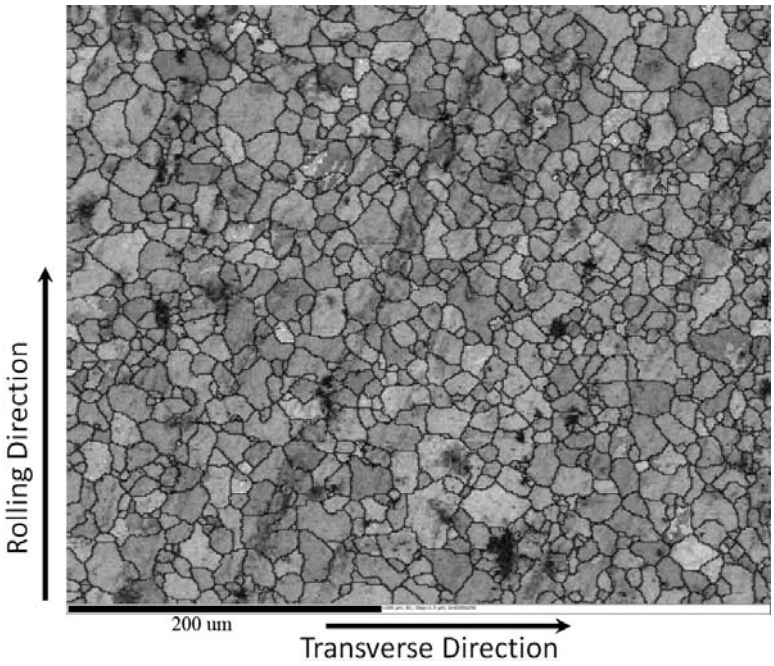

Figure 73 - Microstructure of the AA5182 alloy characterized in the current work.

5.4 Constitutive Model for DP600

The applicability of the proposed model will now be further demonstrated on DP600 sheet material (1 mm thick). Tensile tests were conducted at six nominal strain rates described above (10^{-3}/sec, 10^{-2}/sec, 10^{-1}/sec, 1000/sec, 2000/sec, and 2400/sec) and three samples each were tested along the rolling and transverse directions at each nominal strain-rate. Therefore, a total of 36 tensile tests were performed. Since no tests were conducted at a strain rate of 1 /sec, the second method (in Step 3) to determine *K* and *n* was used, where two reference flow stresses and strain rates were used to calculate *m* using $m = \log(\sigma_2 / \sigma_1) / \log(\dot{\varepsilon}_2 / \dot{\varepsilon}_1)$[71]. Using the average flow stress changes between strain-rates of 10^{-1}/sec and 10^{-2}/sec, the strain-rate sensitivity was estimated to be *m*=0.02 at the reference strain-rate of $5\text{x}10^{-2}$ /sec. This permitted the calculation of *K*=1000 and *n*=0.153 as the material constants describing the DP600 automotive sheet materials.

For each of the 36 tensile tests, discrete true stress-true strain data sets were extracted at true strains of 0.05, 0.1, 0.15, and 0.20. This resulted in a total of 144 discrete true stress-true strain data sets and correspondingly, 144 calculated strain rate sensitivity values shown in figure 74. The data in figure 74 also shows the results of the linear regression used to calculate the constants $A=8.12\text{x}10^{-7}$ and $m_{quasistatic}=0.01972$. Therefore, substituting the values of *K* (1000) and *n* (0.153) along with *A* ($8.12\text{x}10^{-7}$) and $m_{quasistatic}$ (0.01972) into Equation 3 yields the final constitutive model to describe the DP600 material used in this work, as follows:

$$\sigma = 1000\bar{\varepsilon}^{0.153}\dot{\bar{\varepsilon}}^{(8.12x10^{-7}\dot{\bar{\varepsilon}}+0.01972)} \quad (7)$$

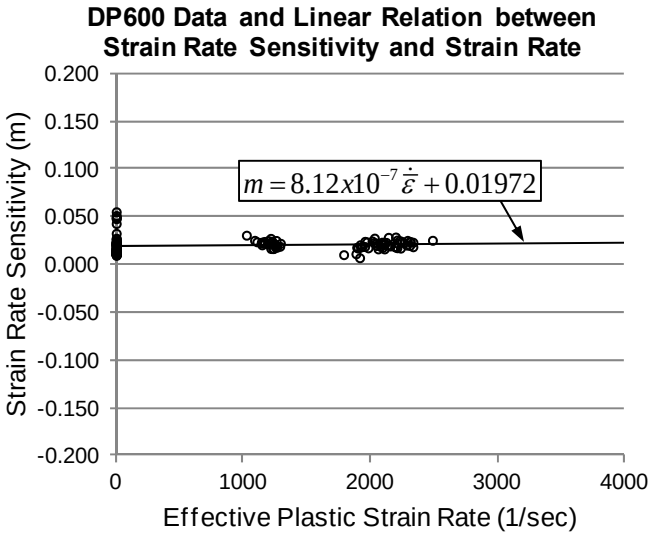

Figure 74 - Calculated strain-rate sensitivity as a function of strain-rate for DP600 using modified power law constitutive model.

Figure 75 compares the stress-strain curve predicted by the constitutive model in equation 7 with the experimental data, and shows that the proposed model reasonably describes the stress- strain behavior of DP600 over six orders of magnitude change in the strain-rate. Figure 76 compares experimental results and the model predicted flow stress across the entire strain-rate regime tested and demonstrates good correlation between the two across the entire strain-rate regime tested.

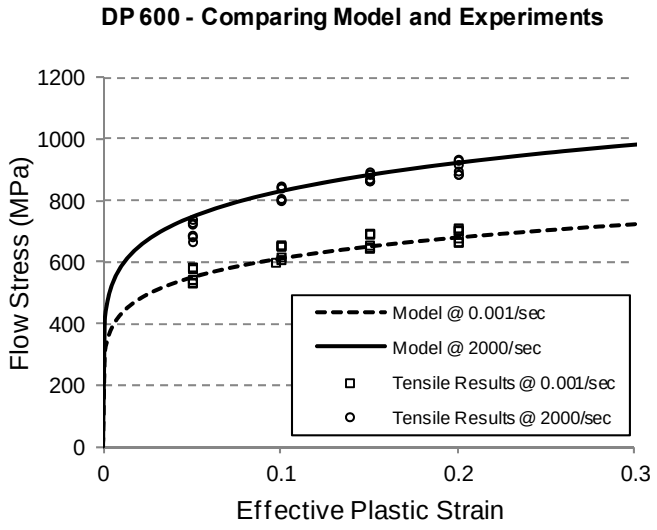

Figure 75 - Representative true stress versus true strain for DP600 comparing the experimental results and the predictions of the modified power law constitutive model (Equation 7).

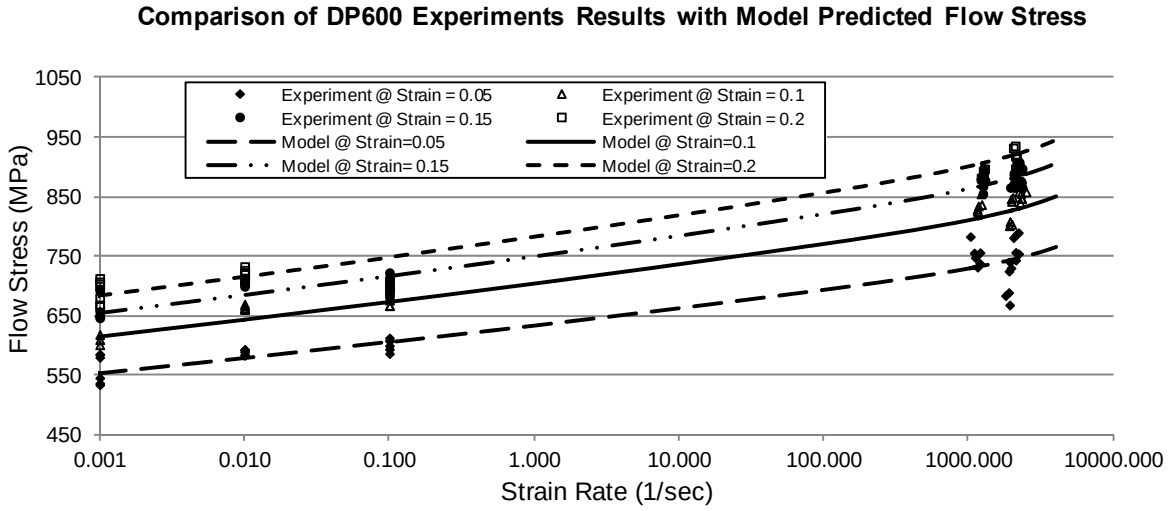

Figure 76 - The experimental flow stress data for DP600 and its comparison with predictions of the modified power law constitutive model (Equation 7).

The comparison of the constitutive model for the AA5182 and DP600 shows that the performance of the materials across the wide range of strain rates is quite different. Figure 77 compares the strain rate sensitivity of the materials across the strain rate range of interest. The figure shows that the DP600 has a positive SRS in the quasistatic regime, and the SRS remains relatively constant across the entire strain rate range. The positive SRS at quasistatic strain rates results in formability performance of the material being quite good (typically plane strain formability of 0.25-0.30 true strain) despite the fact that the strain hardening coefficient (n) is relatively low at n=0.153. In contrast, the AA5182-O material shows a negative SRS in the quasistatic regime, which limits the overall formability of the material despite the

relatively high strain hardening coefficient (n) at n=0.303. However, this situation changes significantly as the materials are evaluated at high strain rates. The DP600 has relatively constant strain rate sensitivity across the entire strain rate regime. However, the AA5182 material has an ever increasing SRS across the strain rate regime, and ultimately has a similar SRS as the DP600 material at strain rates approaching $3x10^3$/sec.

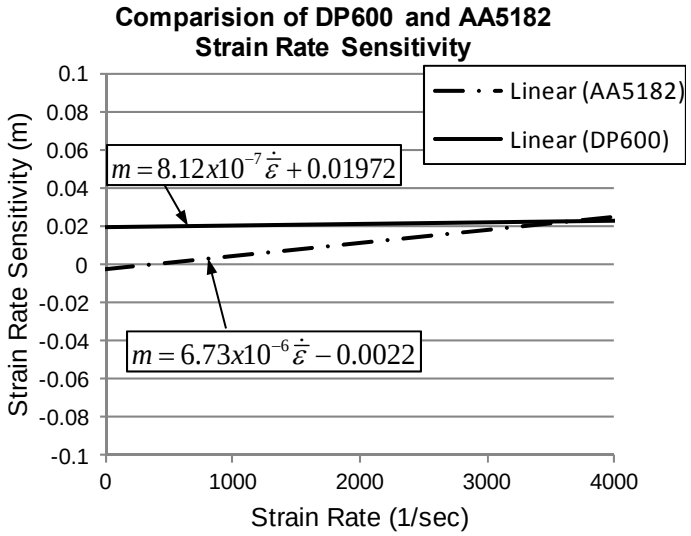

Figure 77 - Comparison of the calculated strain-rate sensitivity as a function of strain-rate for AA5182-O and DP600 using modified power law constitutive model.

Figure 78 shows the constitutive model predicted flow stress behavior of the two materials across the strain rate regime of primary interest for PPF. The DP600 materials have a relatively constant increase in the flow stress, while the AA5812 shows an increase when the strain rates approach and exceed 10^3/sec. Figure 79 further illustrates the differences in the materials across the strain rate regime. The figure again shows that the DP600 has a relatively constant flow stress increase, while the AA5182 has a rather little change in flow stress until the strain rates approach and exceed 10^3/sec. This significant difference in the changes in SRS across this strain rate regime has a profound influence on the predicted formability of the two materials during PPF, which will be shown and discussed in Chapter 6.

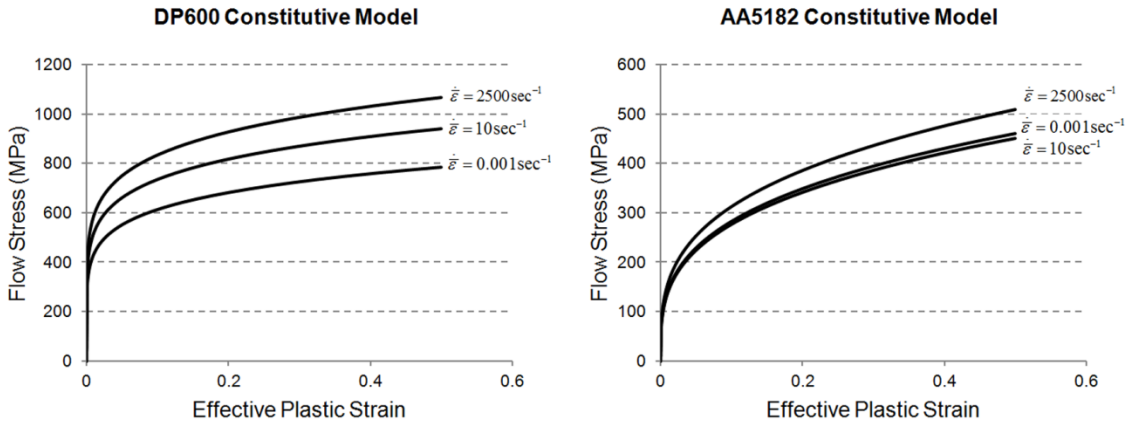

Figure 78 - Comparison of the constitutive model predicted flow stress for the DP600 and the AA5182-O

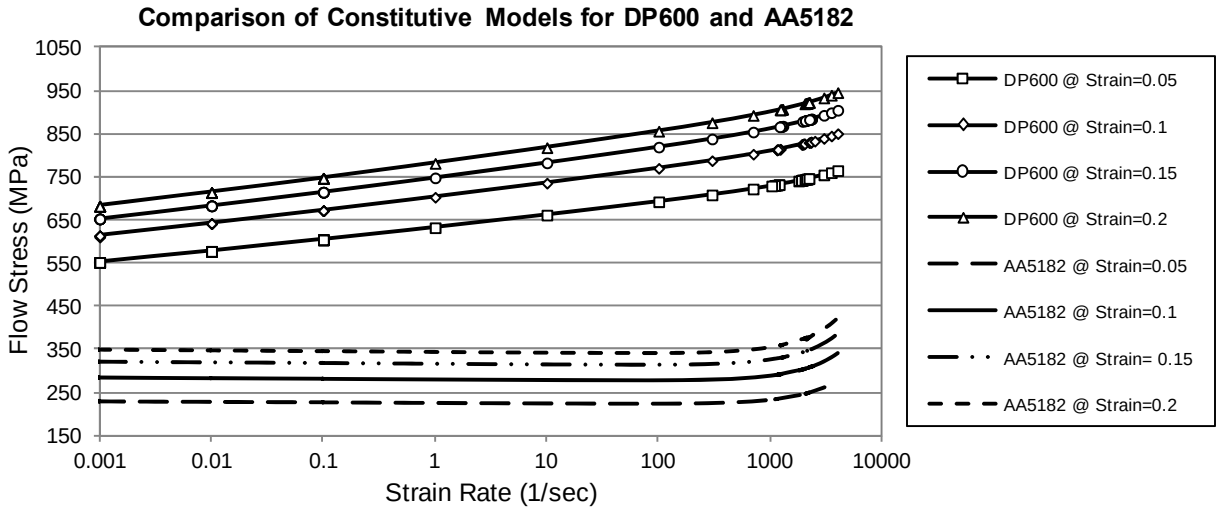

Figure 79 - Comparison of the constitutive model predicted flow stress for the DP600 and the AA5182-O.

The power law constitutive model was developed to treat SRS as a linear function of strain rate to enable the model to reasonably approximate the behavior of AA5182-O and DP600. This model retains the simplicity of the original power law equation, but improves the constitutive model's fit with the experimental data across a wide range of strain rates. This approach requires four constants to fit the constitutive model that can be determined through a simple array of uniaxial tensile tests, thus reducing the cost and complexity associated with more sophisticated constitutive models. For the for aluminum alloys, the constitutive model also appears to capture the well known effects of DSA at low strain rates [8, 9], and generally agrees with predicted increase in SRS shown by a simple dislocation dynamics model [11].

6 Formability Modeling of Metals during PPF

The work under Chapter 6 is designed to overcome the technical barrier that is the lack of validated and predictive formability models for PPF processes. The lack of full-field strain, strain rate, and deformation history during PPF makes validation of finite element models very difficult. Past work has focused on simple and reliable numerical models for PPF forming [12, 13, 14, and 37], but little validation opportunity is available with full-field deformation history. This work applies the Marciniak and Kuczynski (M-K) method of formability prediction to predict the formability of both aluminum alloy AA5182 and advanced high-strength steel alloy DP600 across a wide range of strain rates and strain rate directions [15]. The results of this work first validate the applicability and fitness of the M-K method to predict formability of sheet metals during pulse pressure forming. Furthermore, these models are used to parametrically evaluate the formability of the sheet metals across a wide range of strains, strain rates, and loading paths.

6.1 Approach to Modeling Formability

Many individual investigators have covered the calculation of theoretical forming limit diagrams. Many of these formulations are based on the concepts developed by Marciniak and Kuczynski (55), which is known as the M-K method. The M-K method hypothesizes the pre-existence of geometric imperfections inherent to all real sheet materials. They further propose that these geometric imperfections are the site of eventual localization and failure during the plastic deformation that is developed during biaxial stretching of a sheet. The concept of an initial imperfection in a sheet material is illustrated in figure 80, which shows the proposed imperfection (inhomogeneous) region and a homogenous region. The homogenous region thickness is considered dimensionally perfect.

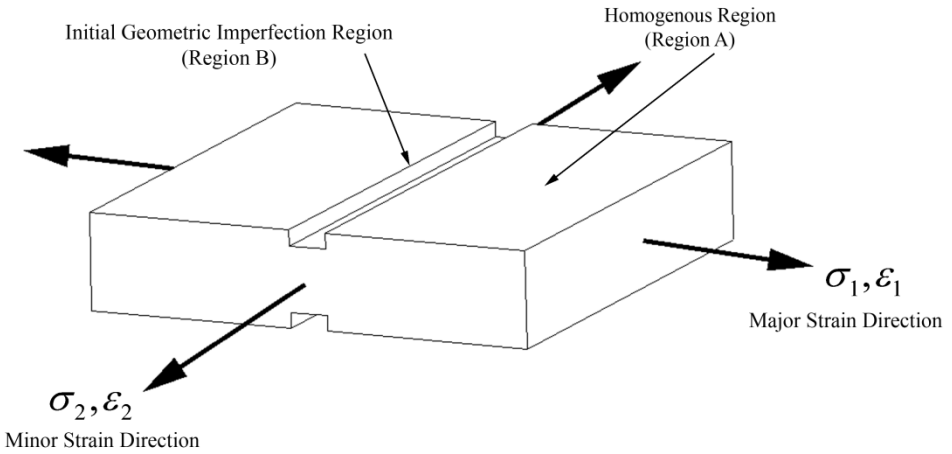

Figure 80 - Illustration of the concept of an initial geometric imperfection oriented perpendicular to the direction of major strain in a biaxial sheet stretching application.

Developing a forming limit diagram (FLD) based on the M-K method generally relies on numerically applying external load on the theoretical sheet shown in figure 80, and tracking the strains that develop during the numerical solution. The strains that theoretically develop in the imperfection and homogenous regions are dictated by the mechanical properties of the material being considered. The failure of the material under a specific simulated loading occurs when the imperfection region accumulates strain at a much higher rate than that of the homogeneous region (e.g. localization). The specific methods used to calculate the left and right hand sides of theoretical forming limit diagrams have been approached by different authors using slightly different methods. Therefore, the specific development of the left and right hand sides of the FLD will be reviewed separately. However, in the current work the constitutive law describing the material properties during deformation is common to both formulations. The constitutive law used in the current work is:

$$\sigma = K\bar{\varepsilon}^{n}\dot{\bar{\varepsilon}}^{m} \tag{8}$$

where K, n, and m represent a strength coefficient, strain hardening exponent, and strain rate sensitivity, respectively [70]. This is the general constitutive law and solution methods are developed based on this law. The strain rate sensitivity (SRS) of the materials is of critical interest during PPF, and the modified power law constitutive model will be applied from Chapter 5 to describe the materials. This overall approach to calculating the theoretical FLD has been recently published by Davies et al [10].

6.1.1 Left Hand Side FLD Calculations

The left hand side (LHS) of the FLD is the region that defines the formability under negative minor strains. Lian and Baudelet [75] first presented the method used in the current work to develop the theoretical FLDs on the LHS. Their formulation was based on the M-K method, observations made by Chan et al. [76], and the Hill instability criterion theory [77]. Lian and Baudelet developed a complete mathematical proof of the concept of material failure occurring in plane strain as a result of a 'critical thickness strain' being reached in the material. The solution to the problem of determining the LHS FLD reduces to tracking the development of an initial geometric thickness imperfection during plane strain deformation. The solution involves only the level of initial geometric imperfection, strain hardening coefficient, and strain rate sensitivity. The solution is notably unaffected by material anisotropy, and in the limiting case of zero initial geometric imperfection, the solution degrades to the Hill instability criterion that predicts a critical thickness strain of –n (strain hardening coefficient). The single equation used to establish the limit of formability in plane strain is:

$$fe^{\varepsilon_{3b}}\varepsilon_{3b}{}^{n}d\varepsilon_{3b}{}^{m} = e^{\varepsilon_{3a}}\varepsilon_{3a}{}^{n}d\varepsilon_{3a}{}^{m} \tag{9}$$

where ε_{3b} and ε_{3a} represents the thickness strain in the imperfection and homogeneous regions, respectively, and f represents the level of initial thickness imperfection in the material. A value of $f = 1$ represents no thickness imperfection, and a value of $f = 0.9$ represents a 10% initial geometric thickness imperfection in the subject material. Given a strain hardening exponent and an initial imperfection level, equation (9) may be numerically solved to develop a relation between the thickness strain in the imperfection and homogeneous regions. Localization and failure in the imperfection region is defined in the current work as the point where the model predicts that the rate of thickness strain accumulation in

the imperfection region is ten times larger than in the homogeneous region [78-80]. Given the critical thickness strain, and the assumption of constant material volume during deformation, values for the major and minor strains may be calculated to complete the left-hand side FLD.

6.1.2 Right Hand Side FLD Calculations

The theoretical calculation of the right hand side (RHS) of the forming limit diagram proves substantially more involved than calculating the left-hand side. There are several recent treatments of theoretically calculating the RHS FLD based on the M-K method using anisotropic yield criterion. However, this work is based upon the works presented by Graf and Hosford [78-80], and uses the Hosford high exponent yield criterion. Xu et al. [81] have presented similar methods based on the Hill 1993 yield criteria. Though the Hill 1993 yield criterion was not used in the current work, Xu et al. offer significant insight into the development of theoretical FLDs. The general outline of the solution procedure is presented below.

The basic concept for the development and solution of the FLD is based on the M-K method schematically represented in figure 80. The method of developing an FLD from the model in figure 80 is to numerically analyze the evolution of the initial geometric imperfection under applications of various plastic strain ratios. Upon application of a defined plastic strain to the overall subject sheet, the yield criterion and constitutive law are used to track the state of stress and the development of the imperfection region strains relative to the homogeneous region strains. By definition in the subject work, localization and failure occurred when the ratio of the rate of major strain accumulation in the imperfection to the homogeneous regions exceeded ten [78-81]. These calculations required several input equations and material parameters.

The yield criterion has proven to be a significant variable in the theoretical FLD calculations [78-81]. The Hosford yield criterion shown in equation (10) was exclusively used in the current work.

$$\sigma_1^a + \sigma_2^a + R(\sigma_1 - \sigma_2)^a = (R+1)\bar{\sigma}^a \qquad (10)$$

Where σ_1 and σ_2 are the biaxial stresses defined in figure 80, a and R are constants that are considered to be material properties, and $\bar{\sigma}$ is the effective yield strength of the material. The yield criterion is a high exponent version of the von Mises yield criterion, and in fact when a =2 and R=1, the criterion takes the form of the von Mises yield criterion. This yield criterion, together with the constitutive law and associated flow rule, are used to determine the RHS FLD (78-81).

6.1.3 Examples of Theoretical FLD calculations

In order to demonstrate results of a theoretical FLD calculation, and the impact of specific variables, a series of solutions were made that investigate the effect of varying the level of initial geometric imperfection (f), strain hardening exponent (n), and SRS (m). These types of calculations have been presented in previous work [78-81], and by others, and are presented here to illustrate the basic methodology prior to applying the methodology to PPF. Figure 81 illustrates a family of theoretical FLDs produced using values of a=8, R=0.7, n=0.25, and m=0 during the calculations. The figure illustrates the impact of introducing increasing levels of geometric imperfection to the subject sheet on the FLD.

The curve that represents an f = 0.995 is very near perfect, so its limit of formability is predictably high using the M-K method. In contrast, the curve which represents f = 0.95 has 95% of the original sheet in the imperfection region, and its limit of formability is predictably low. From figure 81, it can be seen that small changes in the level of imperfection may have relatively large impacts on the height of the FLD, especially as values of f approach unity.

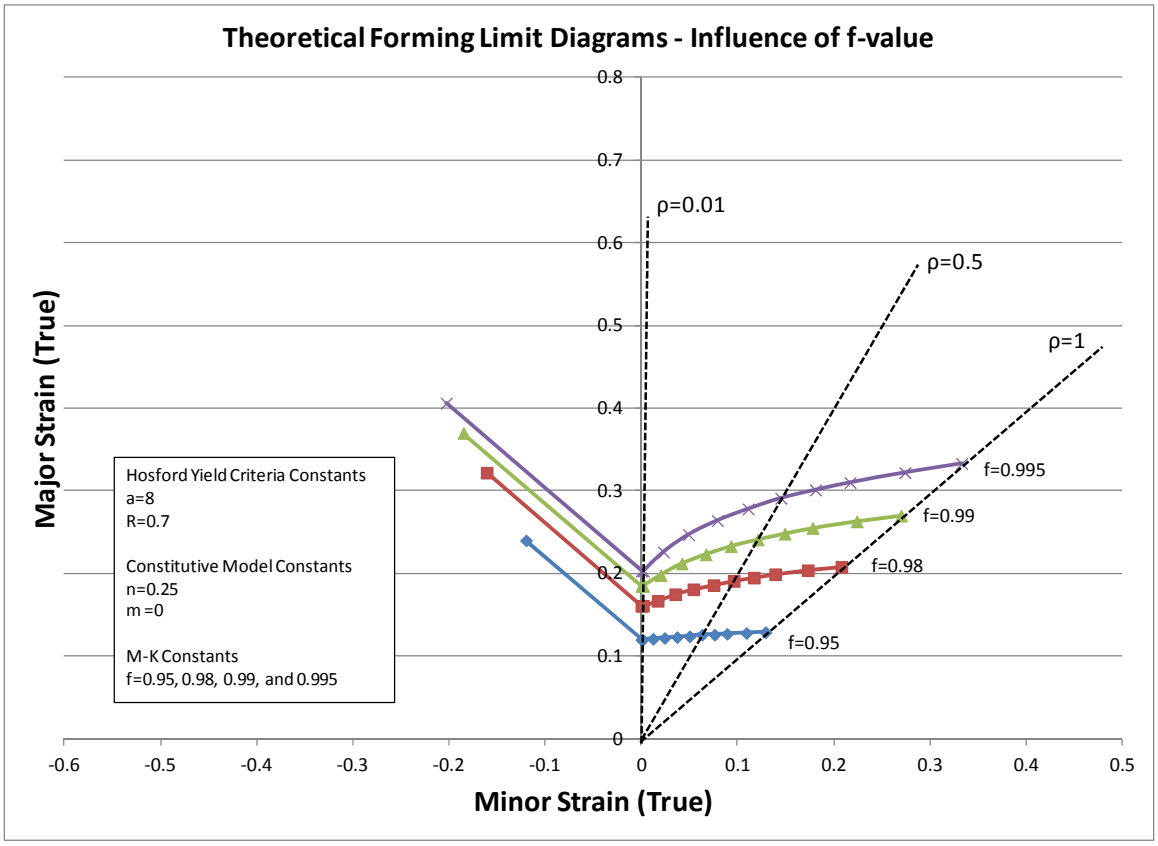

Figure 81 – Illustration of the influence of introducing increasing levels of geometric imperfection on the FLD.

Another important factor influencing the FLD is the strain-hardening exponent (n). Figure 82 shows a family of curves that illustrate the influence of varying values of strain hardening exponent on the FLD. The FLDs in figure 82 were calculated using values of a=8, R=0.7, f =0.99, and m=0. The figure illustrates the impact of introducing increasing strain hardening exponents for the subject sheet on the FLD. The curve that represents an n = 0.15 is very near the measured value for the DP600 material discussed in Chapter 5, where the formability would be expected to be relatively low using the M-K method if the material had a SRS of m=0. In contrast, the curve which represents n = 0.25 is more indicative of an aluminum alloy that does have a SRS of m=~0 in quasistatic forming conditions. From figure 82, it can be seen that small changes in the strain hardening exponent (n) may have relatively large impact on the height of the FLD.

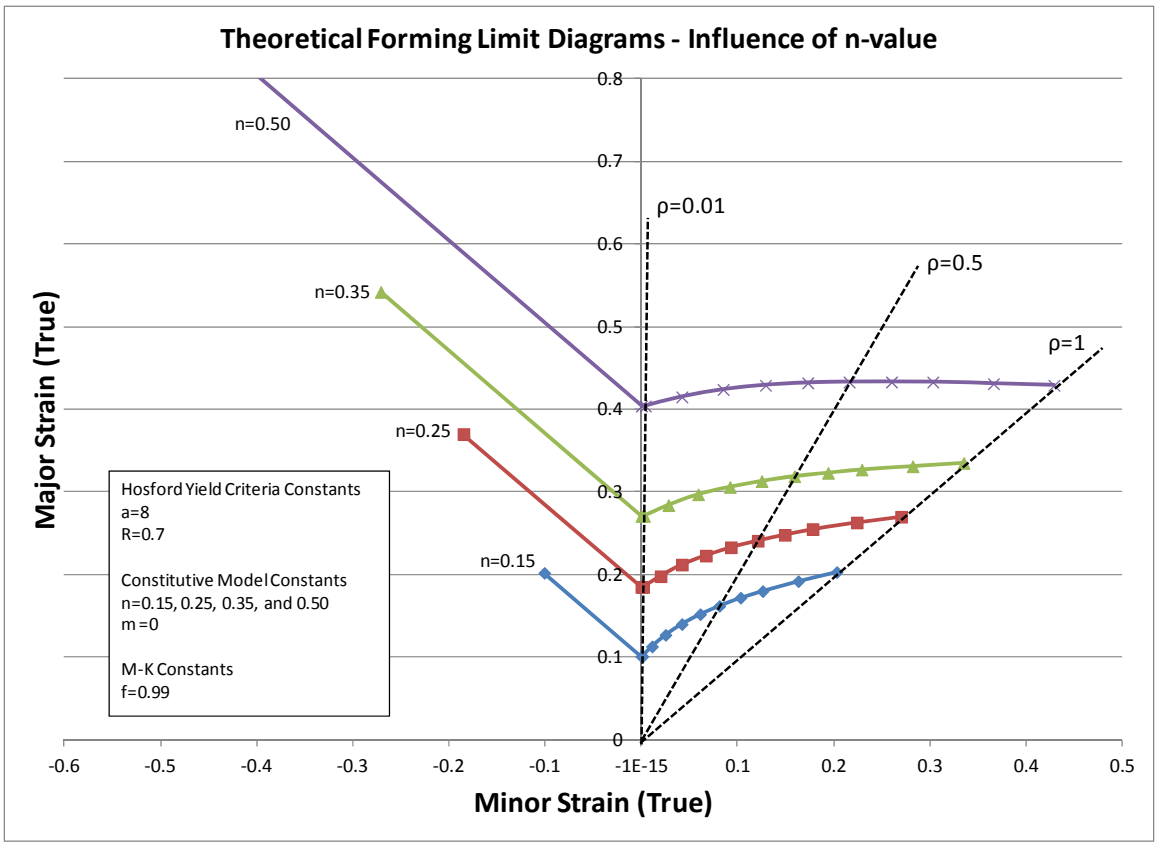

Figure 82 -Illustration of the influence of introducing increasing strain hardening (n) on the FLD.

The influence of strain rate sensitivity is a critical component of materials formability. Figure 83 shows the influence of relatively small changes in the SRS of the material. The FLDs in figure 83 were calculated using values of a=8, R=0.7, *f* =0.99, and n=0.25. The figure illustrates the impact of introducing increasing SRS for a subject sheet on the FLD. The figure shows that having an SRS value of m=0.02 versus m=0 can shift the FLD by a true strain of 0.1, or approximately 50% in the given case. The AA5182-O and DP600 materials described in Chapter 5 have highly variable SRS. There SRS at quasistatic strain rates are separated by approximately 0.2, but are nearly the same value (m=~0.2) at strain rates approaching 10^3/sec. Therefore, the importance of having the constitutive model accurately describe the SRS of the materials during the dynamic forming event of PPF is critical to accurately describing the formability of the materials.

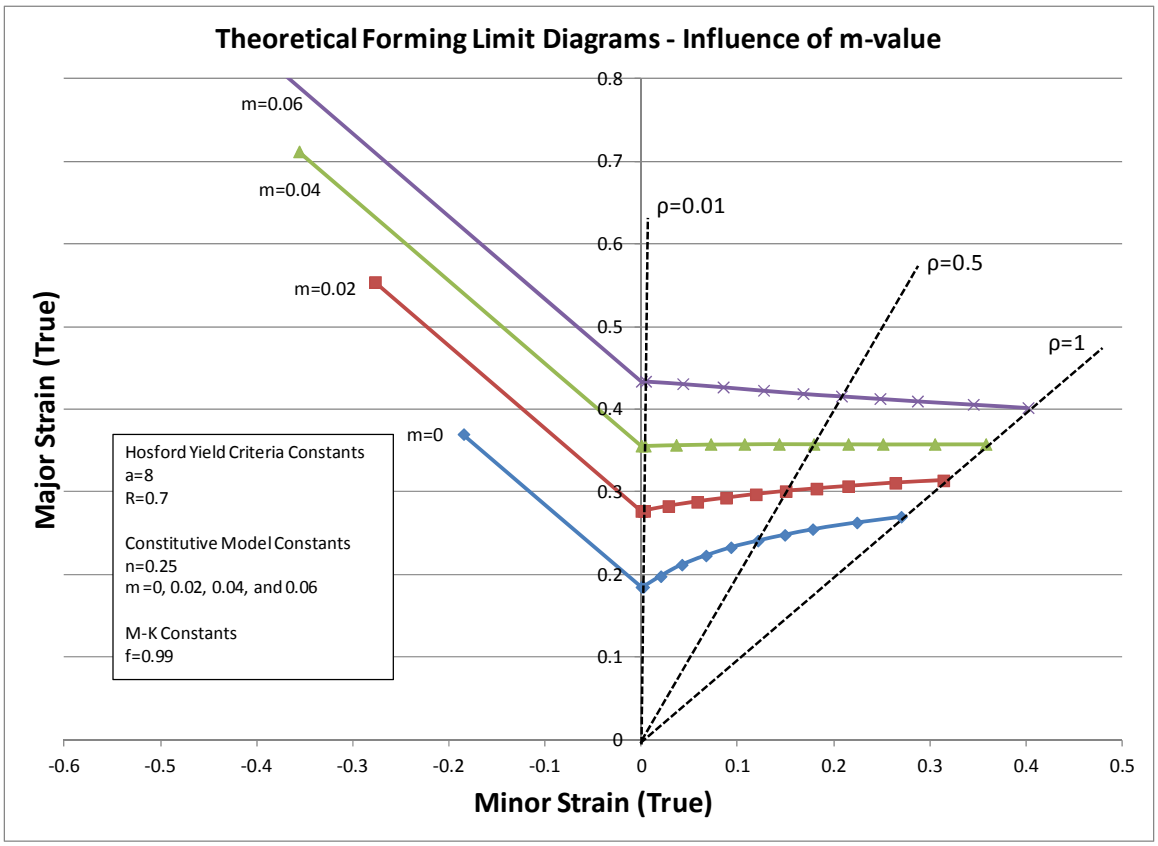

Figure 83 -Illustration of the influence of introducing increasing strain rate sensitivity (m) on the FLD.

In combination, figures 81, 82, and 83 represent a small amount of the overall potential complexity that exists during development of theoretical FLDs. The theoretical calculation of FLDs is a powerful tool to predict sheet metal formability given simple mechanical testing results. The method presents an opportunity to predict the formability of sheet metal during biaxial stretching at high strain rates.

6.2 Formability Model Validation

Validating the accuracy of the theoretical FLD formulation is critical to reliable application of the method. This validation will apply the constitutive models in Chapter 5 to the theoretical FLD approach in Chapter 6.1, and show that in combination they accurately describe the formability of the materials that were measured in Chapter 4.4.

The validation begins by selecting an experiment from Chapter 4.4 that exhibited elevated formability during free forming. The specimen selected is T-74, which is shown in figures 59, 60, and 61 in Chapter 4.4. This particular specimen achieved a peak true strain rate of 1.8×10^3/sec during forming. In analyzing the experiments, the material was also assumed to have constant volume during deformation, which yields the equation (11).

$$\varepsilon_1 + \varepsilon_2 + \varepsilon_3 = 0 \qquad (11)$$

The effective plastic strain was calculated using equation (12).

$$\bar{\varepsilon} = \sqrt{\frac{2}{3}\left(\varepsilon_1^2 + \varepsilon_2^2 + \varepsilon_3^2\right)} \qquad (12)$$

The effective plastic strain rate was determined by differentiating equation (13) with respect to time, and yielding the relationship shown in equation (13).

$$\dot{\bar{\varepsilon}} = \frac{2}{3\bar{\varepsilon}}\left(\varepsilon_1\dot{\varepsilon}_1 + \varepsilon_2\dot{\varepsilon}_2 + \varepsilon_3\dot{\varepsilon}_3\right) \qquad (13)$$

Applying equations 12 and 13 has limitations, as these equations assume the material is undergoing isotropic hardening and proportional loading during deformation. The experiments are approximately proportional loading, and the constitutive model describing the materials assumes isotropic hardening. These equations are used in combination to calculate the effective plastic strain rate and effective plastic strain from the experimental data obtained from the DIC system.

Figure 84 shows the experimental data for the effective plastic strain rate versus effective plastic strain during the experiments, as well as a polynomial curve fit to the data for a continuous representation of the experimental data. This data was directly observed by the high speed cameras and the Digital Image Correlation (DIC) system in the region immediately next to the initiated failure as shown in figure 60.

The next step in validation is applying the previously developed constitutive model for this aluminum alloy (equation 6 from Chapter 5.3). The constitutive model allows the instantaneous calculation of the flow stress in the material as a result of the strain rate from figure 84. Figure 85 shows the predicted flow stress for the material as a function of plastic strain during the high rate forming event, and compares it to the flow stress of the constitutive model at a strain rate of unity. This figure shows that the instantaneous flow stress becomes elevated at high strain rate due to the high strain rate sensitivity of aluminum above 10^3/sec. Figure 86 shows the instantaneous strain rate sensitivity of the materials during the forming event.

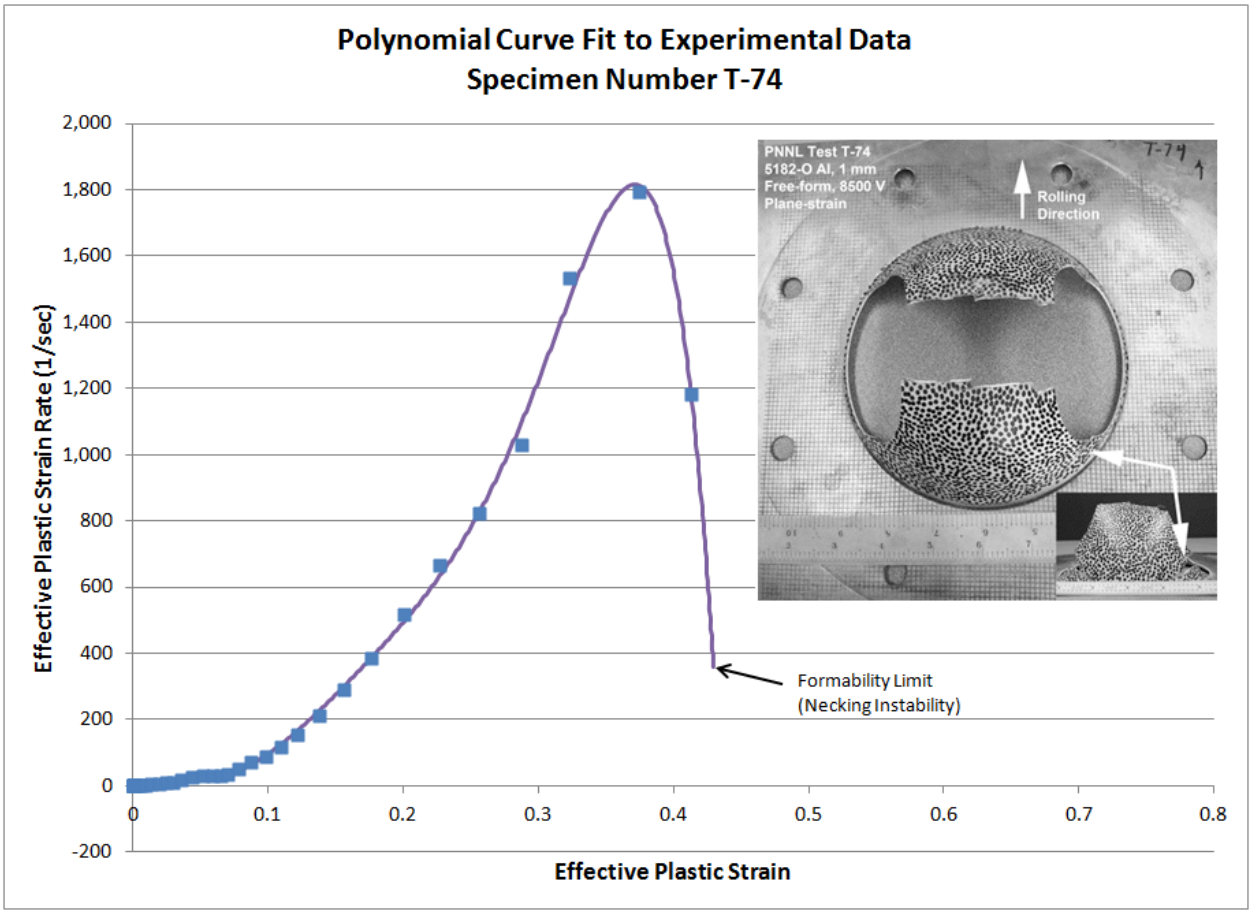

Figure 84 - Experimental strain rate versus strain data from an AA5182-O (1mm) EHF test that exhibited high formability, and a curve fit of a polynomial to describe the data.

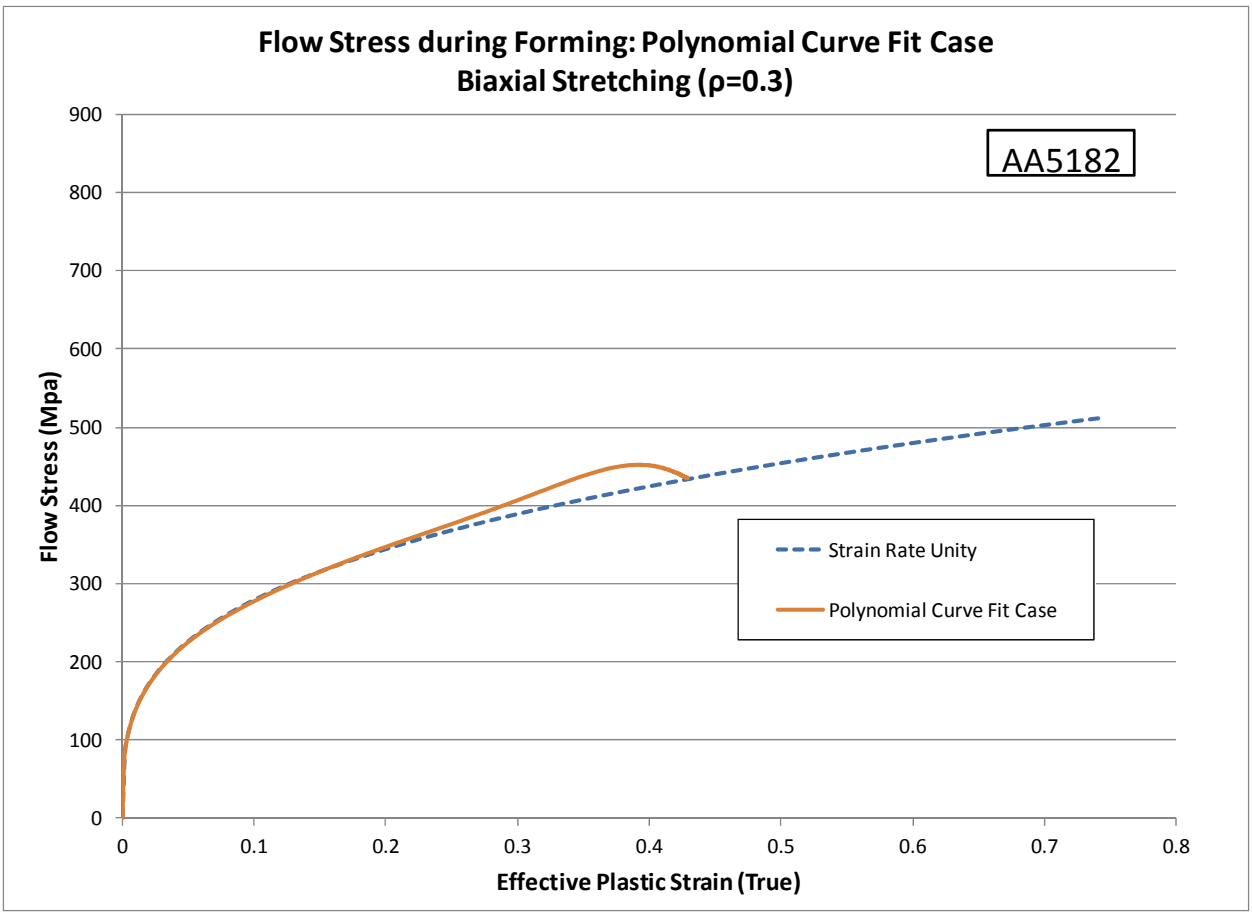

Figure 85 - Model predicted flow stress as a function plastic strain during the dynamic forming event shown in figure 84.

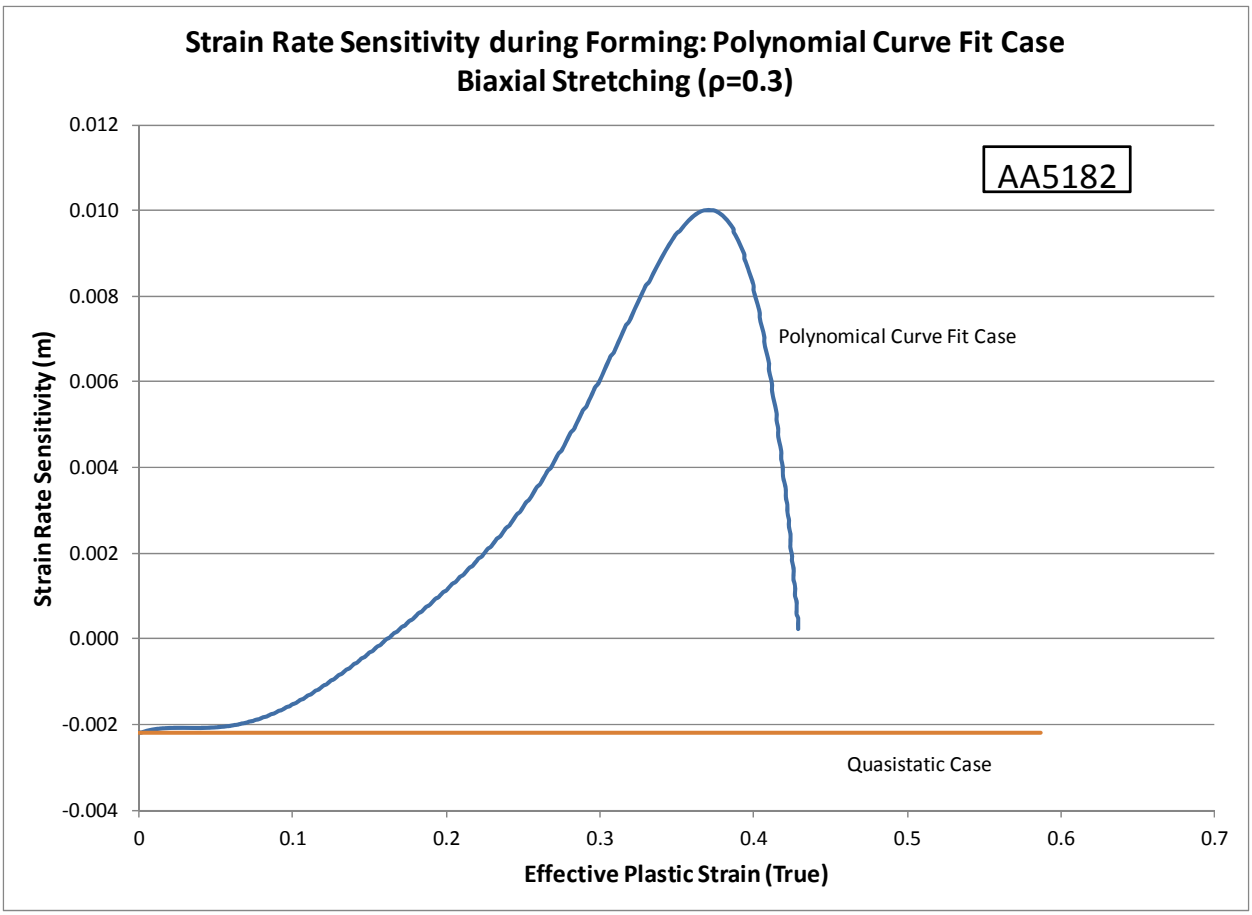

Figure 86 - Model predicted instantaneous strain rate sensitivity as a function plastic strain during the dynamic forming event shown in figure 84

The relatively high strain rate sensitivity of the materials during the forming event has a profound influence of the theoretical FLD of the material during the forming event. The theoretical FLD approach in Chapter 6.1 can now be applied to predict the FLD for this AA5182-O material subjected to the experimental conditions described in figure 84. Figure 87 shows the theoretical FLD calculated for this forming event, which shows a predicted plane strain forming limit (FLD_0) of ~0.3 true strain, as well as the general shape of the FLD. Interestingly, the theoretical FLD calculations show that the specimen would not have failed in biaxial stretching. In fact, the prediction shows that specimen localization and failure would not have occurred in the strain ratio ($\rho=\varepsilon_{minor}/\varepsilon_{major}$) between 0.3 and 1.0. The forming event would have effectively concluded prior to the localization and failure of the material in these strain ratios.

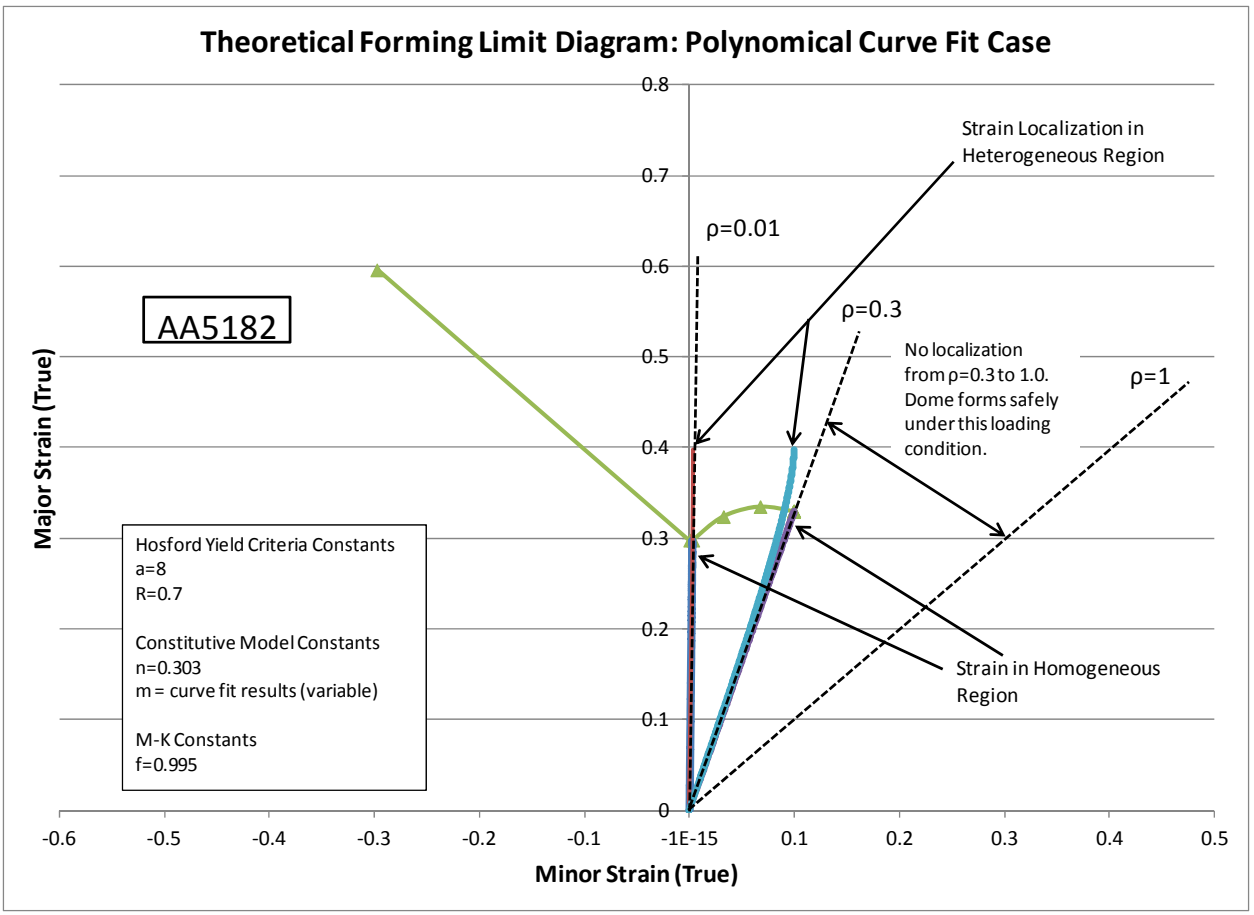

Figure 87 - Theoretical FLD for the AA5182-O materials subjected to the forming event characterized in figure 84.

The approach to validation is to compare this theoretically determined FLD to the experimentally determined FLD in Chapter 4.4. Figure 88 shows the results of this comparison between the incipient neck and safe experimental data (from specimen T-74) and the theoretical FLD developed and shown in figure 87. The results show that the theoretical FLD very closely approximates the experimental data, and differentiates the incipient neck data from the safe forming data very accurately. This figure validates that the application of the M-K method and that the modified power law constitutive model is capable of describing the formability of the sheet metal under high rate forming conditions such as PPF. Given this validation, the remainder of this work will parametrically analyze the formability of AA5182-O and DP600 alloys under various strain rate and strain paths during forming.

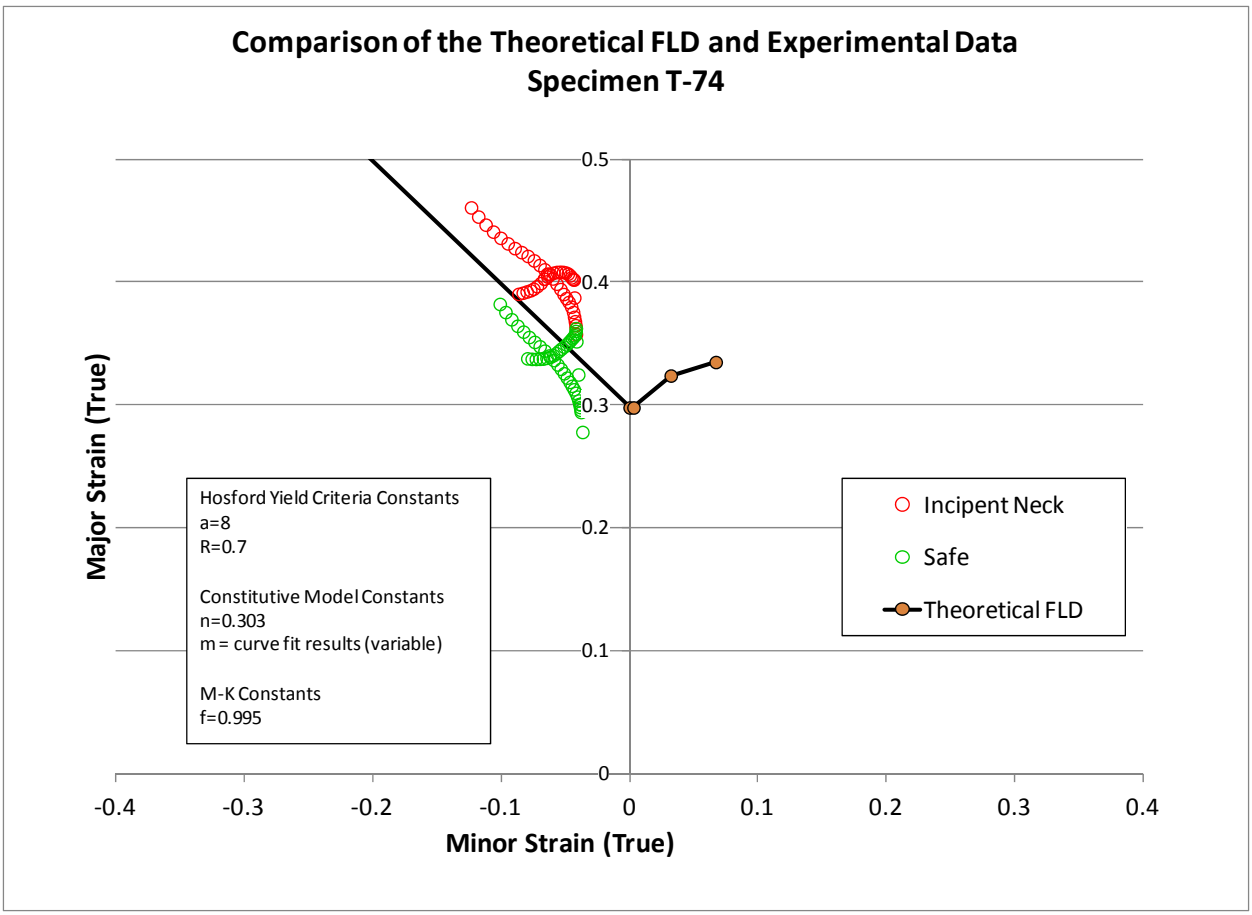

Figure 88 – Comparison of the experimental data to the theoretical FLD for the AA5182-O subjected to the forming event characterized in figure 84.

6.3 Parametric Analysis of Formability during PPF

The relationship between the effective plastic strain rate and the effective plastic strain during forming is the critical element of enhanced formability during PPF. In effect, the accumulation of plastic strain at higher strain rates results in the metal forming occurring under conditions of higher SRS (m) of the material. The higher SRS helps avoid material localization and results in higher FLDs. The key to successful PPF is maintaining high enough strain rates during the forming event to achieve the needed formability to make an automotive component. Therefore, the shape of curve defining the effective plastic strain rate and the effective plastic strain during forming will differentiate the FLD.

For the first set of parametric analysis, the relation between strain and strain rate will be assumed to follow a half-wave sinusoidal relationship such that the forming event starts at zero strain rate and ends at zero strain rate. The relationship between strain rate and strain is given by equation (14).

$$\dot{\bar{\varepsilon}} = \dot{\bar{\varepsilon}}_{peak} \sin\left(\frac{\bar{\varepsilon}}{\bar{\varepsilon}_{peak}}\pi\right) \qquad (14)$$

where the $\dot{\bar{\varepsilon}}_{peak}$ is the peak effective plastic strain rate of the material during the forming, and the strain rate is described as being sinusoidal during the forming event as a function of effective plastic strain.

Figure 89 shows five cases where different peak strain rates are assumed for five half-wave sinusoidal waveforms with the half-wavelength of 0.8 effective plastic true strain (Cases 1-5). The five cases have peak strain rates ranging from $4x10^2$/sec to 10^4/sec for Case 1 and Case 5, respectively. The purpose of this parametric study is to understand the influence of the peak strain rate on the expected material formability.

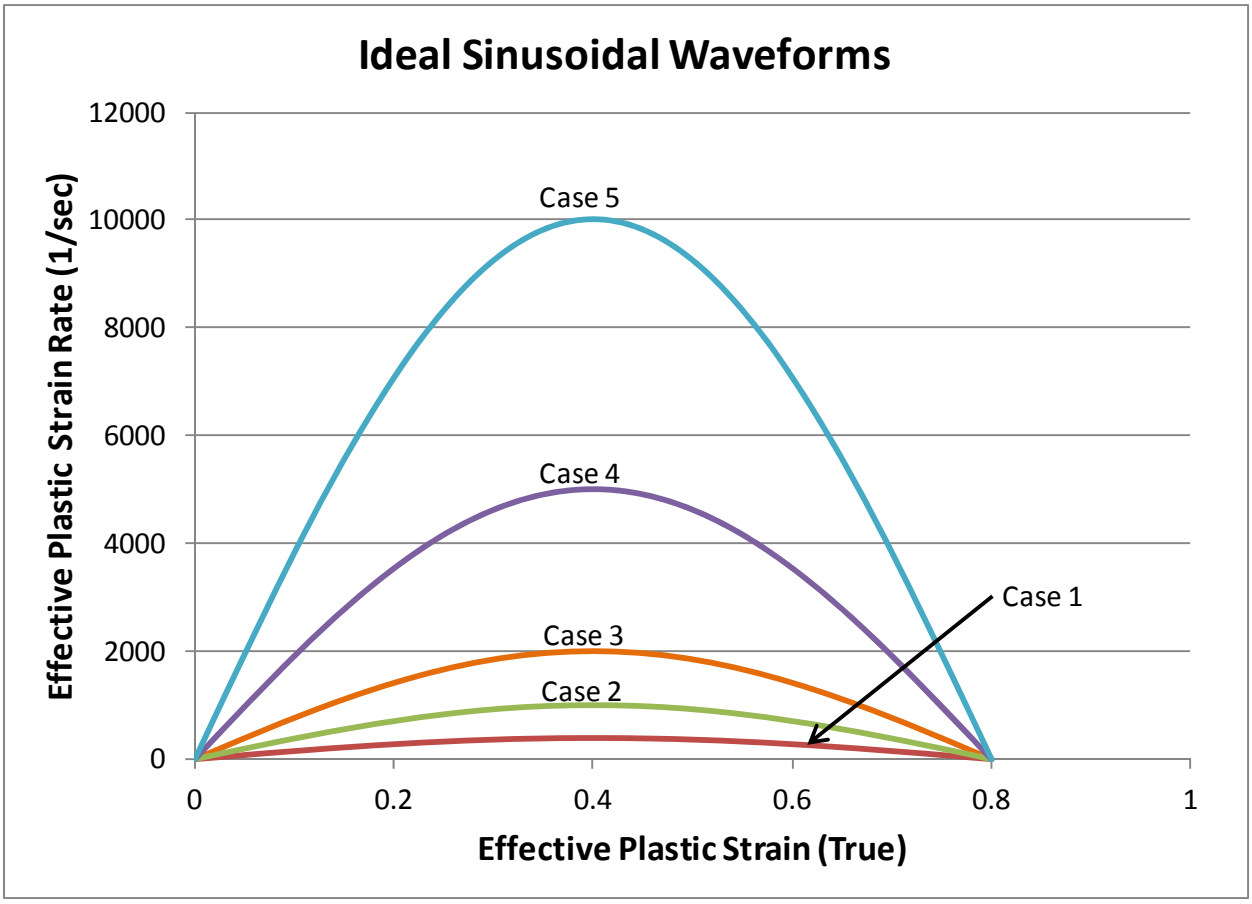

Figure 89 - Five cases of half-wave sinusoidal waveforms with difference peak strain rates assumed.

Each of these five cases was used to calculate the theoretical FLD for the AA5182-O sheet material. These five cases result in the constitutive model yielding five different responses given the modified power law. Figure 90 shows how the constitutive model yields significantly different SRS (m) for the materials for each of the five cases, and how each case exhibits the quasistatic SRS at the beginning of the event. However, due to the modified power law constitutive model, the SRS increases significantly with each increase in the peak strain rate for the material. The data in figure 90 was extracted from the theoretical FLD calculations, and the point at which each curve terminates is the results of localization

being predicted by the model. Furthermore, serrations in this SRS curve are a result of the numerical solver applied, and are simply a phenomenon from the solver - not a real variation. Figure 91 illustrates the changes in the instantaneous flow stress during the forming event. The figure shows that the increase in SRS during the forming event has a profound influence on the flow stress, which can cause the instantaneous flow stress to increase by more the 70% at strain rates of 10^4/sec compared to quasistatic flow stress.

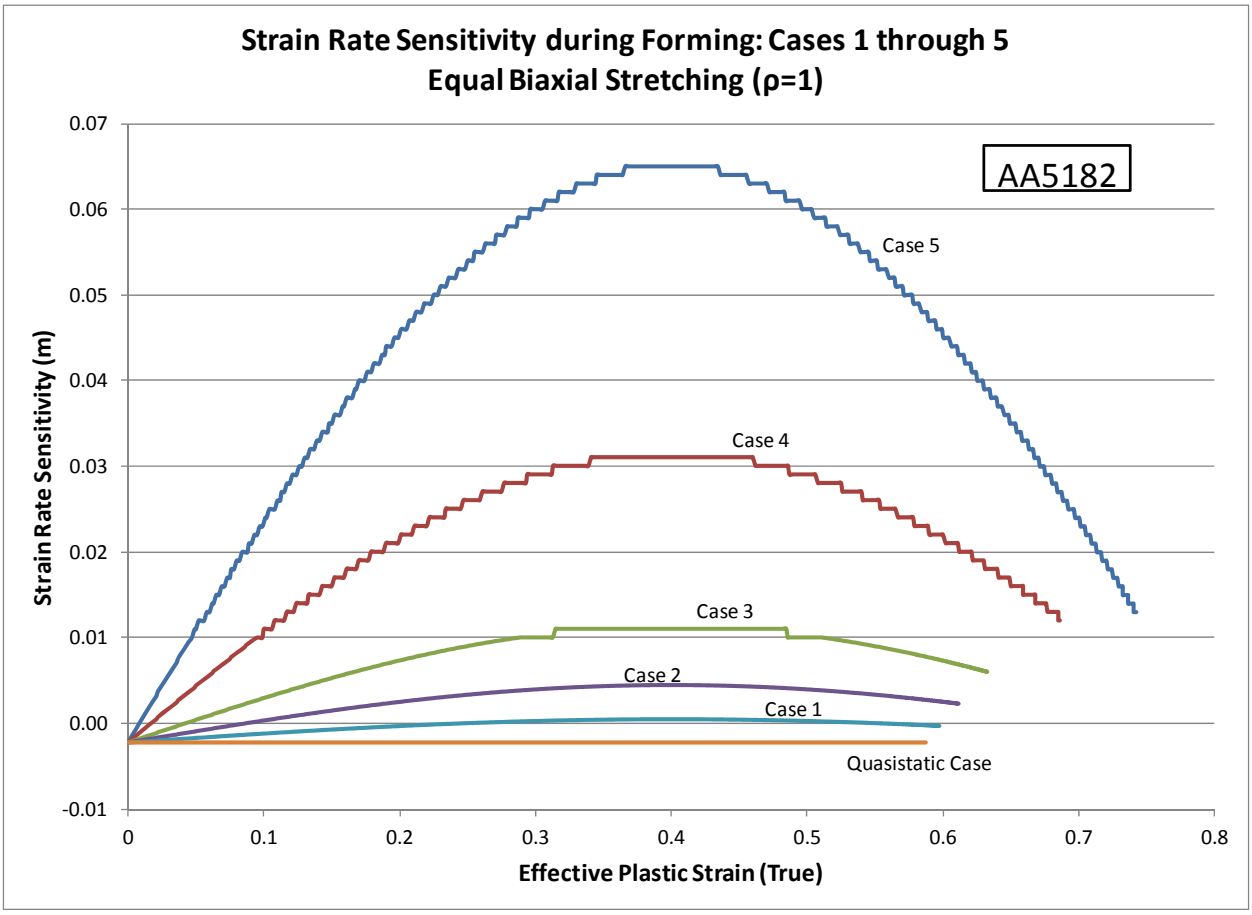

Figure 90 – Illustration of the instantaneous SRS (m) for the five cases of half-wave sinusoidal waveforms.

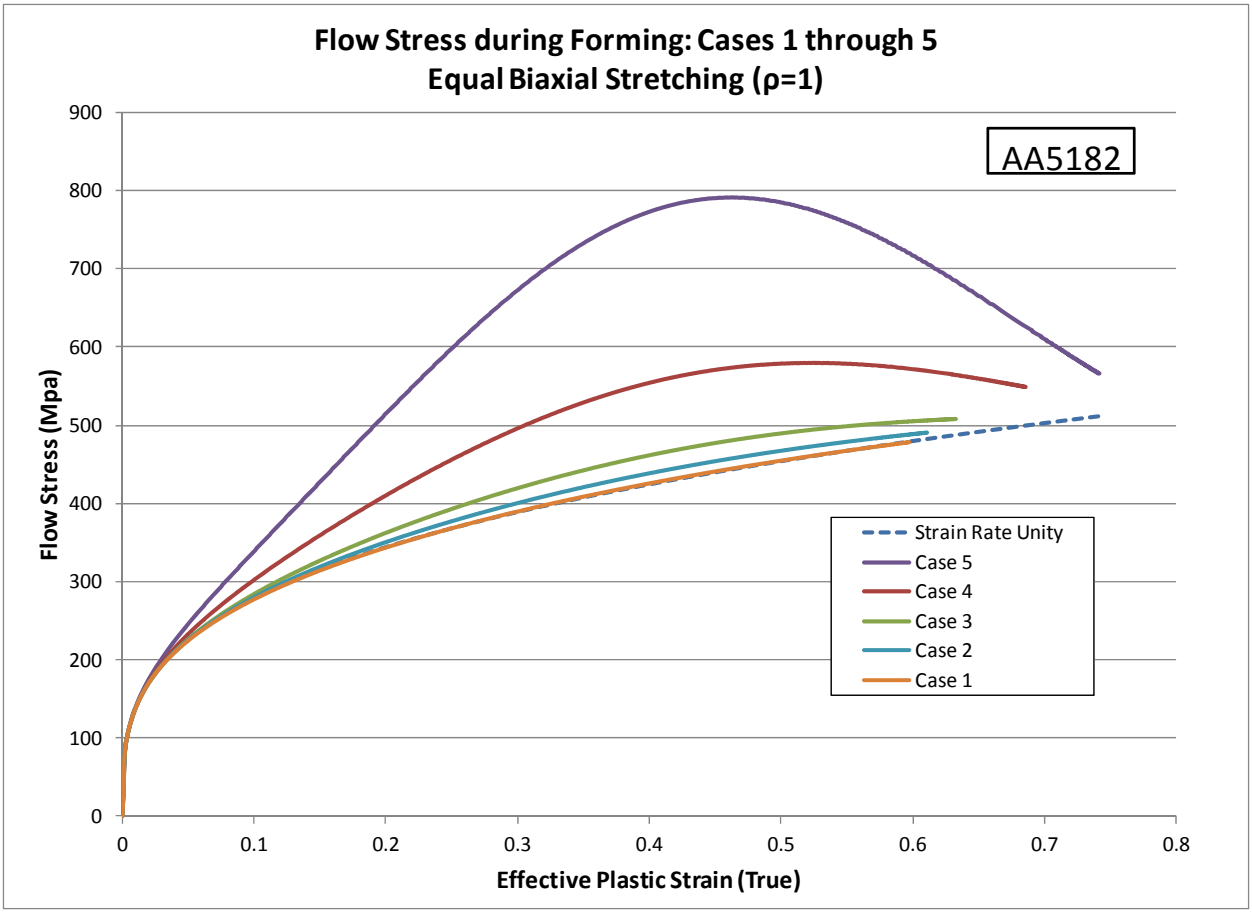

Figure 91 - Illustration of the instantaneous flow stress for the five cases of half-wave sinusoidal waveforms.

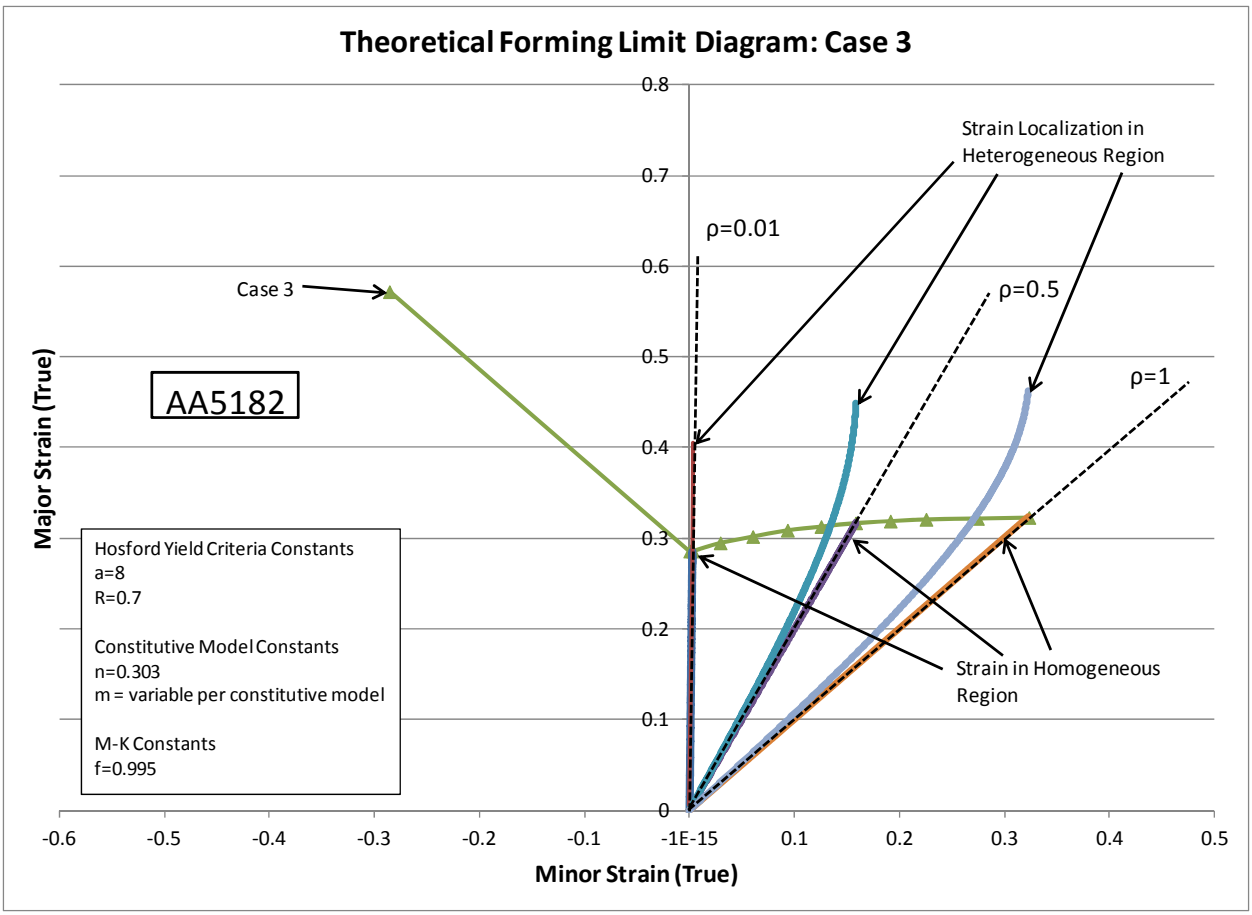

Figure 92 - Theoretical FLD for AA5182-O under Case 3 (peak strain rate =2x10^3/sec).

All five cases resulted in generation of a unique FLD curve for these given forming conditions. Figure 92 contains the FLD for Case 3, and an illustration of the accumulation of plastic strain in both the homogeneous and heterogeneous (imperfection) regions of the M-K method. The plane strain forming limit for Case 3 is approximately 0.28 in true strain. The figure also shows that the FLD has a conventional shape relative to the quasistatic FLD for AA5182-O aluminum alloy. Figure 93 contains the FLD for Case 5, and an illustration of the accumulation of plastic strain in both the homogeneous and heterogeneous (imperfection) regions of the M-K method. Case 5 shows a plane strain forming limit of approximately 0.50 in true strain. This is a major increase in formability for the material relative a quasistatic FLD.

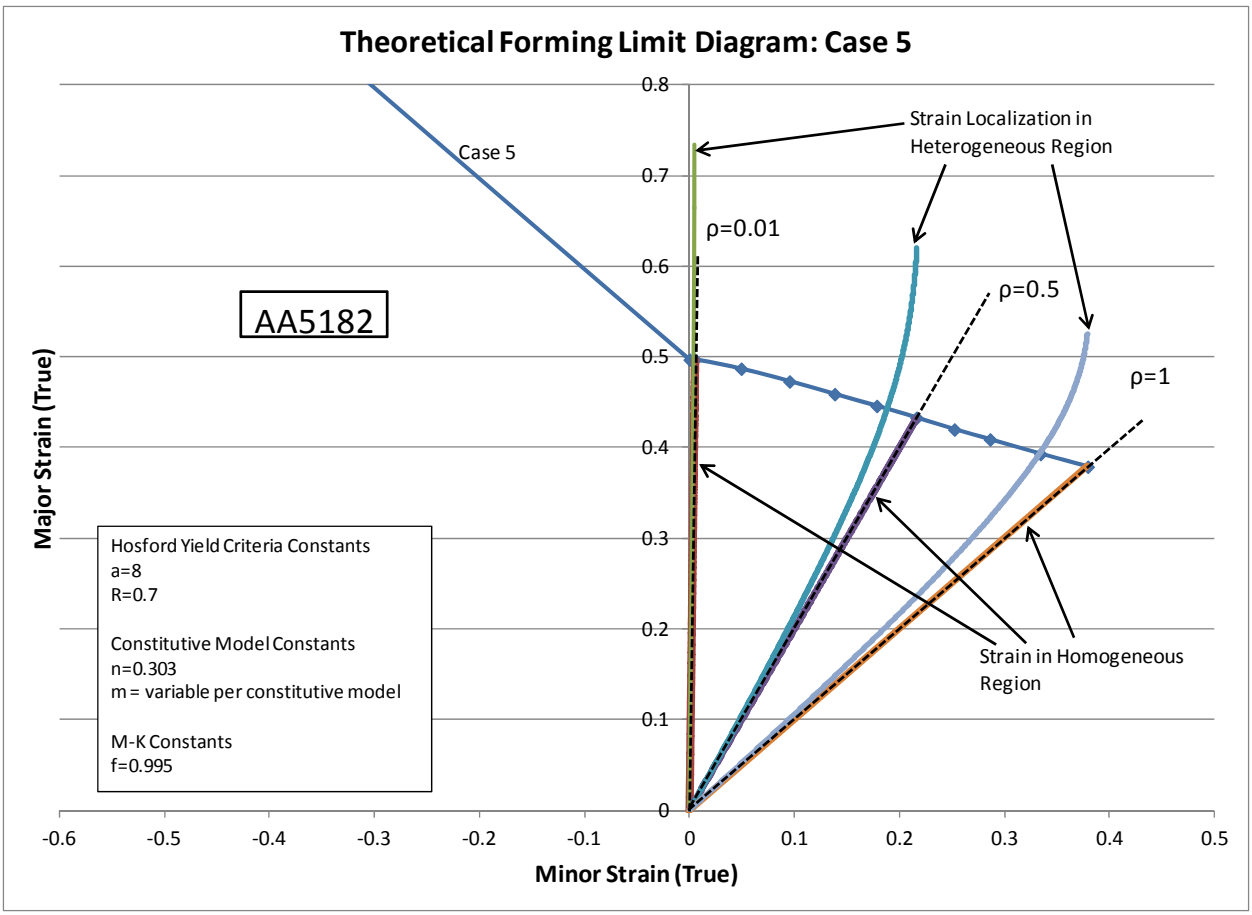

Figure 93 - Theoretical FLD for AA5182-O under Case 5 (peak strain rate =1x10^4/sec).

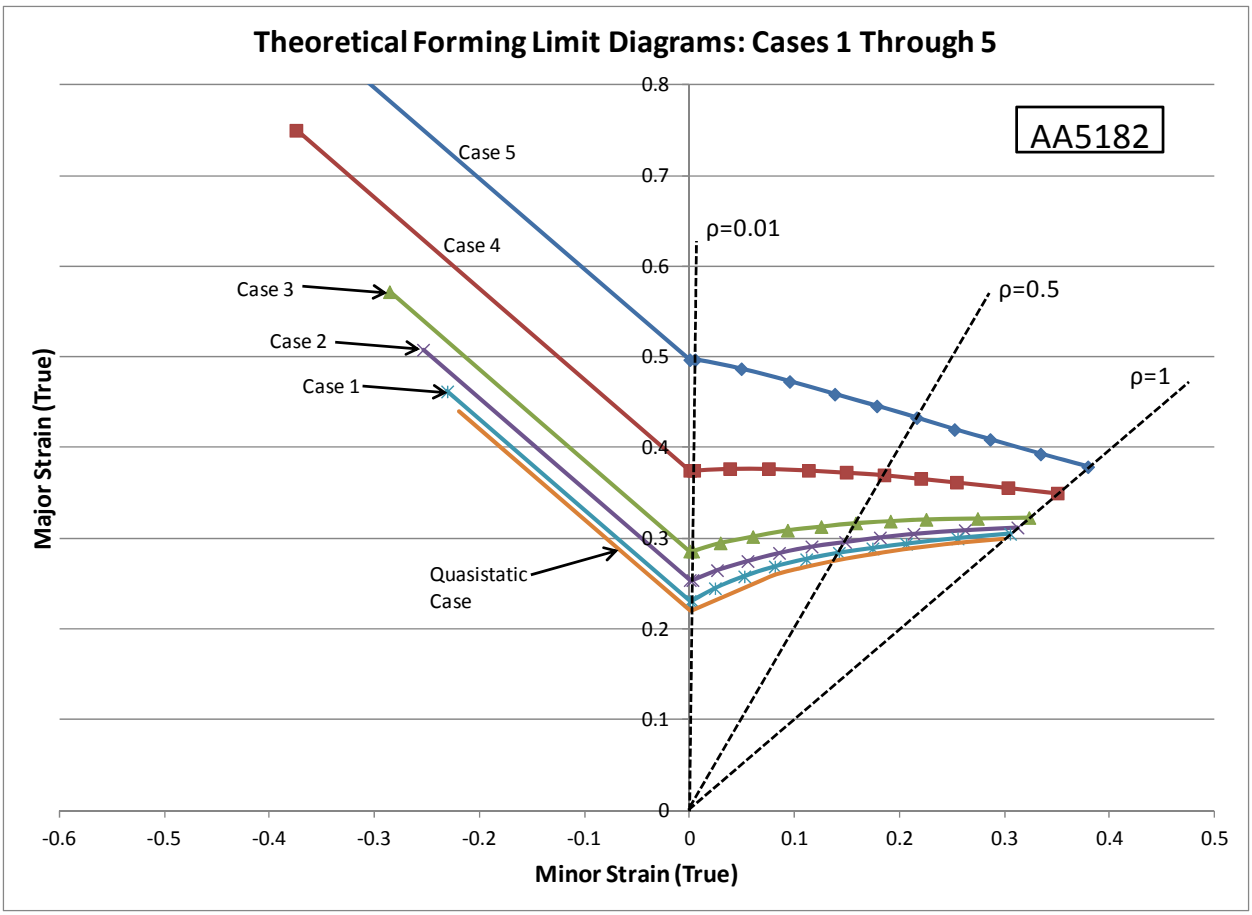

Figure 94 - Theoretical FLDs for AA5182-O across all five cases.

Figure 94 shows the family of theoretical FLDs for all five cases and the quasistatic FLD reference. The parametric analysis shows that the increase in formability is only modest until the peak strain rate reaches $1x10^3$/sec, where the influence of a substantially higher SRS causes a dramatic increase in the formability of the material. The formability appears to be very dependent on the actual strain rate achieved during forming. This fact may very well explain why different authors in the literature have reported large discrepancies in formability enhancement – from no improvement to 2-3 times improvement in the safe strains in the material. Therefore, any formability data for aluminum alloys should be accompanied by measured strain rates achieved during forming to be considered reliable indicators of the material performance.

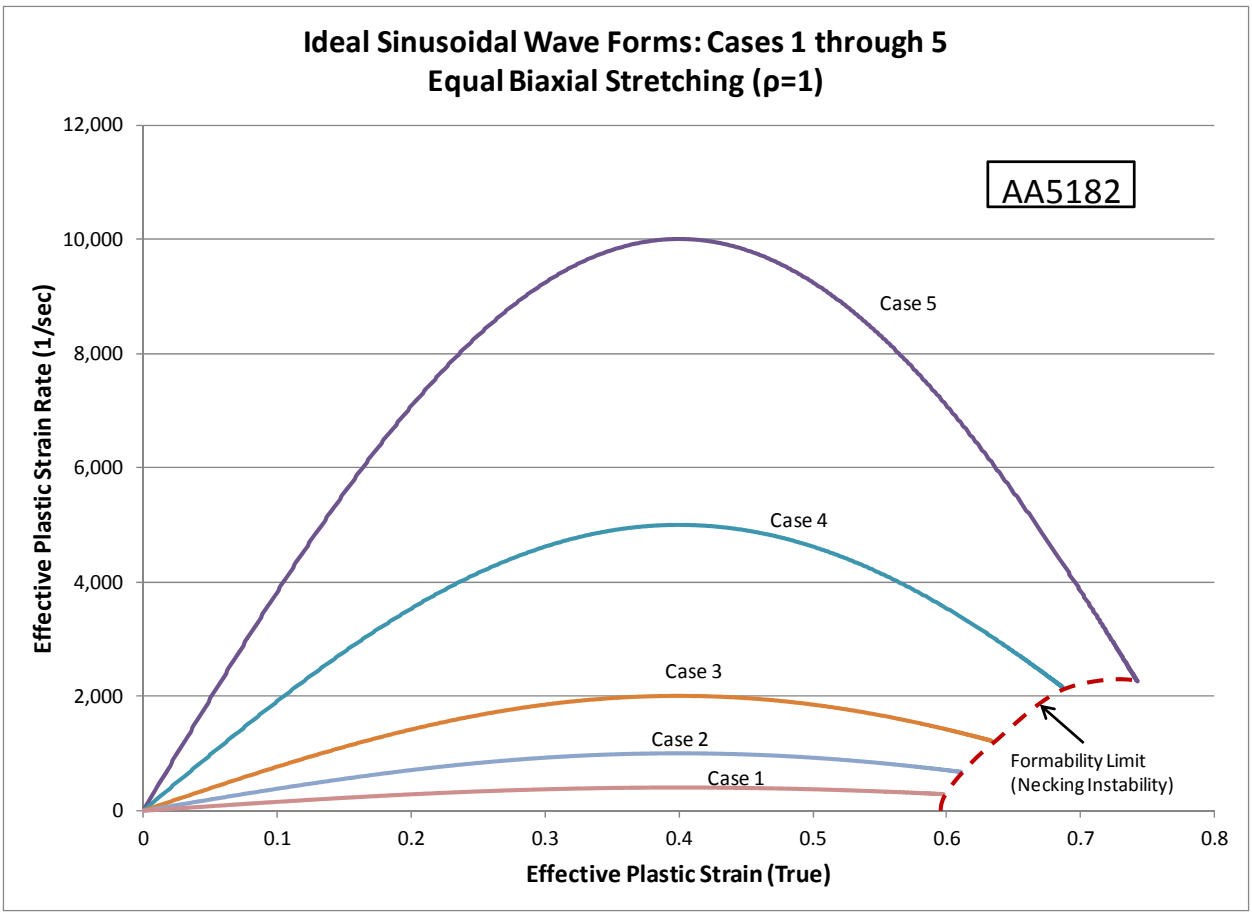

Figure 95 - Illustration of the forming limits of the material on the strain rate versus strain diagram in equal biaxial stretching (ρ=1).

Figure 95 shows the limits of material formability under equal biaxial stretching on the effective plastic strain rate versus effective plastic strain curve under equal biaxial stretching (ρ=1) conditions. The failure in this case occurs well after the peak strain rate has occurred, and effectively occurs during the deceleration of the forming part. The forming in Case 5 nearly achieved the end of the half-wave sinusoidal waveform. In all cases, the strain that was accumulating late in the forming event was at low strain rate. Moreover, as the peak strain rate increases, more plastic strain can be accumulated prior to the forming limit of the materials. Figure 96 and 97 show the limits of material formability under biaxial stretching (ρ=0.5) and plane strain (ρ=0.01) on the effective plastic strain rate versus effective plastic strain curve, respectively. These figures show that less plastic strain is accumulated as the forming event tends toward plane strain. Moreover, these figures show that the strain rate at material failure is very different for the three different loading directions (ρ=0.01, ρ=0.5, and ρ=1.0). This observation inspired the investigation of alternative waveforms later in this work to understand the criticality of the shape of the waveform on the FLD.

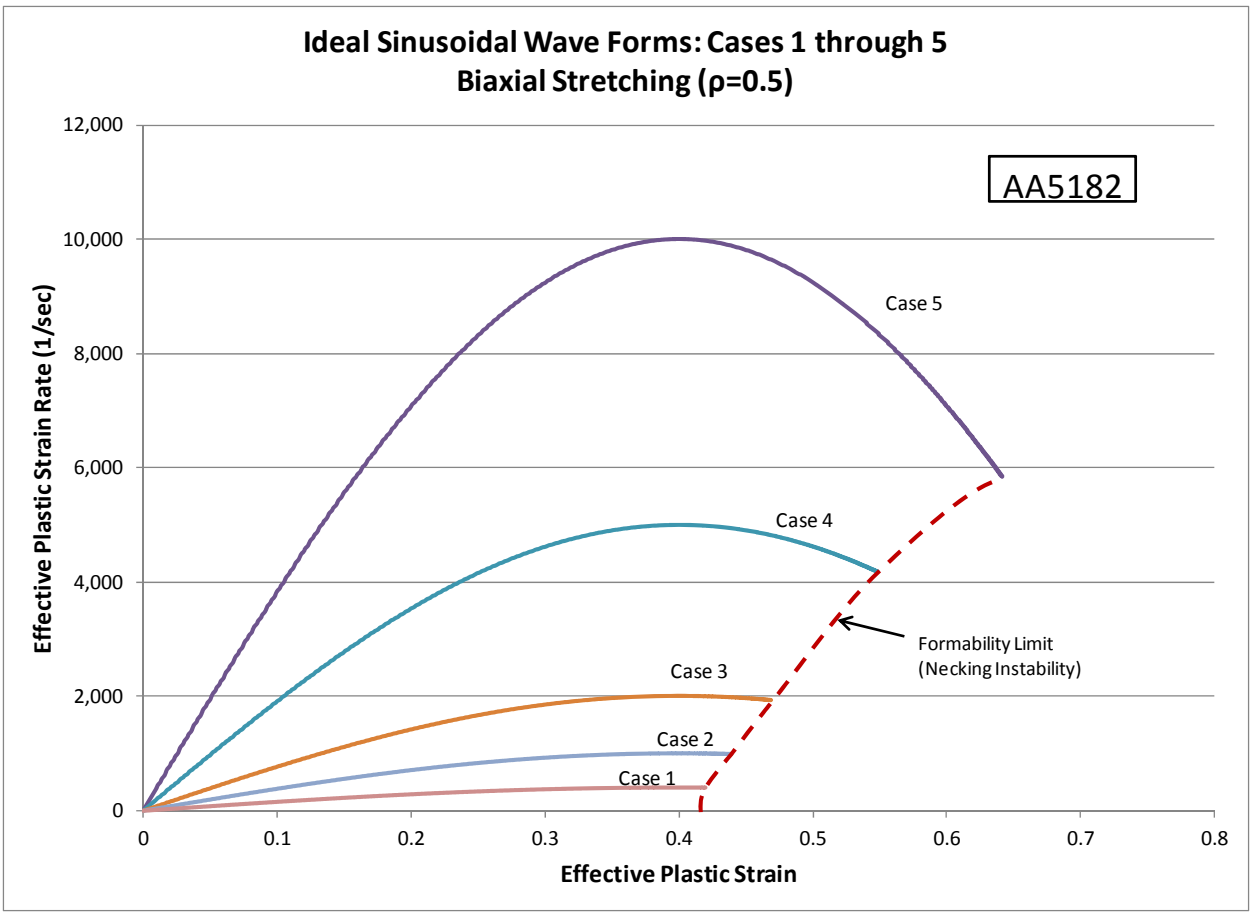

Figure 96 - Illustration of the forming limits of the material on the strain rate versus strain diagram in biaxial stretching (ρ=0.5).

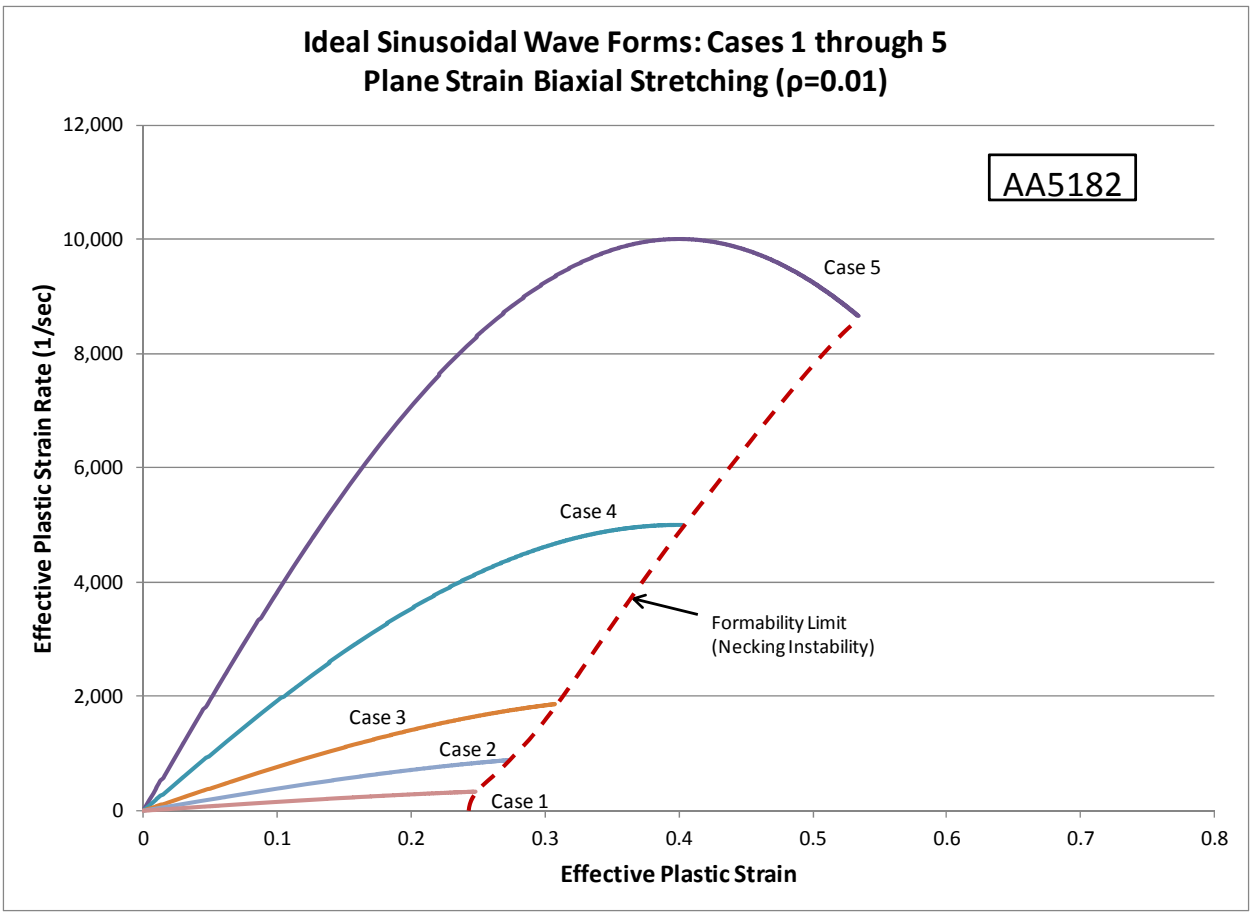

Figure 97 - Illustration of the forming limits of the material on the strain rate versus strain diagram in near plane strain (ρ=0.01).

The next parametric investigation used the identical five Cases (Cases 1-5) and the approach described above, and applied this approach to the DP600 materials. DP600 has a significantly different constitutive relation, where little change in the SRS is exhibited across the strain rate ranges relevant to PPF. Figure 98 contains the family of theoretical FLDs for all five cases, as well as the quasistatic case. The results show that DP600 is expected to have very limited enhancement in formability under PPF conditions. This theoretical result is generally supported by the experimental results of Kim et al [40], who concluded that no increase in FLD was exhibited by DP590 up to 10^2/sec. This theoretical result will require further investigation, as limited formability data exists for the DP600 material, except where die impact during forming has resulted in the formability enhancement [66].

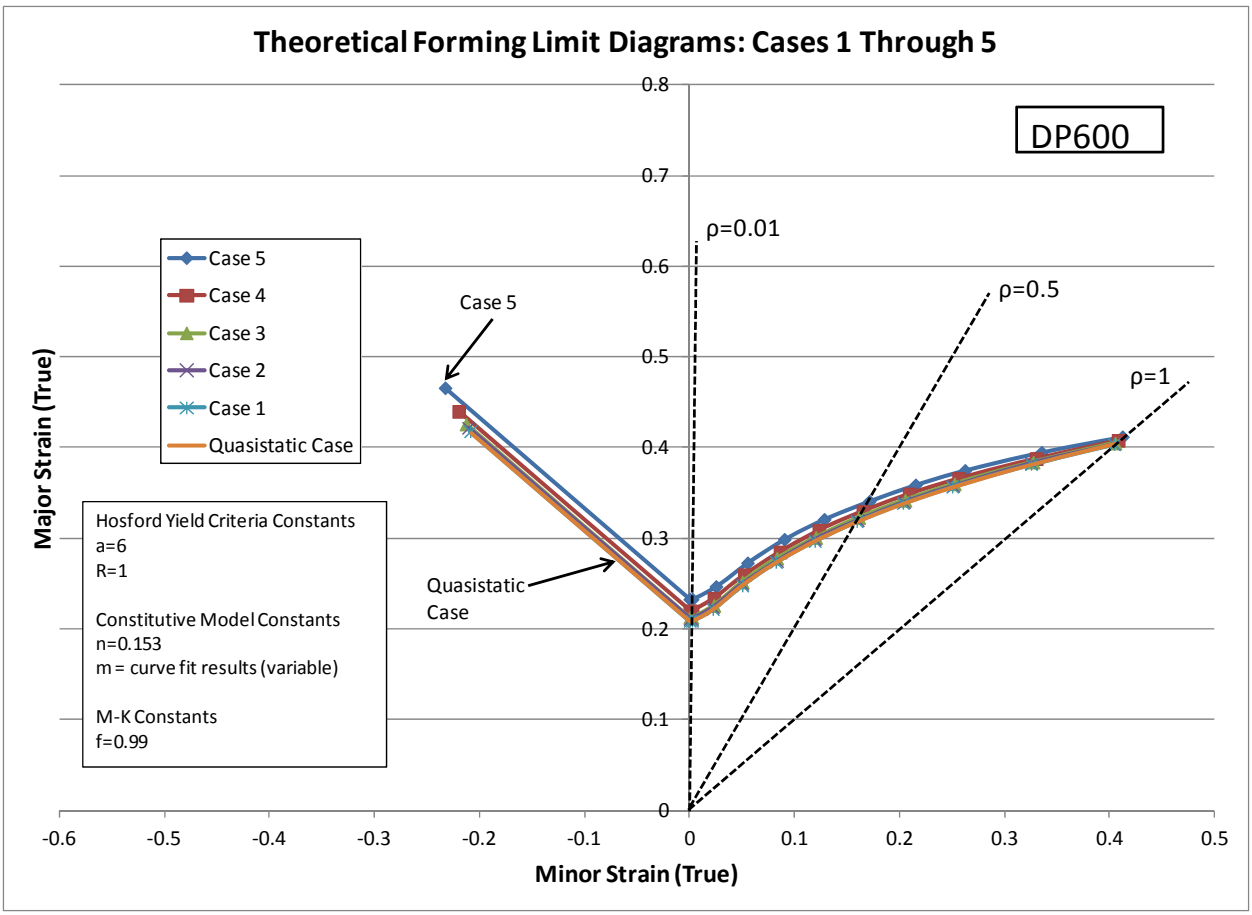

Figure 98 - Theoretical FLDs for DP600 across all five cases.

The apparent influence of the shape of the half-wave sinusoid waveform on the differences in formability across the three different loading directions (ρ=0.01, ρ=0.5, and ρ=1.0) led to parametric investigation using alternative waveforms. Two alternative waveforms were considered. First, a higher frequency sinusoid was superimposed on the original half-wave sinusoid to simulate more variation in the strain rate during forming. This alternative sinusoidal function is shown in equation 15.

$$\dot{\bar{\varepsilon}} = \dot{\bar{\varepsilon}}_{peak} \sin\left(\frac{\bar{\varepsilon}}{\bar{\varepsilon}_{peak}}\pi\right) + \frac{\dot{\bar{\varepsilon}}_{peak}}{2}\sin\left(\frac{3\bar{\varepsilon}}{\bar{\varepsilon}_{peak}}\pi\right) \qquad (15)$$

The second alternative is a square wave. This is essentially assuming that the peak strain rate is constant across the entire forming event. Figure 99 shows that two alternative waveforms with peak strain rate of $5x10^3$/sec, which are designated Case 6 and 7. Also shown on figure 99 is the original Case 4, which assumes the original half-wave sinusoid with the same peak strain rate. Figure 100 provides the results of theoretical FLD calculations showing the influence of waveform shape on the amount of plastic strain accumulated during forming for equal biaxial stretching (ρ=1.0). The figures shows that the square wave (Case 6) shows the highest overall strain accumulation prior to failure, which should be

expected since the constitutive model will have a the maximum SRS for the material under this condition. Figure 100 also shows that the superimpose sinusoid waveform (Case 7) also achieves higher plastic strain than the half-wave sinusoid (Case 4).

Figure 101 contains the theoretical FLDs for all three cases (Case 4, 6, and 7) as well as the quasistatic FLD. The data shows that the assumed waveform has a noticeable influence on the shape of the overall FLD. This is primarily due to the fact that the predicted failures occur at various strain rates depending on the direction of loading (ρ=0.01, ρ=0.5, and ρ=1.0). The overall change in the plane strain formability (FLD_0) between the half-wave sinusoid (Case 4) and the square wave (Case 6) is relatively small. However, the superimposed sinusoid (Case 7) exhibits a drop in plane strain formability relative to the other cases, even though the FLD in equal biaxial stretch is nearly identical. The drop in plane strain formability is due to the fact that failure occurs in plane strain during the low-point of strain rate on the sinusoidal waveform. Therefore the shape of the effective plastic strain rate versus effective plastic strain curve can significantly alter the general shape of the FLD for aluminum alloys.

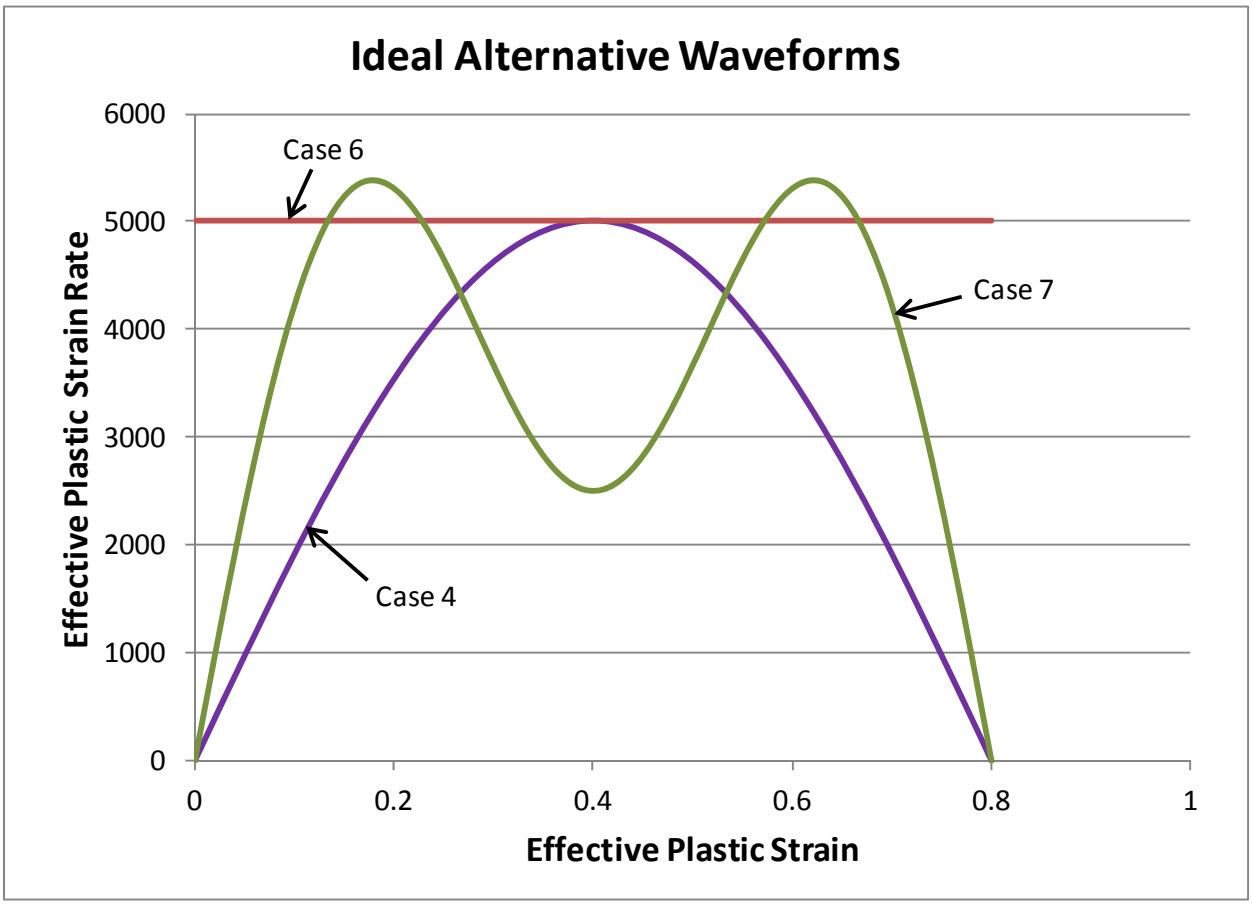

Figure 99 - Alternative ideal waveforms used to calculation theoretical FLDs.

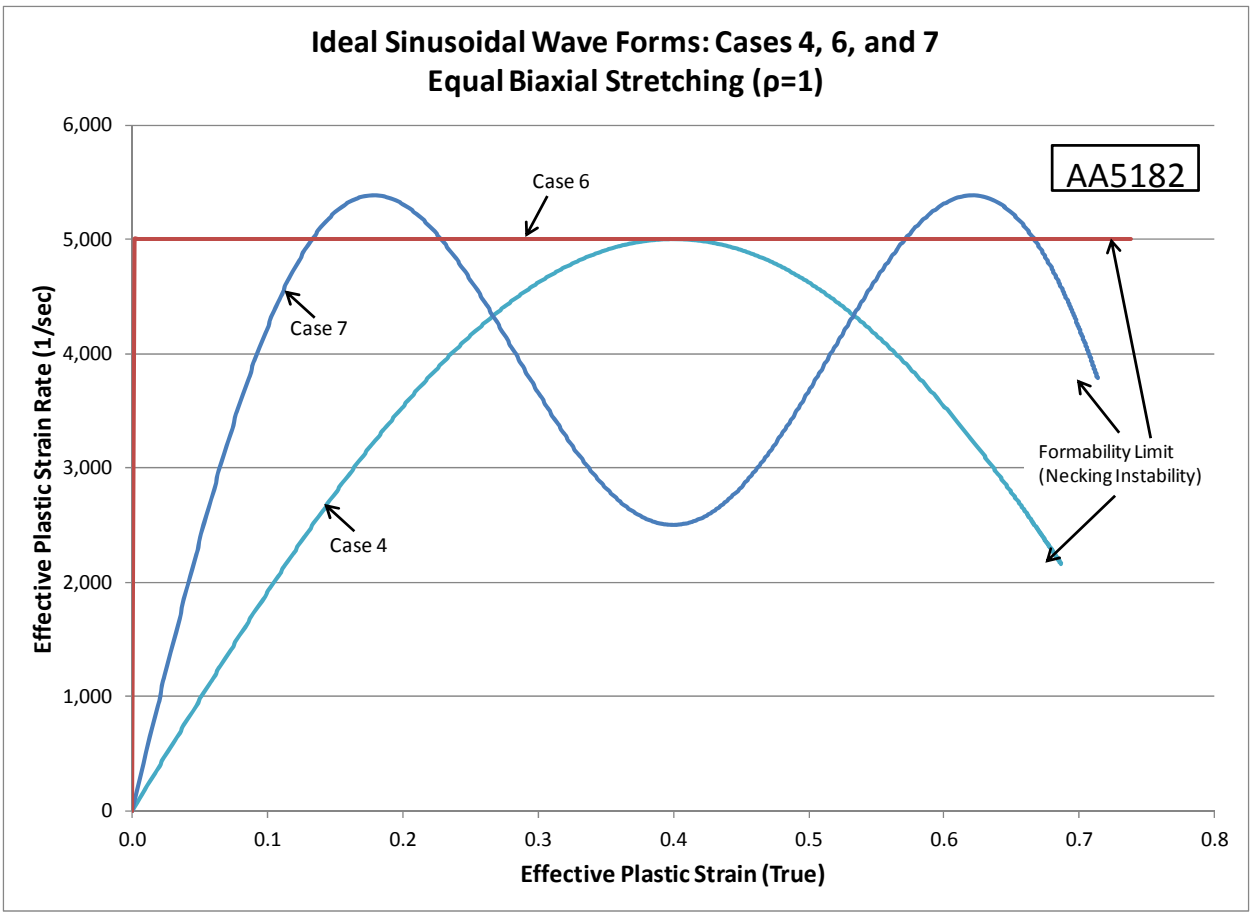

Figure 100 - Illustration of the results of theoretical FLD calculations showing the influence of waveform shape.

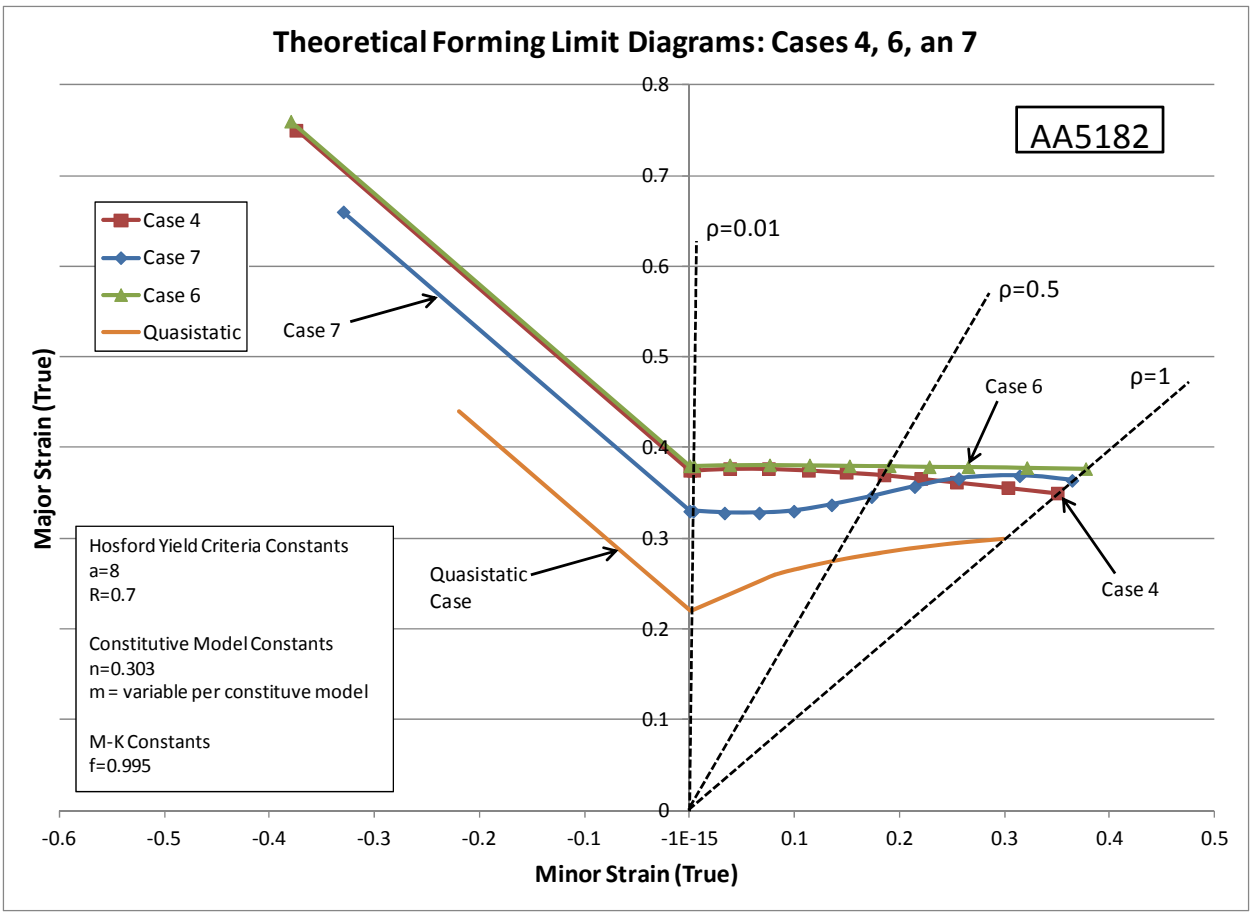

Figure 101 - Theoretical FLD results of the Case 4, 6, and 7 waveforms with peak strain rates of $5x10^3$/sec.

7 Discussion

There are several elements of this work that require additional discussion, as well as a need to perform future work to address some remaining technical issues for PPF. These issues can be divided into the topical areas of further experimental needs, further investigation into the constitutive relations of the materials, and further investigation into theoretical forming limit diagrams (FLDs).

The experimental investigation of the formability of sheet metal during PPF requires more extensive investigation into the free-forming formability. This work has developed an apparatus and employed a Digital Image Correlation (DIC) approach to experimentally investigate the materials. However, this work was limited to investigating aluminum alloy AA5182-O and advanced high strength steel DP600. The relevant automotive material set includes many more aluminum alloys (e.g. AA6011 and AA7021) and steels (e.g. HLSA350 and TRIP), as well as magnesium alloys (e.g. AZ31), which may benefit from PPF processing. Furthermore, DP600 formability should receive additional experimental investigation to more fully characterize the formability enhancement available from PPF. In addition to expanding the material set, further techniques may need developed to more thoroughly characterize the formability enhancement due to sheets impacting the die during forming. The theoretical FLDs in this work were investigated under free-forming conditions. This was perhaps the most important technical gap in understanding formability, as many previous authors have reported enhanced formability under conditions of sheets impacting dies. Alternative experiment methods (beyond DIC) may be needed to experimentally characterize formability enhancement during die impact.

The constitutive relations of the material may also require further scientific information. The constitutive relations of the material subject to PPF appear to be the dominant influence on the ability to achieve enhanced formability during PPF. However, this work does not look at the fundamental reasons why the AA5182-O alloy behaves with increasing flow stress with increasing strain rate. In general, dynamic strain aging and the nature of dislocation dynamics in the material provide only a general understanding of the behavior. Future work should include developing a better understanding of the mechanisms for increasing strain rate sensitivity at strain rates above 10^3/sec for AA5182. This might yield a more accurate non-phenomenological representation of the constitutive relations; which may need to explicitly include temperature in the constitutive relations formulation. Another element of the constitutive relations requiring further investigation is the influence of anisotropy on the formability of materials at high strain rates, and whether the mechanical properties exhibit anisotropy at high strain rates similar to the quasistatic strain rates. This work effectively assumes that the anisotropic yield locus at high strain rates behaves similar to the well-characterized behavior of the materials at quasistatic strain rates. The shape of the anisotropic yield locus is known to influence the shape the FLD, and further investigation may prove this is also true at high strain rates. A third element of the constitutive relations of the materials is the influence of adiabatic heating, which is not explicitly included in this work. The adiabatic heating has been previously shown to have little influence on the formability of materials during PPF [62], but additional work to better describe these effects may be needed.

The results of the theoretical FLD calculations can be influenced by many factors, and many of which may benefit from further investigation and refinement. A significant complicating factor to the theoretical FLD calculations is the existence of varying strain rate across the sheet metal during forming, and a different flow stress and SRS (m) across the part throughout the forming event. This condition effectively means that the theoretical FLD only applies to one single point on the specimen. For example, a forming dome will have a variable strain rate from the apex to the clamping ring for the part. Given the constitutive behavior of the material, the strain will be accumulating across the dome and formability will vary across the dome due to the varying strain rate. This effectively requires modeling a family of points (or a continuum of points) across the surface of the forming part to predict where strain localization might occur and at what strain level. In the model validation (Chapter 6.2), the theoretical FLD was calculated at the same point where failure occurred, which permitted validation. However, in a generalized formability prediction, the theoretical FLDs across the surface of the entire part will need to be tracked and analyzed. As an alternative approach, future work may need to include further investigation into the damage evolution of sheet metals during PPF by using classical void nucleation and growth models to predict material failure using internal state variables. Imbert et al [38] showed promising results of this approach, which may offer the greatest opportunity to describe automotive sheet metal forming in the complex forming environment that includes variable strain rate, complex constitutive relations, and die impact during forming.

The theoretical FLD work under this thesis also makes no attempt to treat the so-called “inertia stabilization” effect. Inertia stabilization is believed by some researchers to be a critical (or perhaps dominate) contributor to the extended ductility observed during pulse pressure forming (PPF). Balanethiram et al [31-33] argue that the constitutive relations are less important than this inertia stabilization. However, their work appears to be largely based on the supposition that the uniaxial modeling of high rate tensile tests is directly transferable to PPF formability. This may not be relevant to forming materials using a pressure pulse, since the mechanism of applied loading is completely different. The inertia stabilization is well-proven in the uniaxial case, where applied stress must be transferred from one end of a tensile specimen to the other. But, this is quite dissimilar to the loading under PPF. Moreover, most of the Balanethiram et al [31-33] arguments are based upon generalizations of the macroscopic forming observations and the microhardness of iron, copper, and aluminum alloys after being subject to Electrohydraulic forming. Given the validation of the M-K method model in this work, which does not include inertia stabilization, future work may need to be focused on validating any influence of inertia stabilization on biaxial stretching during PPF.

The Left Hand Side (LHS) of the FLD (negative minor strains) is believed to be of lesser relevance to automotive manufacturing relative to the Right Hand Side (RHS) of the FLD (positive minor strains). For this reason, the primary focus of the theoretical FLD calculations was on the RHS. However, the LHS FLD may warrant further investigation to understand the limits of the theoretical critical thickness strain used in the current work. Future work should include investigation of the influence of variable strain rate sensitivity on the shape of the FLD on the LHS (negative minor strain) region of the diagram. The influence of variable strain rate sensitivity may have influences on the shape of the LHS FLD.

There is also a need to evaluate whether the strain rate sensitivity (SRS) must be treated as a separate value inside the homogeneous and inhomogeneous regions during M-K method analysis. In the present work, the M-K method analysis assumes that the SRS in both the homogeneous and inhomogeneous regions are equal to the SRS in the homogeneous region. This is the normal convention for these calculations, and thus the reason the approach was employed. This is the more conservative case. However, using the SRS of the inhomogeneous region would predict higher formability. In this case, the SRS that is used to solve for incremental strain rate during the M-K method calculations would be much higher than the more conservative case. However, making this change may require a significant re-evaluation of the overall approach to applying the M-K method.

The final topic where technical progress must be made is in the ability to more reliably use the process of electrohydraulic forming for commercial metal forming. The experimental apparatus, and those used by most researchers, have a limited durability and are limited in size. Achieving commercial success of the implementation of the EHF (or any PPF) process may require a focused effort on the design of the manufacturing equipment capable of reliably making components with cycle times approaching 10-15 seconds.

8 Conclusions

Pulse Pressure Forming (PPF) appears to be an attractive methodology suitable to more cost-effectively manufacture automotive structures made from aluminum alloys and high strength steel (HSS). PPF technologies employ a short duration pressure-pulse to drive sheet metal into single-sided dies. The most common PPF processes being developed include Electromagnetic Forming (EMF), Electrohydraulic Forming (EHF), and Laser Shock Forming. This work has reached three primary conclusions.

The first major conclusion is that direct experimental investigation of a PPF forming event using an apparatus comprised of high speed camera arrays (up to 80,000 frames per second) and digital image correlation can locally interrogate strains and strain rates during PPF to characterize full-field biaxial strain and strain rates [7, 8]. The results of this work showed that EHF processes can develop sheet metal velocities up to 150 meters/sec, and create true effective plastic strain rates of $2x10^3$/sec. This investigation showed that achieving significant extended ductility of an AA5182 aluminum automotive sheet requires the forming event to achieve peak strain rates at or above the order of $1x10^3$/sec.

The second major conclusion is that the constitutive relations of metallic sheet metals can be characterized through uniaxial testing using conventional tensile testing systems and Split Hopkinson Pressure Bar (SHPB). Additionally, a simple modified power law constitutive relation can be employed to describe the variable strain rate sensitivity seen across the wide range of strain rates observed during PPF processes. Most metallic materials exhibit significant changes in flow stress based on strain rates and mechanical property and microstructure variation. This work determined the constitutive relations of aluminum alloy AA5182 and advances high strength steel alloy DP600 at PPF strain rates, and showed that the strain rate sensitivities of these materials can vary between m= -.022 to 0.08 for AA5182, and is relatively constant at m=0.02 for DP600. Furthermore, the relatively high strain rate sensitivities for AA5182 appear to be responsible for achieving the significant extended ductility under PPF forming events at strain rates above 10^3/sec.

The third major conclusion is that a conventional Marciniak and Kuczynski (M-K) method of formability prediction, combined with a modified power law constitutive relation that includes variable strain rate sensitivity, can successfully predict the formability of both aluminum alloy AA5182 and advanced high strength steel alloy DP600 across a wide range of strain rates and strain rate directions. The results of this work first validate the applicability and fitness of the M-K method to predict formability of sheet metals during pulse pressure forming. Furthermore, these models are used to parametrically evaluate the formability of the multiple sheet metals across a wide range of strains, strain rates, and loading paths.

The combination of these three conclusions develops a more predictive capacity to design and develop Pulse Pressure Forming manufacturing processes for a given component. The first step in developing a new application should be selecting material and characterizing and modeling it's constitutive relations from quasi-static to strain rates of 10^4/sec. The second step should be predicting the forming limits of the material across the PPF range of strains and strain rates. The third step should be designing the process to achieve the strain rates necessary for the selected to form the given component.

9 Acknowledgements

I would like to acknowledge and thank many people for their support, collaboration, and engagement while conducting this research. I would like thank my research team at PNNL, who has been working with me for many years, as the Principle Investigator, and made many outstanding technical contributions to this research and development and to the technical literature. These include Dr. Aashish Rohatgi, Elizabeth Stephens, Dr. Ayoub Soulami, Mark Smith, Dr. Danny Edwards, and Gary VanArsdale. I would also like to thank Dr. Kenneth Vecchio (University of California, San Diego, USA), who's team conducted much of the mechanical testing of the materials.

I would like to thank my advisors Dr. Said Ahzi and Dr. Mohammad Khaleel whose leadership and technical advice and interaction has proven invaluable to this research. I would also like to thank the reporters and members of the jury for their efforts, support and guidance, including Dr. Barlat, Dr. Gracio, Dr. Remond, and Dr. M'Guil.

Most of all, I would like to thank my family for the support and joy they provide me always – my wife Heather, my daughters Savanna and Erica, and my son Levi.

10 References

1. Golovashchenko, S., N. Bessonov, R. Davies; “Design and Testing of Coils for Pulsed Electromagnetic Forming”, Proceedings of the 2nd International Conference on High Speed Forming (ICHSF 2006), University of Dortmund, Germany, March 20-21, 2006.
2. Tamhane, A., M. Altynnova, and G. Daehn; “Effect of Sample Size on the Ductility in Electromagnetic Ring Expansion”; Scripta Materialia, Vol. 34, No.8, pp1345-1350, 1996.
3. Golovashchenko, S.F., Mamutov, V.S., 2005. Electrohydraulic forming of automotive panels, In: Bieler, T.R., Carsley, J.E., Fraser, H.L., Sears, J.W., Smurgeresky, J.E. (Eds.), Trends in Materials and Manufacturing Technologies for Transportation Industries and Powder Metallurgy Research and Development in the Transportation Industry. TMS, Warrendale, PA, pp. 65-70.
4. Zhou, J. Z., J.C. Yang, Y. K. Zhang, and M. Zhou; “A study of super-speed forming of metal sheet by laser shock waves”, Journal of Materials Processing Technology, Volume 129, Issue 3, 2002, Pages 241-244
5. Seth, M., V. Vohnout, and G. Daehn; “Formability of steel sheet in high velocity impact”, Journal of Materials Proc. Technology, Volume 168, Issue 3, 15 October 2005, Pages 390-400
6. Daehn, G., Y. Zhang, S. Golowin, K. Banik, A. Vivek, J.r. Johnson, G. Taber, G.K. Fenton, I. Henchi, and P. L’Eplattenier; “Coupling Experiment and Simulation in Electromagnetic Forming Using Photon Doppler Velocimetry”, Proceedings of the 3rd International Conference on High Speed Forming (ICHSF 2008), University of Dortmund, Germany, March 11-12, 2008.
7. Rohatgi, A., Stephens, E.V., Soulami, A., Davies, R.W., Smith, M.T., 2011. “*Experimental characterization of sheet metal deformation during electro-hydraulic forming”.* Journal of Materials Processing Technology, 211, pp. 1824-1833
8. Rohatgi, A., Stephens, E.V., Davies, R.W., Smith, M.T., Soulami, A., Ahzi, S., 2012. Electro-Hydraulic Forming of Sheet Metals: Free-forming vs. Conical-die Forming. Journal of Materials Processing Technology, 212, pp. 1070-1079.
9. Higashi, K., et al., “*The Microstructural Evolution During Deformation under Several Strain Rates in Commercial 5182 Aluminum Alloy”.* Journal De Physique IV, Colloque C3, October 1991. p. 347-352.
10. Davies, R.W., G.J. Grant, H.E. Oliver, M.A. Khaleel, and M.T. Smith, “Forming Limit Diagrams of Aluminum Tailor Welded Blank Weld Material,” *Metallurgical and Materials Trans A*, Vol. 32A, pp. 275-283, February, 2001.
11. Davies, R. W., Rohatgi, A., Vecchio, K.S., Ahzi, S., 2011. *Aluminum Alloy Constitutive Model across a Wide Range of Strain Rates.* Submitted to Journal of Engineering Materials Technology.
12. Correia, J.P.M., M.A. Siddiqui, b, S. Ahzia, S. Belouettar and R. Davies; “A simple model to simulate electromagnetic sheet free bulging process”, International Journal of Mechanical Sciences, Volume 50, Issues 10-11, October-November 2008, Pages 1466-1475S.
13. Golovashchenko, S., N. Bessonov, R. Davies; “Modeling of Pulsed Electromagnetic Forming”, Numisheet 2008, Interlaken, Switzerland, September 1-5, 2008.
14. Golovashchenko, S., N. Bessonov, and R. Davies; “Analysis of Blank-Die Contact Interaction in Pulsed Forming Processes”, Proceedings of the 3rd International Conference on High Speed Forming (ICHSF 2008), University of Dortmund, Germany, March 11-12, 2008.

15. Davies, R.W., A. Rohatgi, E.V. Stephens, A. Soulami, and S. Ahzi; “Sheet Metal Forming and Failure during Biaxial Stretching at High Strain Rates”, Manuscript in preparation for the International Journal of Plasticity.
16. Daehn, G.S., 2006. High-Velocity Metal Forming, In: Semiatin, S.L. (Ed.), ASM Handbook, Metalworking: Sheet Forming. ASM International, Materials Park, Ohio, pp. 405-418.
17. Psyka, V., D. Risch, B.L. Kinsey, A.E. Tekkaya, and M. Kleiner; “Electromagnetic forming—A review”, Journal of Materials Processing Technology, 211, 787–829.
18. Harvey, G.W., Brower, D.F., 1958. Metal Forming Device and Method. US-Patent No. 2976907.
19. Oliveira, D.A., M.J. Worswick, M.J., M. Finn, and D. Newman; 2005. “Electromagnetic forming aluminum alloy sheet: free-form and cavity fill experiments and model”, Journal of Materials Processing Technology, 170, 350–362.
20. Beerwald, C., Brosius, A., Kleiner, M., Psyk, V., 2003. Einfluss des magnetischen Druckes bei der elektromagnetischen Blechumformung. In: 2. Kolloquium Elektromagnetische Umformung, Dortmund, pp. 77–85.
21. Golovashchenko, S.F., Bessonov, N.M., Ilinich, A.M., 2011. Two-step method of forming complex shapes from sheet metal. J. Mater. Process. Technol. 211, 875-885.
22. Shang, J., and Daehn, G., 2011. Electromagnetically Assisted Sheet Metal Stamping. Journal of Materials Processing Technology, 211, 868-874.
23. Yutkin, L.A., 1955. Electrohydraulic Effect. Mashgiz, Moscow, Russia, pp. 5–22.
24. Parr, J.F., 1960. Tooling Engineering, Vol. 44, p.81
25. Cadwell, G.C., 1962. Metalworking, Vol. 106, p.49
26. Wagner, H.J., 1960. Tooling Engineering, Vol. 44, p.83
27. Bruno, E.J., 1968. High-velocity Forming of Metals, revised edition. ASTM, Dearborn, pp. 73–108.
28. Oyane, M., and Masaki, S., 1964. Fundamental Study on Electrohydraulic Forming, Bulletin of the Japan Society of Engineers, Vol. 7, No. 26, pp. 474-480
29. Oyane, M., and Masaki, S., 1965. Fundamental Study on Electrohydraulic Forming (II), Bulletin of the Japan Society of Engineers, Vol. 8, No. 30, pp. 251-258
30. Oyane, M., and Masaki, S., 1965. Fundamental Study on Electrohydraulic Forming (III), Bulletin of the Japan Society of Engineers, Vol. 8, No. 30, pp. 259-263
31. Balanethiram, V.S., Daehn, G.S., 1992. Enhanced formability of interstitial free iron at high-strain rates. Scr. Metall. Materialia 27, 1783-1788.
32. Balanethiram, V.S., Daehn, G.S., 1994. Hyperplasticity - Increased forming limits at high workpiece velocity. Scr. Metall. Materialia 30, 515-520.
33. Balanethiram, V.S., Hu, X.Y., Altynova, M., Daehn, G.S., 1994. Hyperplasticity - Enhanced formability at high-rates. J. Mater. Process. Technol. 45, 595-600.
34. Golovashchenko, S. F., Mamutov, V., Dmitriev, V. V., and Sherman, A. M., 2003, “Formability Of Sheet Metal With Pulsed Electromagnetic And Electrohydraulic Technologies,” S. K. Das, ed., Aluminum 2003, TMS, Warrendale, PA, pp. 99-110.
35. Tobe, T., Kato, M., Obara, H., 1979. Metal Forming by Underwater Wire Explosion 1. An Analysis of Plastic-Deformation of Circular Membranes Under Impulsive Loading. Bulletin of the JSME-Japan Society of Mechanical Engineers 22, 271-278.

36. Tobe, T., Kato, M., Obara, H., 1984. Metal-forming by underwater wire explosions 2. Experiments on bulging of circular aluminum sheets by copper wire explosions. Bulletin of the JSME-Japan Society of Mechanical Engineers 27, 130-135.
37. Imbert, J., Worswick, M., Winkler, S., Golovashchenko, S., Dmitriev, V., 2005. Analysis of the increased formability of aluminum alloy sheet formed using electromagnetic forming, SAE World Congress, Paper 2005-01-0082. SAE International, Detroit, Michigan, USA.
38. Imbert, J.M., Winkler, S.L., Worswick, M.J., Oliveira, D.A., Golovashchenko, S., 2005. The effect of tool-sheet interaction on damage evolution in electromagnetic forming of aluminum alloy sheet. J. Eng. Mater. Technol.-Trans. ASME 127, 145-153.
39. Oliveira, D.A., Worswick, M., 2003. Electromagnetic forming of aluminium alloy sheet. J. Phys. IV 110, 293-298.
40. Kim, S.B., H. Huh, H.H. Bok, and M.B. Moon, 2011. Forming limit diagram of auto-body steel sheets for high-speed sheet metal forming, Journal of Materials Processing Technology, Vol. 211, 851–862.
41. Taylor, B., 1988. Formability testing of sheet metals, Metals Handbook- Forming and Forging, 9 ed. ASM International, Metals Park, Ohio, pp. 877-879.
42. Golovashchenko, S.F., 2007. Material formability and coil design in electromagnetic forming. J. Mater. Eng. Perform. 16, 314-320.
43. Johnson, J.R., Taber, G., Vivek, A., Zhang, Y., Golowin, S., Banik, K., Fenton, G.K., Daehn, G.S., 2009. Coupling Experiment and Simulation in Electromagnetic Forming Using Photon Doppler Velocimetry. Steel Res. Int. 80, 359-365.
44. Mercier, S., Granier, N., Molinari, A., Llorca, F., Buy, F., 2010. Multiple necking during the dynamic expansion of hemispherical metallic shells, from experiments to modelling. Journal of the Mechanics and Physics of Solids 58, 955-982.
45. Wielage, H., Vollertsen, F., 2011. Classification of laser shock forming within the field of high speed forming processes. J. Mater. Process. Technol. 211, 953-957.
46. Badelt, M., Beerwald, C., Brosius, A., Kleiner, M., 2003. Process Analysis of Electromagnetic Sheet Metal Forming by Online-Measurement and Finite Element Simulation, ESAFORM 2003 - 6th International Conference on Material Forming, Salerno, Italy, pp. 123-126.
47. Higashi, K., T. Mukai, K. Kaizu, S. Tsuchida, S. Tanimura, Journal de Physique IV, Colloque C3, suppl. au Journal de Physique III, Vol. 1, October 1991, C3-347 - C3-352.
48. Dieter, G.E., Mechanical Metallurgy, third ed., McGraw-Hill, Boston, 1986.
49. Higashi, K., T. Mukai, K. Kaizu, S. Tsuchida, S. Tanimura, Journal de Physique IV, Colloque C3, suppl. au Journal de Physique III, Vol. 1, October 1991, C3-341 - C3-346.
50. Lin, M., B. Pang and W. Zhang, 2009. Dynamic tensile behavior of Al-6Mg alloy with three treatment states. DYMAT 2009 - 9th International Conference on the Mechanical and Physical Behaviour of Materials under Dynamic Loading, Vol. 2, 1125 – 1131
51. Mukai, T., M. Kawazoe, and K. Higashi, 1998. Strain-rate dependence of mechanical properties in AA5056 Al–Mg alloy processed by equal-channel-angular-extrusion, Materials Science and Engineering A, Vol. 247, 270–274

52. Smerd, R., S. Winkler, C. Salisbury, M. Worswick, D. Lloyd, and M. Finn, High strain rate tensile testing of automotive aluminum alloy sheet. International Journal of Impact Engineering, 2005. 32: p. 541 - 560.
53. Huh, H., S. Kima, J. Songa, and J Limb, 2008. Dynamic tensile characteristics of TRIP-type and DP-type steel sheets for an auto-body. International Journal of Mechanical Sciences, Vol. 50, p. 918 - 931.
54. Yu, H., Y. Guo, and X. Lai, 2009. Rate-dependent behavior and constitutive model of DP600 steel at strain rate from 10^-4 to 10^3/sec. Materials and Design, Vol. 30, 2501–2505.
55. Marciniak, Z. and K. Kuczynski, 1967. International Journal of Mechanical Sciences, Vol. 9, 609.
56. Jie, M., C.H. Cheng, L.C. Chan, and C.L. Chow, 2009. Forming limit diagrams of strain-rate-dependent sheet metals, International JournalofMechanicalSciences, Vol. 51, 269–275
57. Khan, A.S., and Baig, M. 2011. Anisotropic response, constitutive modeling and the effects of strain rate and temperature on the formability of an aluminum alloys, International Journal of Plasticity, 27, 522–538.
58. Kim, K.J., Kim, D., Choi, S.H., Chung, K., Shin, K.S., Barlat, F., K.H.Oh, and J.R.Youn, 2003. Formability of AA5182/polypropylene/AA5182 sandwich sheets, Journal of Materials Processing Technology, Vol. 139, p 1–7.
59. Khan, A.S., Liang, R., 1999. Behavior of three BCC metal over a wide range of strain rates and temperatures. International Journal of Plasticity 15, 1089–1109.
60. Khan, A.S., Liang, R., 2000. Behavior of three BCC metals during non-proportional multi-axial loadings. International Journal of Plasticity 16, 1443–1458.
61. Barlat, F., Maeda, Y., Chung, K., Yanagawa, M., Brem, J.C., Hayashida, Y., Lege, D.J., Matsui, K., Murtha, S.J., Hattori, S., Becker, R.C., Makosey, S., 1997. Yield function development for aluminum alloy sheets. Journal of the Mechanics and Physics of Solids 45 (11/12), 1727–1763.
62. Thomas, J.D., N. Triantafyllidis, 2007. Theory of necking localization in unconstrained electromagnetic expansion of thin sheets, International Journal of Solids and Structures, Vol. 44, 6744–6767
63. Hu, X., and G.S. Daehn, 1996. Effect of Velocity on Flow Localization in Tension. Acta Metallurgica, Vol. 44, No. 3, 1021-1033
64. Rohatgi, A., Soulami, A., Stephens, E.V., Davies, R.W., Smith, M.T. Enhanced formability in 5182-O Al at room temperature using electro-hydraulic forming. Manuscript in preparation for Journal of Materials Processing Technology.
65. Rohatgi, A., Stephens, E.V., Soulami, A., Davies, R.W., Smith, M.T., 2010. High-strain-rate forming of aluminum and steel sheets for automotive applications, In: Kolleck, R. (Ed.), International Deep Drawing Group (IDDRG), Graz, Austria, pp. 441-450.
66. Rohatgi, A., Stephens, E.V., Edwards, D.J., Smith, M.T., Davies, R.W., 2012. Electro-hydraulic forming of advanced high-strength steels: Deformation and microstructural characterization. In press, Proceedings of the 2012 ASME Manufaturing Science and Engineering Conference (MSEC2012), Paper MSEC2012-7322, June 4-8, 2012, Notre Dame, Indiana, USA.
67. Liang, R., A.S. Khan, Int. J. of Plasticity 15 (1999) 963-980.
68. Johnson, G.R., W.H. Cook, 7th Int. Symp. on Ballistics (1983) 541-547.
69. Hollomon, J.H., Trans. Metall. Soc. AIME 162 (1945) 268-290.

70. Hu, J., Z. Marciniak, J.Duncan, Mechanics of Sheet Metal Forming, second ed., Butterworth-Hienemann, Woburn, MA, 2002.
71. Dieter, G.E., Mechanical Metallurgy, third ed., McGraw-Hill, Boston, 1986.
72. Wagenhofer, M., M. Erickson-Natishan, R.W. Armstrong, F.J. Zerilli, Scr. Mater. 41 (1999) 1177-1184.
73. Mukhopadhyay, J., Parameters Affecting Strain Rate Sensitivity in Al-Mg Alloys, in: Z. Jin, A Beaudoin, T.A. Bieler and B Radhakrishnan (Eds.), Hot Deformation of Aluminum Alloys III, TMS, 2003, pp.391-398.
74. Barlat, F., M.Z. Glazov, J.C. Brem, D.J. Lege, Int. J. of Plasticity 18 (2002) 919-939.
75. Lian, J. and B. Baudelet: *Mater. Sci. Eng.*, **86**, 1987, pp. 137-144
76. Chan, K.S., D.A. Koss, and A.K. Ghosh: *Metallurgical Transactions A*, 15A, February 1984, pp. 323-329.
77. Hill, R.: *J. Mech. Phys. Solids*, 1, 1952, pp. 1
78. Graf, A., and W. F. Hosford: Metall. Trans. A, 21A, 1990, pp.87
79. Hosford, W.F., and R. M. Caddell, Metal Forming – Mechanics and Metallurgy, 2nd ed., Prentice Hall (1993)
80. Graf, A., and W. F. Hosford: Forming Limit Diagrams: Concepts, Methods, and Applications, TMS, 1989, pp.153
81. Xu, S., K.J. Weinmann, and A. Chandra: *Journal of Engineering Materials,* **120**, 1998.